Decay of plasmonic excitations in one dimensional assemblies of metallic nanoparticules

Adam Brandstetter-Kunc

UNIVERSITÉ DE STRASBOURG

ÉCOLE DOCTORALE PHYSIQUE ET CHIMIE PHYSIQUE

[182]

THÈSE

présentée par :

Adam BRANDSTETTER-KUNC

soutenue le : 15 **Décembre 2016**

pour obtenir le grade de : **Docteur de l'université de Strasbourg**

Discipline/ Spécialité : Physique de la matière condensée

Decay of plasmonic excitations in one dimensional assemblies of metallic nanoparticles

THÈSE dirigée par :

M. JALABERT Rodolfo	Professeur, Université de Strasbourg

RAPPORTEURS :

M. ADAM Pierre-Michel	Professeur, Université de Technologie de Troyes
M. INGOLD Gert-Ludwig	Professeur, Universität Augsburg

AUTRES MEMBRES DU JURY :

Mme. HALTE Valérie	Maître de conférences, IPCMS
M. MANFREDI Giovanni	Directeur de recherche, IPCMS
M. MOLINA Rafael	Chargé de recherche, Consejo Superior de Investigaciones Científicas
M. WEICK Guillaume	Maître de conférences, Université de Strasbourg
M. WEINMANN Dietmar	Directeur de recherche, IPCMS

Contents

Résumé

Les propriétées optiques très spécifiques des petits objets métalliques sont à l'origine des avancées spectaculaires réalisées dans le domaine de la nanophotonique [1–4]. Ce sont les oscillations collectives des électrons de conduction qui permettent de telles propriétés optiques. Ces excitations, où les charges électriques oscillent, soit à la surface du métal soit directement à l'interieur des nanostructures, sont appellées *résonances plasmons de surface* [3]. Dans le premier cas [5], les plasmons se propagent le long de l'interface entre le métal et le diélectrique avec une impulsion non-nulle. Cette thèse se concentre sur le second cas, celui de nanoparticules où les plasmons sont confinés, ce qui à pour effet de localiser les oscillations des charges électriques à l'interface avec le milieu diélectrique environnant. Ce type de plasmons est appelé *plasmon de surface localisé* (LSP) et nous utiliserons la terminologie de plasmons de surface lorsque aucune confusion avec les plasmons propageants n'est possible.

Tandis que les recherches scientifiques sur les LSPs (ou plasmons) s'étendent sur plus d'un siècle [12], leurs utilisations remontent à des temps encore plus anciens [13]. Allant du cas de la nanoparticule unique [1, 12, 14–35] à celui où un réseau régulier de nanoparticule à été réalisé [36–67] offrant ainsi un environnement de recherche riche et permettant des avancées scientifiques diverses dans la compréhension des intéractions entre la lumière et la matière à l'échelle du nanomètre. Grâce aux avancées dans le domaine de la miniaturisation [63], les scientifiques sont à présent capables de concevoir des réseaux de nanoparticules où les espaces entre les particules ainsi que les propriétés des matériaux sont très bien contrôlées. De tels progrès nous permettent de développer et tester les concepts théoriques présentés dans cette thèse aidant ainsi dans la conception de nouveaux matériaux possédant de nouvelles propriétées optiques.

L'étude des excitations collectives dans des dimères constitués de nanoparticules [71] date de plus de 74 ans après l'article fondateur de Mie [12] sur la particule unique. Dans de telles structures dimérisées, les intéractions entre les plasmons de chacune des deux nanoparticules provoque l'apparition de modes collectifs symétriques et anti-symétriques. Les modes symetriques sont fortement couplés à la lumière et sont donc généralement appellés *brillants* dans la littérature scientifique. À

l'inverse, les modes anti-symétriques ne se couplent que faiblement à la lumière sont donc appellés modes *sombres*.

La description théorique de ces modes plasmoniques collectifs à été réalisée à travers différentes méthodes [71–78]. Une de ces méthodes est de partir de la théorie de Mie en utilisant ensuite les équations de Maxwell [71, 72] afin d'obtenir l'énergie de ces modes. Cependant, l'absence de symétries sphériques dans le cas du dimère ne permet pas de réaliser les calculs de façon exacte et nécessite certaines approximations ou des calculs numériques pour être achevés. L'avantage de cette approche est qu'elle inclut directement les résonances plasmoniques multipôlaires. Une méthode simplifiée proposée par Nordlander *et al.* [73] à été utilisée afin d'obtenir une hybridisation plasmonique. Dans leur travail, les auteurs ont montré que les modes collectifs d'une nanoparticule peuvent être décrits comme une superposition d'états *liés* et *anti-liés* constitués de plasmons individuels qui possèdent respectivement une énergie faible et élevée. En utilisant leur model, ils ont pu obtenir les niveaux énergétiques de ces modes plasmoniques couplés ainsi que leur dépendance avec la distance entre les nanoparticules.

Du côté expérimental, l'avancée des techniques de miniaturisation ont permis de réaliser des dimères constitués de nanoparticules de taille ainsi que de séparation très petites, qui ont alors pu être étudiés [79–86].

Ces structures dimérisées en plus de leurs propriétées intrinsèques intéressantes constitues un excellent point de départ pour l'étude de structures plus complexes telle que des chaines de nanoparticules.

La proposition d'utiliser une chaîne linéaire de nanoparticules métalliques sphériques pour propager de manière guidée la lumière sur des distance sub-longueur d'onde [37] a été accompagnée par des calculs d'électromagnétisme classique basés sur la théorie généralisée de Mie [36]. En résolvant les équations de Maxwell pour une chaîne linéaire de nanoparticules d'argent de 25 nm de rayon (la lumière excitant la chaîne n'illumine que la première nanoparticule de la chaîne), les auteurs de la Ref. [37] ont essayé d'optimiser l'écart de distance entre les nanoparticules pour obtenir une longueur maximale de propagation. Une longueur de propagation significative n'a été trouvée que pour une excitation longitudinale (champ électrique parallèle à l'axe de la chaîne). La longueur de propagation maximale (900nm) a été obtenue pour une distance centre-à-centre de 75nm. De telles chaînes, ainsi que des structures contenant des jonctions ou des coins ont été étudiées par Brongersma *et al.* [40] à partir d'un modèle se basant sur des dipôles ponctuels électriques couplés. À partir de la forme analytique des relations de dispersion des modes longitudinaux et transverses, ils ont pu montrer que ces modes ne sont que faiblement affectés par un couplage pris au delà des plus proches voisins.

En supposant un rayonnement électromagnétique d'une nanoparticule non-couplée, les auteurs de la Ref. [40] ont trouvé des pertes radia-

tives négligeables basées sur l'estimation de la radiation d'un unique électron oscillant. Avec ces hypothèses, des atténuations comparables pour les modes transverses et longitudinaux ainsi que des distances de propagations similaires à celles obtenues dans la Ref. [37] furent obtenues. Les résultats de la Ref. [40] ont ensuite été testés en utilisant des calculs de difference finie dabs la domain temporel (FDTD) pour une chaîne constituée de nanoparticule d'argent [44], confirmant ainsi la relation de dispersion obtenue en utilisant le modèle des dipôles couplés de la Ref. [40]. De plus, la possibilité de propager une excitation pulsée a été confirmée par les auteurs de la Ref. [44], tandis qu'une atténuation (de 3dB/140nm pour les modes longitudinaux et 3dB/43nm pour les transversaux) plus élevée que celle prédie dans la Ref. [40] pour une chaîne de nanoparticules d'argent a été observée.

Des études théoriques plus approfondies ont consideré l'influence des effets du retard de l'intéraction dipôle-dipôle sur les propriétées plasmoniques d'une chaîne. Il a été montré [46, 47] qu'il existe un comportement non-monotone pour la relation de dispersion des modes transverses dû à ces effets de retard, alors que les modes longitudinaux ne sont pas affectés. Dans la Ref. [46] il a été avancé que la concordance de phase entre la dispersion plasmonique et les photons de même fréquence était responsable de cette non-monotonie. De plus, il a été montré que les effets des intéractions sur les pertes radiatives donnent un amortissement radiatif dépendant du mode plasmonique [46, 47].

Il a été montré que la décroissance de la propagation plasmonique dans une chaîne électriquement forcée était de nature non-exponentielle, à la fois pour les modes transverses et longitudinaux [46], avec les modes transverses subsistant sur des distances plus importantes que les modes longitudinaux. D'autres travaux utilisant une approche similaire ont cette fois étudié des chaînes ordonnées et désordonnées de nanoparticules métalliques [53]. Tandis que des comportement similaires à ceux obtenus à la Ref. [46] pour les relations de dispersion et l'amortissement radiatif ont été observés, il a été introduit une distinction entre deux type de plasmons : les plasmons ordinaires, des modes sub-radiatifs qui sont loalisés en présence de désordre et ceux dits extraordinaires, des modes qui radient quelque soit le désordre présent.

Plus récemment, les propriétées quantiques des chaînes de nanoparticules métalliques ont également suscité de l'attention du fait que de telles chaînes pourraient servir d'outils de communication quantiques [57] et pourraient présenter des états intriqués stockés dans les plasmons collectifs [61].

La première observation expérimentale du champ proche associé aux plasmons collectifs dans une chaîne ordonnée de nanoparticules à été réalisée par Krenn *et al.* [38] en utilisant un microscope à balayage (PSTM). Les images PSTM obtenues pour une chaîne de 10000 nanoparticule d'or (Au) de taille $100\times100\times40\text{nm}^3$ et séparées par une

distance de 100nm sont cohérente avec la résolution numérique des équations de Maxwell. En utilisant une technique de spectroscopie en champ lointain plutôt qu'en champ proche, Maier *et al.* [42] ont mesuré les fréquences à longueur d'onde infinies des modes transverses et longitudinaux pour une chaîne constituée de 80 nanoparticules sphériques d'or d'un diamètre de 50nm et séparées de 75nm. Ces résultats expérimentaux ont été confrontés aux prédictions de la Ref. [40] et ont permis l'accès aux vitesses de groupe des plasmons.

D'autres études expérimentales [43] utilisant un microscope à balayage optique en champ proche (NSOM), ainsi que des colorants fluorescents, ont étudié le transport d'énergie le long d'une chaîne de nanoparticules d'argent de taille $90\times30\times30\text{nm}^3$ séparées par une distance de 50nm, et ont obtenu une atténuation de l'excitation plasmonique de 6dB sur 195nm. De plus, les avancées récentes des techniques expérimentales ont permis d'imager spatialement le champs électrique associé aux plasmons le long de la chaîne utilisant un microscope optique en champ proche [60]. La spectroscopie par perte d'energie des électrons (EELS) a également éététilisée pour exciter et détecter des modes sub-radiants dans des chaînes de nanoparticules [62].

Nous proposons dans cette thèse une approche générale basée sur le concept de système quantique ouvert pour étudier les plasmons en intéraction dans des assemblées unidimensionnelles de nanoparticules métalliques. Ce modèle nous donnera les outils pour comprendre comment la séparation entre les particules influence la relation de dispersion ainsi que les méchanismes d'amortissements du système. Il nous permettera également d'étudier la propagation des excitations à travers des chaînes de nanoparticules.

Le chapitre 2 est consacré au cadre théorique de l'approche du système quantique ouvert dans l'approximation du jellium appliqué pour une nanoparticule métallique isolée. Partant du hamiltonien microscopique dans la jauge de Coulomb, nous séparons les coordonnées en cordonnées du centre de masse (plasmons) et coordonnées relatives (électrons), qui donne alors lieu à la forme générale du hamiltonien du système

$$H = H_{\text{pl}} + H_{\text{eh}} + H_{\text{pl-eh}} + H_{\text{ph}} + H_{\text{pl-ph}}, \tag{1}$$

qui est utilisé aux chapitres 3 et 4 (avec l'ajout d'une force externe dans le chapitre 4). Dans l'Eq. (1), H_{pl} décrit les plasmons et leurs intéractions mutuelles, H_{eh} et H_{ph} représentents respectivement les bains de paires électrons-trous et de photons. $H_{\text{pl-eh}}$ et $H_{\text{pl-ph}}$ sont respectivement les interactions entre le système plasmonique et les bains de paires électrons-trous et de photons. Le hamiltonien (1) est caractéristique d'un système quantique ouvert, où le petit système quantique (plasmon) est couplé à l'environnement (électronique et photonique) extérieur. L'utilisation de l'approximation de champ moyen pour le bain électronique permet d'obtenir des résultats analytiques

concerant le temps de vie des plasmons.

Le couplage entre les plasmons et les électrons est dû à la brisure du théorème de Kohn [89], à cause du caractère non-harmonique du potentiel de confinement de l'électron. Ce couplage permet alors l'existence d'un processus où le plasmon se désintègre en produisant une paire électron-trou (i.e. l'amortissement Landau). À la section 2.3 nous présentons la méthode pour évaluer cet amortissement Landau utilisant une règle d'or de Fermi qui donne alors

$$\gamma_0^{\mathrm{L}} = \frac{3v_{\mathrm{F}}}{4a} g\left(\frac{\hbar\omega_0}{E_{\mathrm{F}}}\right), \tag{2}$$

où v_{F} et E_{F} sont respectivement la vitesse et l'énergie de Fermi. Dans l'expression ci-dessus, ω_0 est la fréquence de Mie d'un plasmon dans une nanoparticule et a est le rayon de la nanoparticule. La fonction $g(\nu)$ est définie par

$$g(\nu) = \frac{2}{\nu} \int_{\max\{1,\nu\}}^{1+\nu} \mathrm{d}x \int_{0}^{x-\nu} \mathrm{d}y \sqrt{(x-y)(x-y-\nu)}. \tag{3}$$

La forme de l'amortissement Landau (2) est en accord avec celle proposée par Kawabata et Kubo [14] montrant une relation inversement proportionnelle à la taille de la nanoparticule a.

À la section 2.4 nous évaluons l'effet du couplage entre les plasmons et les photons. Ce couplage donne lieu à des pertes radiatives qui sont une conséquence directe de la radiation provenant de charges accélérées. Utilisant également une règle d'or de Fermi, il est possible d'obtenir l'expression bien connue de l'amortissement radiatif,

$$\gamma_0^{\mathrm{r}} = \frac{2\omega_0^4}{3c^3} a^3, \tag{4}$$

qui ne dépend pas de la polarisation à cause de la symétrie sphérique du système. On peut noter que l'amortissement radiatif (4) dépend du volume de la particule qui est relié au nombre d'électrons constituant le plasmon. Ce résultat (4) peut également être retrouvé en utilisant l'électrodynamique classique [70], que nous présentons à l'annexe A. Cependant, utilser la théorie quantique rend cette présentation plus uniforme et cohérente.

Nous utilisons au chapitre 3 le cadre théorique du chapitre 2 pour étudier comment les amortissement Landau et radiatif changent dans le cas de dimères, qui constituent la brique élementaire de structures plus complexes telle que la chaîne de nanoparticules présentée au chapitre 4.

Nous commençons notre étude en calculant les modes propres des plasmons collectifs d'un dimère hétérogène représentéà la Figure 1.

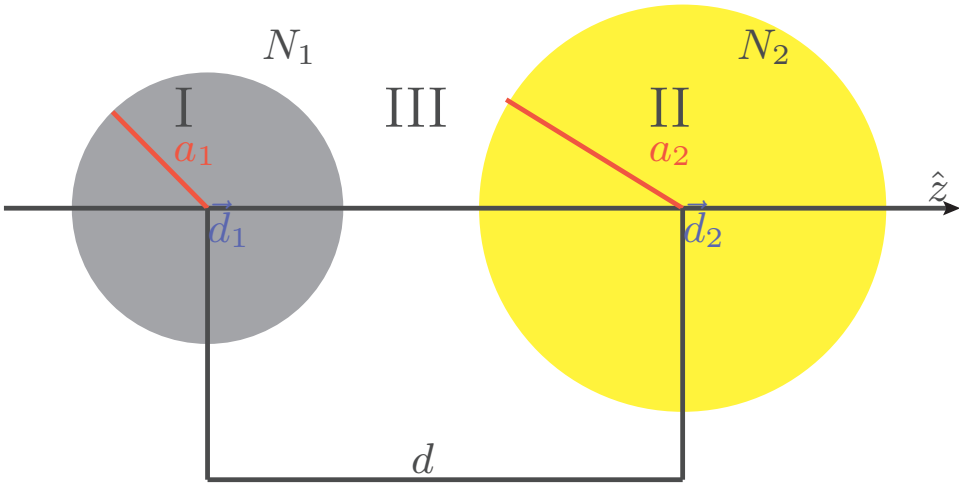

Figure 1: Schéma d'un dimère hétérogène constitué de deux nanoparticules de rayons a_1 et a_2 contenant, respectivement, N_1 et N_2 électrons, séparées d'une distance d l'une de l'autre. $\vec{d}_1$ et $\vec{d}_2$ représentent respectivement le centre de la nanoparticule 1 et 2.

Partant du hamiltonien microscopique du système sous l'hypothèse que la distance entre les particules d est bien plus grand que le rayons des nanoparticules a_n, nous exprimons le hamiltonien sous la forme suivante:

$$H_{\rm pl} = \sum_{n=1}^{2}\left(\frac{\mathbf{P}_n^2}{2M_n} + \frac{M_n}{2}\tilde{\omega}_n^2\mathbf{R}_n^2\right) + \frac{Q_1Q_2}{d^3}[\mathbf{R}_1\cdot\mathbf{R}_2 - 3(\mathbf{R}_1\cdot\hat{\mathbf{d}})(\mathbf{R}_2\cdot\hat{\mathbf{d}})], \quad (5)$$

où $M_n = N_n m_{\rm e}$ et $Q_n = N_n e$ sont respectivement la masse et la charge électronique totale de la n-ième nanoparticule, et $\tilde{\omega}_n$ est la fréquence de Mie du plasmon de la n-ième nanoparticule décallée vers le rouge dû aux effets de spill-out, [1, 18, 88]

$$\tilde{\omega}_n = \omega_n\sqrt{1 - \frac{N_{n,\rm out}}{N_n}}, \quad \omega_n = \sqrt{\frac{N_n e^2}{a_n^3 m_{\rm e}}}. \quad (6)$$

$\mathbf{R}_n$ et $\mathbf{P}_n$ à l'Eq. (5) sont respectivement le centre de masse et l'impulsion du plasmon de la n-ième nanoparticule. Introduisant une description en seconde quantification avec des opérateurs d'annhilation (création) pour les plasmons de la nanoparticule n dans la direction $\hat{\sigma}$ b_n^σ ($b_n^{\sigma\dagger}$), nous diagonalisons le hamiltonien plasmonique utilisant des transformations de Bogoliubov. Pour celà, nous utilisons une méthode proposée par Tsalis [90] pour des hamiltoniens bosoniques quadratiques. Cette diagonalisation donne alors la forme des fréquences propres des modes plasmoniques couplés

$$\omega_\alpha^\sigma = \sqrt{\frac{(\tilde{\omega}_1+\tilde{\omega}_2)^2}{4} + \alpha\sqrt{\frac{(\tilde{\omega}_1^2-\tilde{\omega}_2^2)^2}{4} + 4\eta_\sigma^2\Omega^2\tilde{\omega}_1\tilde{\omega}_2}}, \quad (7)$$

avec $\alpha = \pm$, $\eta_{x(y)} = 1$, $\eta_z = -2$ et

$$\Omega = \frac{1}{2}\prod_{n=1}^{2}\left[\frac{\tilde{\omega}_n}{1 - N_{\mathrm{out},n}/N_n}\right]^{1/2}\left(\frac{a_n}{d}\right)^{3/2}. \tag{8}$$

Nos résultats obtenus pour les fréquences et vecteurs propres confirment ceux présentés dans la littérature scientifique (i.e. évolution de l'énergie propre en fonction de la distance d entre les particules en d^{-3} provenant de l'intéraction dipôle-dipôle) [71, 73, 75]. Les modes propres obtenus sont de deux natures: symétriques (i.e. plasmons orientés parallèlement) qui sont fortement couplés à la lumière et donc dénommé modes lumineux; et anti-symétriques (i.e. plasmons orientés anti-parallèlement) couplés faiblement à la lumière et dits modes sombres.

À la section 3.3, nous utilisons les résultats du chapitre 2 pour obtenir les expressions analytiques de l'amortissement Landau des modes collectifs

$$\gamma_{\pm}^{\sigma,\mathrm{L}} = \sum_{n=1}^{2}\frac{3v_{\mathrm{F}}^{n}}{4a_n}\Delta u_{\pm,n}^{\sigma 2}\left(\frac{\omega_n}{\omega_{\pm}^{\sigma}}\right)^3 g\left(\frac{\hbar\omega_{\pm}^{\sigma}}{E_{\mathrm{F}}^{n}}\right), \tag{9}$$

où $g(\nu)$ est la fonction définie à l'Eq. (3) et

$$\Delta u_{n\pm}^{\sigma} = u_{n\pm}^{\sigma} - \bar{u}_{n\pm}^{\sigma}, \tag{10}$$

avec

$$u_{n,\alpha}^{\sigma} = \mathrm{sign}[\alpha\eta_\sigma]^{n-1}\frac{\omega_\alpha^\sigma + \tilde{\omega}_n}{2\sqrt{\tilde{\omega}_n\omega_\alpha^\sigma}}\sqrt{\frac{\omega_\alpha^{\sigma 2} - \tilde{\omega}_{\hat{n}}^2}{2\omega_\alpha^{\sigma 2} - \tilde{\omega}_1^2 - \tilde{\omega}_2^2}}, \tag{11}$$

et

$$\bar{u}_{n,\alpha}^{\sigma} = \mathrm{sign}[\alpha\eta_\sigma]^{n-1}\frac{\omega_\alpha^\sigma - \tilde{\omega}_n}{2\sqrt{\tilde{\omega}_n\omega_\alpha^\sigma}}\sqrt{\frac{\omega_\alpha^{\sigma 2} - \tilde{\omega}_{\hat{n}}^2}{2\omega_\alpha^{\sigma 2} - \tilde{\omega}_1^2 - \tilde{\omega}_2^2}}, \tag{12}$$

où $\hat{n} = 1(2)$ pour $n = 2(1)$.

L'expression analytique de l'amortissement radiatif des modes collectifs est présentée à la section 3.4:

$$\gamma_{\pm}^{\sigma,\mathrm{r}} = \frac{2\omega_{\pm}^{\sigma 3}}{3c^3}\left(\sum_{n=1}^{2}\sqrt{\omega_n a_n^3}\Delta u_{n,\pm}^{\sigma}\right)^2, \tag{13}$$

où $\Delta u_{n,\pm}^{\sigma}$ est défini à l'Eq. (10).

Dans le cas d'un dimère homogène, le taux de décroissance du mode sombre est nul tandis que celui du mode brillant est deux fois plus important que celui d'une nanoparticule unique. Dans le cas d'un dimère hétérogène, le mode sombre irradie toujours. De plus, pour une polarisation longitudinale, l'amortissement radiatif du mode lumineux augmente en augmentant la distance séparant les nanoparticules jusqu'au point qu'il dépasse en intensité l'amortissement Landau du mode.

Les résultats présentés au chapitre 3 sont en excellent accord avec les résultats expérimentaux existants [79, 80, 85, 86] ainsi qu'avec les calculs numériques [75], ceci encourageant donc l'utilisation de notre modèle analytique.

Le chapitre 4 est consacré à l'étude d'une chaîne homogène de nanoparticules. Nous commençons par étendre le hamiltonien (1) du système en ajoutant le forçage électrique externe nécessaire pour décrire correctement les expériences,

$$H = H_{\mathrm{pl}} + H_{\mathrm{eh}} + H_{\mathrm{pl-eh}} + H_{\mathrm{ph}} + H_{\mathrm{pl-ph}} + H_{\mathrm{drive}}. \tag{14}$$

Considérant une chaîne finie, nous utilisons alors une transformation sinusoïdale

$$b_n^\sigma = \sqrt{\frac{2}{\mathcal{N}+1}} \sum_q \sin(nqd)\, b_q^\sigma, \tag{15}$$

et une transformation de Bogoliubov

$$B_q^\sigma = \cosh\theta_q^\sigma b_q^\sigma + \sinh\theta_q^\sigma b_q^{\sigma\dagger}, \tag{16}$$

afin d'obtenir les modes propres des plasmons collectifs, montrant ainsi la relation de dispersion déjà calculée dans la littérature [40]

$$\omega_q^\sigma = \omega_0 \sqrt{1 + 4\eta_\sigma \frac{\Omega}{\omega_0} \cos(qd)}. \tag{17}$$

Les opérateurs B_q^σ ($B_q^{\sigma\dagger}$) détruisent (créent) un plasmon collectif avec une impulsion q dans la direction $\hat{\sigma}$.

Utilisant ces modes propres des plasmons collectifs, nous dérivons une équation maîtresse pour la matrice densité des degrés de libertés plasmoniques pour la polarisation $\sigma = x, y, z$ ρ^σ. Dans cette dérivation, nous nous plaçons dans la limite de faible couplage ainsi que dans une approximation de processus markoviens.

L'approximation de faible couplage permet d'assurer que les intéractions entre les plasmons et les bains ne changent pas les états de ces bains. L'hypothèse markovienne permet de prendre en compte le fait que le temps caractéristique d'évolution du système est bien plus élevé que le temps de corrélation des électrons présents dans le système plasmonique.

L'équation maîtresse donne alors

$$\begin{aligned}
\dot{\rho}^\sigma = &- \mathrm{i} \sum_q \tilde{\omega}_q^\sigma \left[B_q^{\sigma\dagger} B_q^\sigma, \rho^\sigma\right] \\
&- \sum_q \frac{\gamma_q^\sigma}{2} \left(B_q^{\sigma\dagger} B_q^\sigma \rho^\sigma + \rho^\sigma B_q^{\sigma\dagger} B_q^\sigma - 2 B_q^\sigma \rho B_q^{\sigma\dagger}\right) \\
&+ \mathrm{i} \sum_q \frac{\mathcal{A}_q^\sigma f(t)}{2\tilde{\omega}_q^\sigma} \left[B_q^{\sigma\dagger} + B_q^\sigma, \rho^\sigma\right],
\end{aligned} \tag{18}$$

où l'amplitude $\mathcal{A}_q^\sigma$ est donnée par

$$\mathcal{A}_q^\sigma = -2\sqrt{\frac{2}{\mathcal{N}+1}}\hat{\sigma}\cdot\hat{\epsilon}\sin(qd)\,\Omega_{\mathrm{R}}\tilde{\omega}_q^\sigma\sqrt{\frac{\omega_0}{\omega_q^\sigma}}. \tag{19}$$

Cette équation maîtresse (18) est obtenue sous la forme de Lindblad, avec des taux de décroissance obtenus avec les règles d'or de Fermi.

Évaluant la règle d'or de Fermi pour les taux de décroissances présents dans l'équation (18) nous obtenons pour l'amortissement Landau

$$\gamma_q^{\sigma,\mathrm{L}} = \frac{3v_{\mathrm{F}}}{4a}\left(\frac{\omega_0}{\omega_q^\sigma}\right)^4 g\left(\frac{\hbar\omega_q^\sigma}{E_{\mathrm{F}}}\right), \tag{20}$$

et l'amortissement radiatif

$$\gamma_q^{\sigma,\mathrm{r}} = \frac{3\pi|\eta_\sigma|\gamma_0^{\mathrm{r}}}{4k_0 d}\,\frac{\left(\omega_q^\sigma\right)^2+\mathrm{sgn}\{\eta_\sigma\}\left(cq\right)^2}{\omega_0\omega_q^\sigma}\,\Theta\left(\omega_q^\sigma-cq\right), \tag{21}$$

des plasmons collectifs d'une chaîne homogène infinie.

Les amortissements radiatifs obtenus (21) sont en excellent accord avec les précédents résultats numériques obtenus [46], montrant une nette séparation entre des modes super-radiants (i.e. taux de décroissance supérieur à celui de la nanoparticule unique) et sub-radiants (i.e. taux de décroissance inférieur à celui de la nanoparticule unique).

À la section 4.4, nous utilisons l'équation maîtresse (18), où nous ajoutons phénoménologiquement les pertes Ohmiques afin de dériver des équations du mouvement pour des moments dipolaires adimensionnés dans l'espace réciproque,

$$\ddot{\sigma}_q + \gamma_q^\sigma\dot{\sigma}_q + \Omega_q^{\sigma\,2}\sigma_q = \mathcal{A}_q^\sigma f(t), \tag{22}$$

avec $\Omega_q^{\sigma 2} = \tilde{\omega}_q^{\sigma 2} + (\gamma_q^\sigma/2)^2$, et où l'amplitude du terme de forçage $\mathcal{A}_q^\sigma$ est défini par l'Eq. (19).

Nous considérons ensuite deux scénarios de propagation plasmonique : à la section 4.4.1 nous étudions le cas d'un forçage électrique continu et monochromatique, et dans la section 4.4.2 celui d'une courte impulsion laser pour exciter le plasmon.

Les calculs numériques dans le cas d'un forçage continu pour une chaîne de 1000 nanoparticules d'argent (Figure 2(a)-(d)), montrent distinctement deux régimes quasistatiques. Pour des courtes distances, les excitations décroissent de façon exponentielle pour décroîtrent algébraïquement pour des distances plus importantes. L'ajustement des lois de puissances pour les décroissances algébraïques donnent les exposants 1 (2) pour les modes transverses (longitudinaux). Le changement d'une décroissance exponentielle à une de type algébraïque est une conséquence du comportement discontinu de l'amortissement radiatif en fonction de l'impulsion des plasmons. Ainsi, la décroissance exponentielle tire

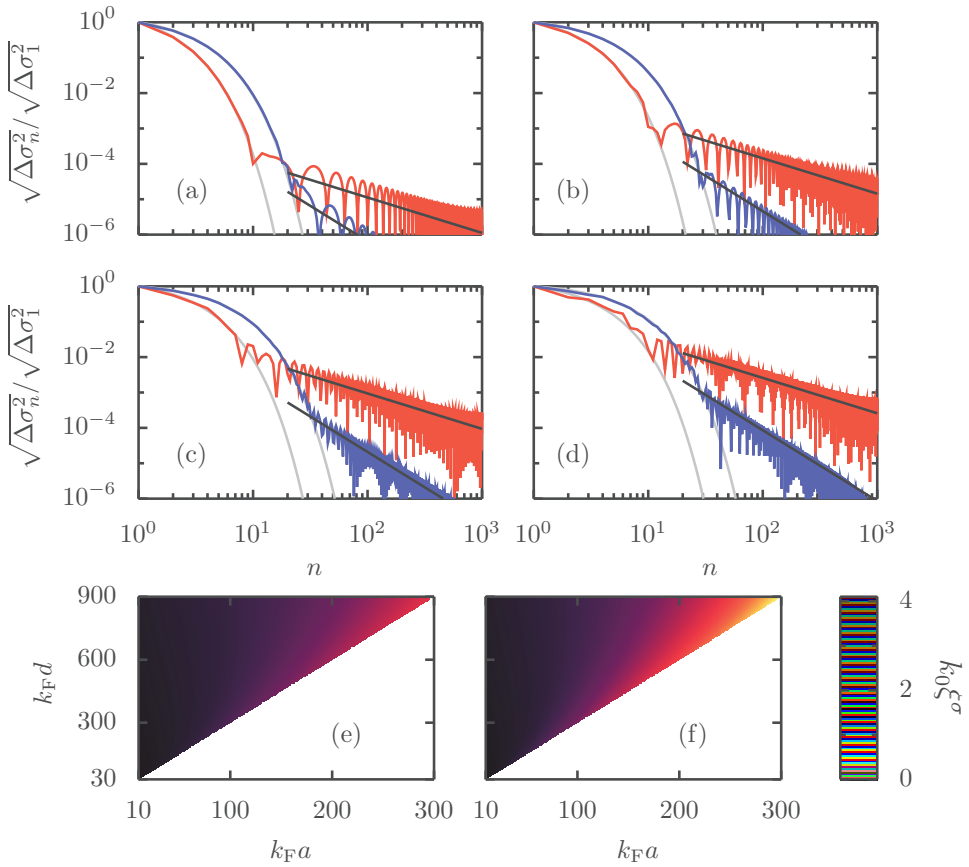

Figure 2: (a)-(d) Ecart type moyenné dans le temps et normalisé du moment dipôlaire présent sur la nanoparticule n résultant d'une excitation monochromatique à la fréquence $\omega_\mathrm{d} = \omega_0$ de la 1ère nanoparticule d'une chaîne de $\mathcal{N} = 1000$ particules avec une distance entre les particules de $d = 3a$. Les lignes en pointillés rouges et bleues correspondent respectivement aux solution numériques de l'équation (22) pour les modes transverses et longitudinaux en incluant les pertes ohmiques, Landau et radiatives. Les pointillés épais et les lignes grises correspondent aux résultats analytiques qui ne prennent pas en compte l'amortissement radiatif, i.e. pertes Ohmiques et Landau. Les tailles des nanoparticules sont (a) $k_\mathrm{F}a = 50$, (b) $k_\mathrm{F}a = 100$, (c) $k_\mathrm{F}a = 200$, et (d) $k_\mathrm{F}a = 300$. Les lignes noires pleines et pointillées sont les ajustements algébraïques pour les modes transverses et longitudinaux respectivement (voir texte). (e)-(f) Longueur de propagation ξ^σ d'aprés l'Eq. (23) pour les modes (e) transverses (f) et longitudinaux en fonction a et d. Les paramètres choisis pour la figure sont $\gamma^\mathrm{a}/\omega_0 = 0.027$, $\hbar\omega_0/\mathrm{E_F} = 0.47$, et $\omega_0/ck_\mathrm{F} = 1.1 \times 10^{-3}$, correspondant à une chaîne de nanoparticules d'argent. Les décalages fréquenciels (Lamb) sont ici négligés.

uniquement son origine de processus non-radiatifs. Utilisants celà et négligeant l'amortissement radiatif (qui ne contribue qu'a la décroissance

algébraïque), nous avons calculé de manière analytique les expressions de l'amplitude et de la longueur de propagation liées à la propagation des plasmons

$$\xi^{\sigma} = \frac{d}{\operatorname{arcsinh}(\gamma^{\mathrm{nr}}/4|\eta_{\sigma}|\Omega)}, \tag{23}$$

où $\gamma^{\mathrm{nr}} = \gamma_0^{\mathrm{L}} + \gamma^{\mathrm{a}}$ est la partie non-radiative de l'amortissement d'une nanoparticule unique.

Dans le cas d'une impulsion laser de courte durée, nous avons testé le fait que l'amortissement radiatif n'influence que faiblement la propagation de l'impulsion (Figure 3). Ainsi, nous avons calculé, comme dans le cas du forçage continu, les expressions analytiques des moments dipôlaires locaux.

De nos résultats, nous pouvons conclure que même si la propagation plasmonique est possible et pourrait être détectée, l'atténuation des excitations est suffisamment importante pour rendre la détection sur grande distance inutile [11]. Cependant, il a été avancé dans la littérature que l'utilisation des plasmons collectifs pour la transmission de signaux [37, 40] ne serait que possible pour des relativement courtes distances. Notre travail permet donc à partir de notre modèle de trouver des moyens de minimiser les pertes qui limitent les possibles applications de réseaux de nanoparticules [11].

Pour conclure, notre approche basée sur un système quantique ouvert peut s'adapter à tout types de réseaux réguliers de nanoparticules métalliques, donnant ainsi un grand nombre de possibilités pour de potentielles applications. Utilisant uniquement quelques approximations, nous avons été capables d'appréhender la physique de la propagation et de l'amortissement des plasmons collectifs dans des chaînes de nanoparticules métalliques. De plus, le fait d'utiliser une description quantique nous à permis d'inclure l'amortissement Landau, qui constitue un élément essentiel de la description du temps de vie des plasmons dans des nanoparticules de petites tailles.

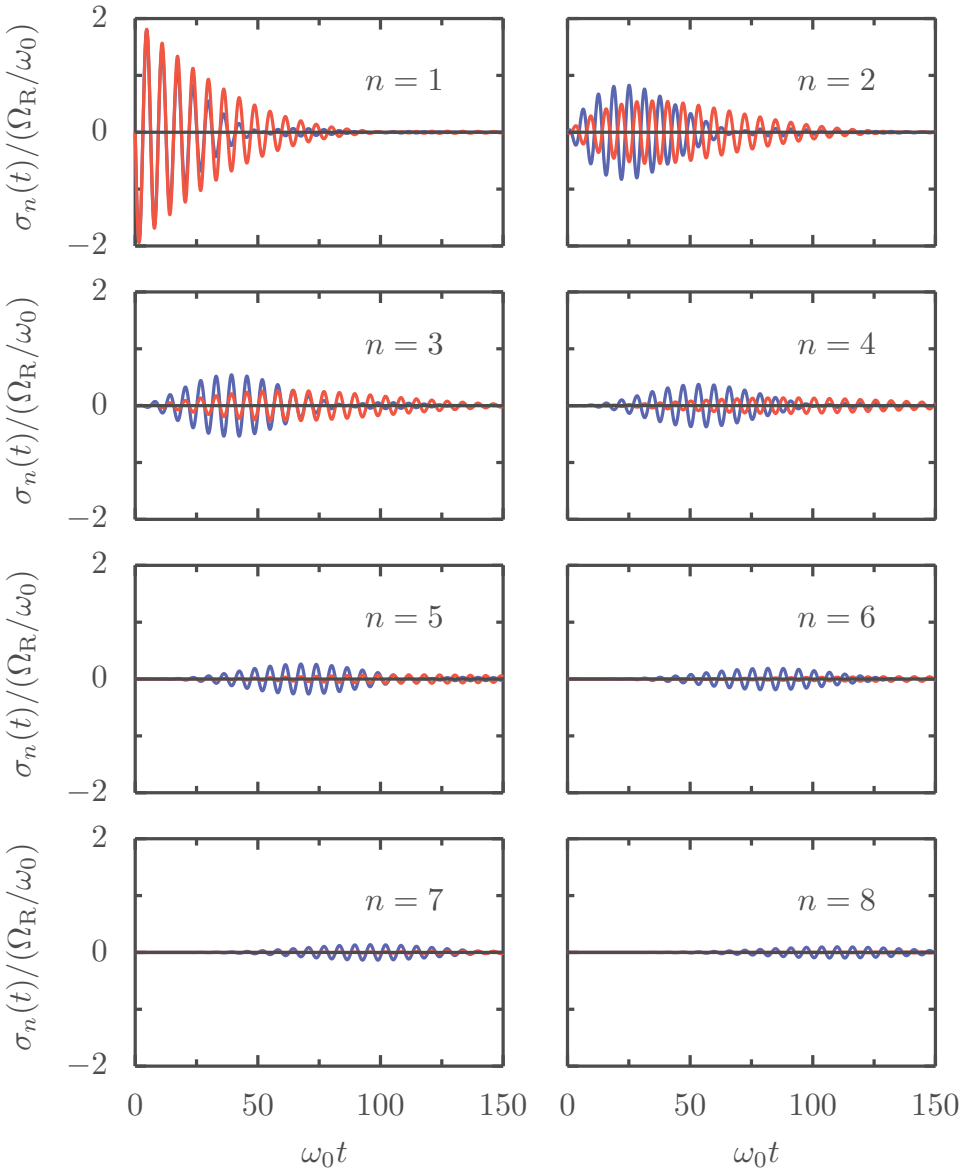

Figure 3: Moment dipolaire de la nanoparticule n en fonction du temps résultant d'une impulsion laser de courte durée sur la première nanoparticule. Les modes transverses et longitudinaux sont respectivement représentés en pointillés rouges et en lignes bleues. Les paramètres dans la figure correspondent à ceux d'une chaîne infinie de particules d'argent de rayons $a = 200\ k_F^{-1} = 16.6$ nm et séparées d'une distance $d = 3a$.

Chapter 1

Introduction

The very peculiar optical properties of small metallic objects are at the origin of the spectacular advances recently achieved in the field of nanophotonics [1–4]. The collective oscillations of the conduction electrons are responsible for these optical properties. These excitations, where the electronic charge oscillates at a metal surface or within a nanostructure are generally referred to as *surface plasmon* resonances [3]. In the first case, [5] the plasmons propagate along the metal-dielectric interface and have non-zero momentum. The focus of our work will be the second case of metallic nanoparticles, where plasmons become confined yielding an oscillating pile up of the electronic charge at the interface with the surrounding dielectric, and are referred to as *localized surface plasmons* (LSPs). Using the shorter terminology of surface plasmons is usually adopted when there is no possibility of confusion with the surface-propagating oscillations.

LSPs are of particular interest in confining light at the nanoscale. Their dynamics can be resolved in time in pump-probe experiments [6]. In terms of applications the usage of the LSPs can range from spectroscopy to the realization of *metamaterials* [3]. On the one hand, the local spectroscopy benefits from the high electric field intensities present in the vicinity of the nanoparticle, as used for the surface enhanced Raman scattering (SERS) of molecules [7]. This effect can be even further enhanced due to the interaction between LSPs [8]. On the other hand, the LSPs in nanoparticle arrays may be exploited to achieve new materials with unusual optical properties (i.e. metamaterials). This feature is of particular interest for developing *plasmonic circuitry* [2], as well as for fundamental research on novel physical states, such as massless Dirac bosons originating from arrays of metallic nanoparticles arranged on a honeycomb lattice [9, 10].

Although plasmonics with the use of LSPs has many potential applications, it is highly susceptible to losses present in its metallic components [11]. These losses are the main reason for limitations of the use of nanoparticle arrays for practical purposes. Thus, understand-

ing the mechanisms behind them is of great importance for the field of plasmonics.

While the scientific research on LSPs (plasmons for short) spans over a century [12] their application goes even further to ancient times [13]. Going from the single nanoparticle case [1,12,14–35] to the state where a regular array of nanoparticles was achieved [36–67] defines a rich research field with various points to advance in an understanding of light-matter interaction at the nanoscale. Thanks to the advancement in the miniaturization procedures [63], scientists are now able to fabricate nanoparticle arrays with given regular spacings and controlled material properties. Such advancements give the possibility to develop and test our theoretical concepts, helping in the design of novel materials with interesting optical features.

1.1 Localized surface plasmon

The initial theoretical research on the optial properties of a single spherical particle was done in 1908 by Mie [12]. Using Maxwell's equations the author showed the method of obtaining the extinction spectrum for a spherical dielectric sphere. Using the appropriate dielectric function, one is able to adapt the method for metals. In addition, under the condition that the radius of the sphere is much smaller than the wavelength of the incoming light, one obtains a condition for the resonance in the extinction spectrum. This condition, using the Drude model for the dielectric function [5], leads to the following expression for the resonance frequency of the metallic sphere (corresponding to the dipolar plasmon):

$$\omega_0 = \frac{\omega_\mathrm{p}}{\sqrt{\epsilon_\mathrm{d} + 2\epsilon_\mathrm{m}}}. \tag{1.1}$$

The above mentioned frequency is called the Mie frequency, where $\omega_\mathrm{p} = \sqrt{4\pi n_\mathrm{e} e^2/m_\mathrm{e}}$ is the plasmon frequency of the metal, with n_e, e and m_e standing for the electron density, charge and mass, respectively. ϵ_d is the correction to the dielectric constant of the metal coming from the screening of d electrons, while ϵ_m is the dielectric function of the embedding medium. In the case of alkali metals in vacuum, the Mie frequency simplifies to $\omega_0 = \omega_\mathrm{p}/\sqrt{3}$.

The investigation of electron dynamics in an isolated nanoparticle can be performed using various theoretical approaches out of which the most relevant for us is the open quantum system approach [14,17,19,22, 24–27,30]. Another useful method is based on density functional theory [33]. A different theoretical approach to the electron dynamics in an isolated metallic nanoparticle incorporates a quantum hydrodynamic model [31,35,68].

The plasmon resonance described by Mie's theory has a finite linewidth, as observed in the experiments (see Figure 1.1) [20]. Figure 1.1 (repro-

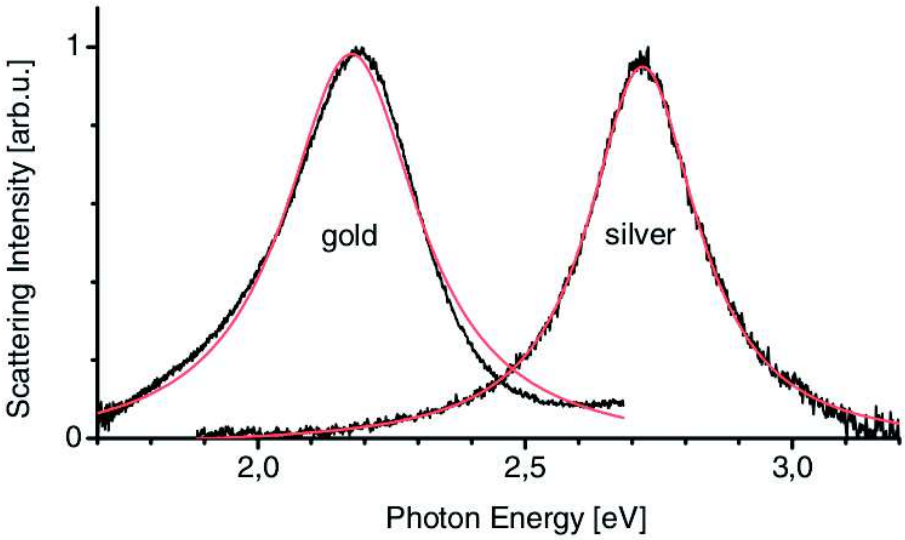

Figure 1.1: The black curves show light-scattering spectra from a single gold and a single silver cluster with 60nm diameter. The red curves show Lorentzian fits to the spectra. Reproduced from Ref. [20]

duced from Ref. [20]) shows examples of the light-scattering spectra from single gold and silver nanoparticles. The observed spectra show a clear resonance with an envelope fitting almost perfectly to a Lorentzian function. The width of the resonance was associated with the Ohmic (or absorption) losses in the metal (described by the decay rate γ^{a}) due to inelastic scattering of electrons based on classical conductivity theory [5]. Nevertheless there exist additional sources of energy dissipation which lead to linewidths that depend on the size of the nanoparticle (see Figures 1.2 and 1.3).

Figure 1.2 (reproduced from Ref. [20]) shows scattering spectra of single particles with different sizes (ranging from 20 to 150 nm). In the figure we observe a tendency of the linewidth to increase with increasing size of the particles. Figure 1.3 (reproduced from Ref. [28]) shows the dependence of the spectral width on the inverse diameter $1/D_{\mathrm{eq}}$. We observe two regimes (i) for particles smaller than 20 nm the spectral width increases with decreasing size, and (ii) for particles larger than 20 nm the spectral width increases with increasing size. These two regimes are linked to two size-dependent mechanisms of damping.

Among the two size-dependent sources of the damping, is a classical phenomenon associated with the accelerated charges [70], this corresponds to the *radiative losses* (i.e. radiation damping). The magnitude of the radiation damping is proportional to the number of electrons in the nanoparticle, and therefore it scales as a^3, where a is the nanoparticle radius. Thus, this mechanism is increasingly important for relatively large nanoparticles with $a > 15$ nm (see Figures 1.2 and 1.3).

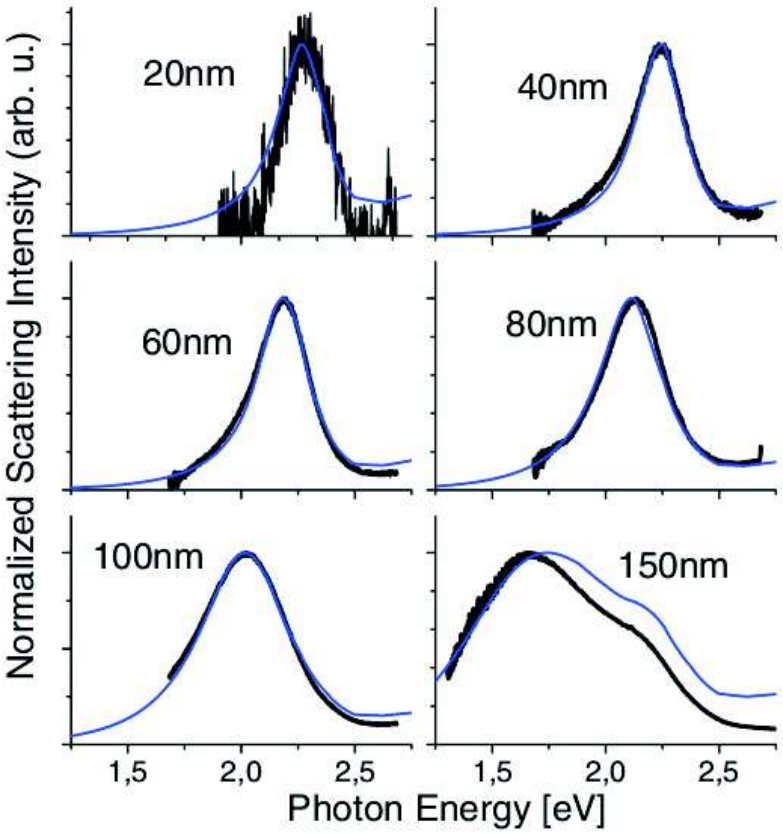

Figure 1.2: Scattering spectrum of single particles for various particle sizes (black curves). The cluster diameters are indicated. The blue curves show the result of Mie theory calculations using the dielectric function of gold from Ref. [69]. Reproduced from Ref. [20].

The other relevant size-dependent mechanism, called *Landau damping*, was first studied theoretically by Kawabata and Kubo in finite-size metallic clusters [14] using their linear response theory. It describes a process in which a plasmon is decaying by creating particle-hole pairs. This process results in a damping governed by a rate

$$\gamma^{\mathrm{L}} = \frac{3v_{\mathrm{F}}}{4a} g_{\mathrm{KK}} \left(\frac{\hbar\omega_0}{E_{\mathrm{F}}} \right), \tag{1.2}$$

with v_{F} and E_{F} being the Fermi velocity and energy, respectively. Note that γ^{L} scales as a^{-1} and becomes important for small nanoparticles with $a < 10$ nm (see Figure 1.3). The function

$$g_{\mathrm{KK}}(\nu) = \nu^{-3} \int_{\nu_0}^{1} \mathrm{d}x \, [x^3(x+\nu)]^{1/2}, \tag{1.3}$$

with $\nu_0 = 1 - \nu$ and 0 for $\nu < 1$ and $\nu > 1$, respectively. This function was later corrected by Ruppin and Yatom [15] for a missing factor of

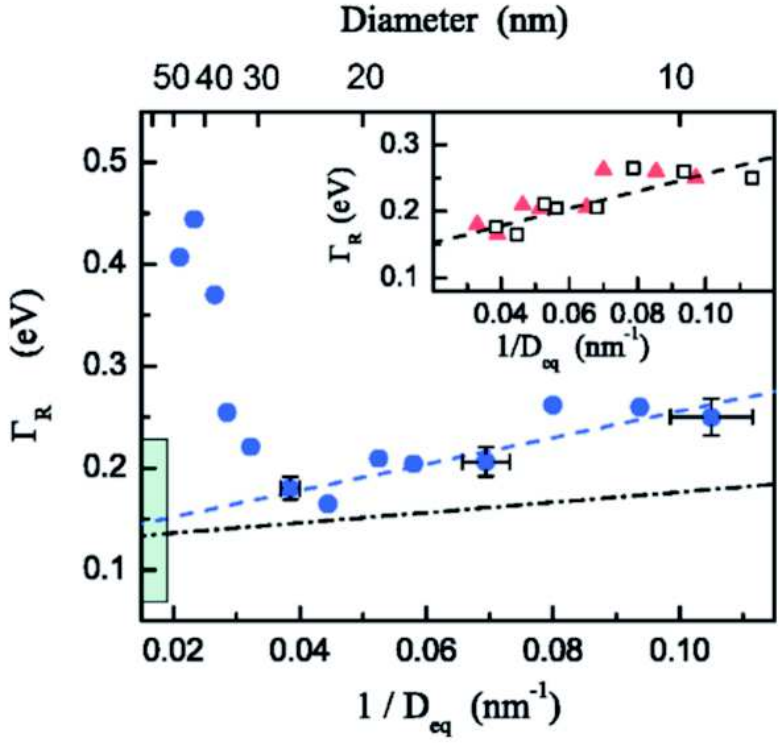

Figure 1.3: Spectral width Γ_{R} of the LSP resonance in different single Ag nanoparticles embedded in SiO_2 matrix, as a function of the inverse diameter $1/D_{\mathrm{eq}}$. Reproduced from Ref. [28].

π, and further corrected by Yannouleas and Broglia [17] to incorporate corrections due to the used asymptotes of Bessel function in Ref. [14]. Moreover, the result in Eq. (1.2) was later further refined as to include the oscillations of the linewidth as a funciton of nanoparticle size and the effect of the embedding matrix [19, 22, 24–26]. The presence of two different size-scalings between the cases of radiation and Landau damping is a key ingredient for the optical properties of metallic nanoparticles and play a key role in the minimization of the total width (i.e. maximization of the plasmon lifetime).

1.2 Nanoparticle dimers

The extension to the collective excitation studies in a system constituted by a particle dimer was performed [71] 74 years after the founding paper of Mie [12]. In dimer structures, the interaction between individual plasmons on each nanoparticle gives rise to symmetric and anti-symmetric modes. The former are strongly coupled to light, and are thus referred to as *bright* modes in the literature. The latter are

weakly coupled to the light, and thus called *dark* modes.

The theoretical description of these coupled plasmonic modes has been performed through various methods [71–78]. One possible approach is to start from the Mie theory and use Maxwells's equations [71,72] in order to obtain the energies of the modes. The lack of spherical symmetry in the case of dimers renders the calculations involved, which cannot be carried in an exact way, but need to be approximate or numerically computed. The advantage of the Mie approach is that it includes effects of the multipolar plasmon resonances. A simplified approach proposed by Nordlander *et al.* [73] was used to obtain plasmon hybridization. In their work, the authors showed that the collective modes of the nanoparticle can be viewed as *bonding* and *antibonding* states composed of the individual plasmons, which have lower and higher energy, respectively. Using their model they obtained the energy levels of the coupled plasmonic modes as well as their dependence on the interparticle distance.

Aside for the studies of the energy eigenstates of the system, the lifetime of the collective plasmons plays an important role limiting any potential nanoplasmonic applications [11]. The changes in radiation damping with respect to the case of a single nanoparticle were studied by Dahmen *et al.* [74], using a dipolar approximation. This approach resulted in an oscillatory behavior of the radiation linewidth as a function of the interparticle distance. These results were also confirmed by Smith [76].

Studies including Landau damping were performed in Ref. [75], through the use of time-dependent local density approximation (TDLDA) calculations. The results of these calculations are presented in Figure 1.4 (reproduced from Ref. [75]). The figure shows optical absorption of the homogeneous dimer with radius $R = 16\ a_0$ (left panel in Figure 1.4) and $R = 24\ a_0$ (right panel in Figure 1.4) for different interparticle separations d, with a_0 being one Bohr radius. From the spectra we can observe a shift of the plasmon resonances and a change in their widths with decreasing separation (from upper curve down). Although TDLDA captures the effect of Landau damping, it does not show what is the effect of the interaction between plasmons in different nanoparticles onto the damping. The advantage of this numerical technique is that it includes the tunneling effects that may occur for nanoparticles that are almost touching each other. In such cases, a new plasmonic resonance, called a *charge transfer plasmon*, appears (see bottom curves in Figure 1.4).

Up to the initiation of our studies, there was no complete survey of the influence of the interaction between plasmons onto the damping mechanisms occurring in nanoparticle dimers. In Chapter 3 we present such a study based on a model which incorporates both radiation and Landau damping in a self-contained way.

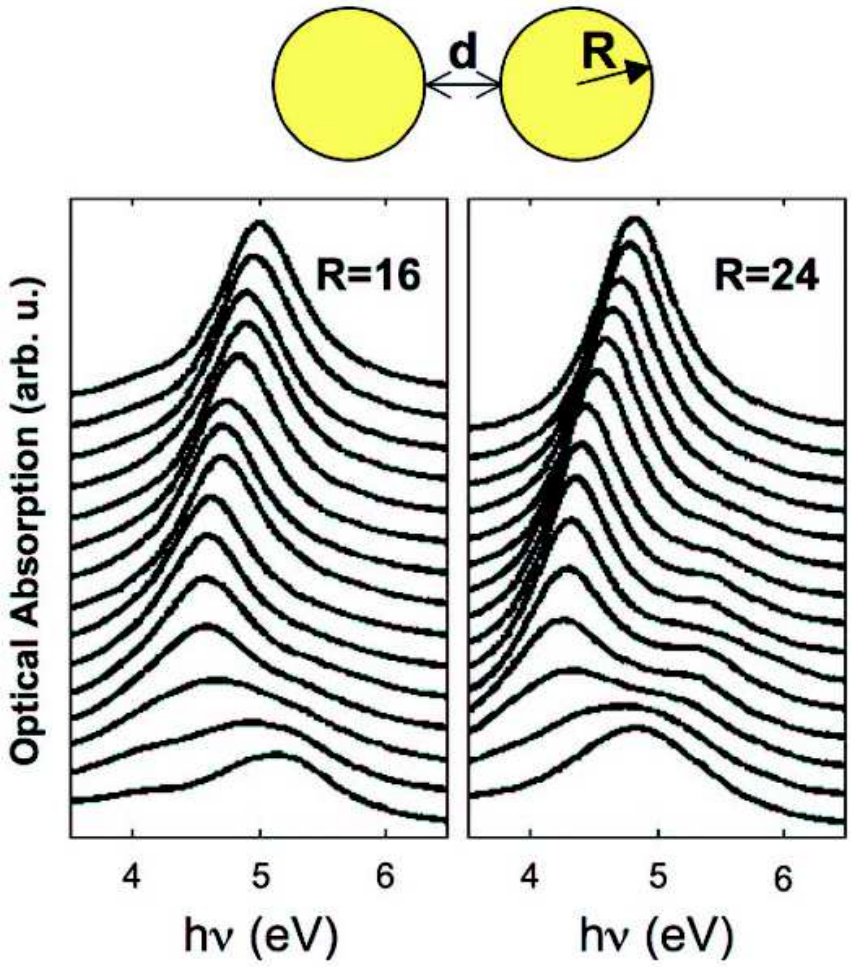

Figure 1.4: TDLDA absorption spectra for $R = 16\ a_0$ (left panel) and $R = 24\ a_0$ (right panel) for different separations $d = 0, 1, 2, 3, 4, 5, 6, 7, 8, 10, 12, 14, 16, 20$, and $24\ a_0$ (from bottom curve up), where a_0 is one Bohr radius (0.0529 nm). Reproduced from Ref. [75].

On the experimental front, thanks to the advancement in the fabrication techniques, nanoparticle dimers with very small sizes and separations have been achieved [79–86]. Using lithographic methods, Jain *et al.* [81,86] managed to fabricate metallic nanodisk pairs with controlled interparticle separation. The results of the absorption experiment performed on these samples are presented on Figure 1.5. Figure 1.5 (a) shows a transmission electron micrograph of lithographically-fabricated nanodisc dimers with diameters of 44 nm and controlled interparticle separation. Figure 1.5(b) shows the extinction spectra of these dimers for a longitudinal polarization and varying separation. One can observe a decrease of the plasmon energy and its linewidth with increasing separation. Figure 1.5(c) presents the extinction spectra of the fabricated dimers for the transverse polarization. From the figure one finds a slight increase of the plasmon energy and decrease of its linewidth with

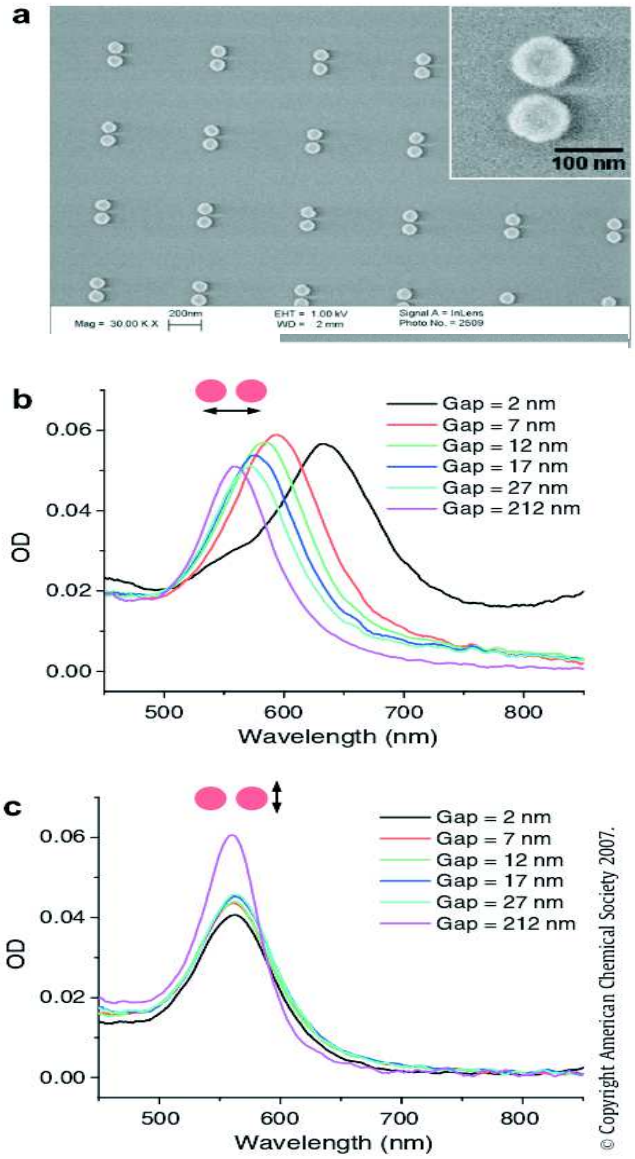

Figure 1.5: (a) Lithographically-fabricated array of 88 nm diameter gold nanodisc pairs with controlled interparticle separation, in this case 12 nm (inset is a magnified SEM image clearly showing the interparticle gap). Extinction spectra show that LSP resonance of the particle pair (b) red-shifts with decreasing gap for polarization along the interparticle axis. (c) Blue-shifts very slightly with decreasing gap for polarization orthogonal to the interparticle axis. Reproduced from Ref. [81].

increasing separation.

Other authors studied [79, 80] the characteristics of the symmetric modes with polarization parallel (longitudinal) and orthogonal (trans-

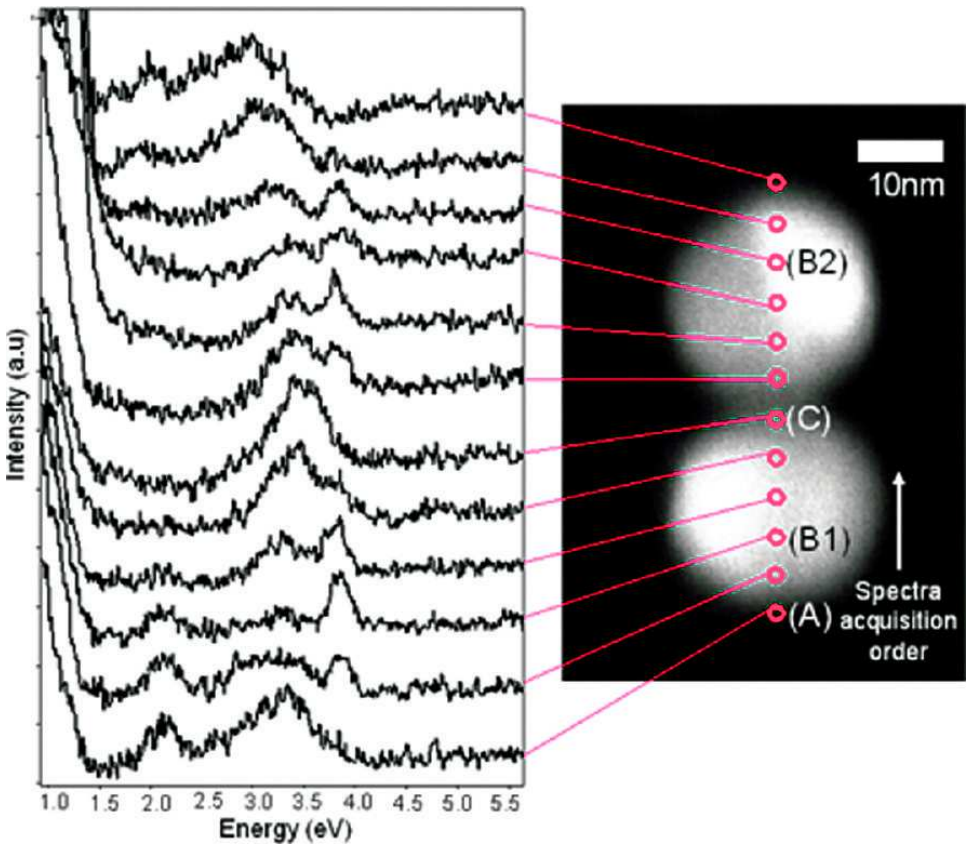

Figure 1.6: Experimental EELS data set of a symmetrical silver nanoparticle dimer, showing plasmon energies as a function of electron probes position. The spectra are obtained at regular intervals of 4 nm. Reproduced from Ref. [85].

verse) to the interparticle axis confirming earlier theoretical developments. Nevertheless, those experiments using light as the excitation, have a major setback, which is their inability to excite the anti-symmetric modes (the dipole moment of homogeneous dimers is zero and almost zero in the case of heterogeneous dimers). This setback was solved with the introduction of the experimental technique called *electron energy loss spectroscopy* (EELS) [84, 85]. In an EELS experiment, a beam of electrons is sent in the vicinity of the particles and, due to the interaction of the nanoparticle electrons with the electric field induced by the electron beam, a plasmon may be exited. Since the interaction is repulsive, placing the beam in the space between the nanoparticles will excite the antisymmetric (dark) mode. Moreover, the spatial mapping of the bright and dark modes is also possible using EELS. An example of the EELS spectra from Ref. [85] is presented in Figure 1.6. In this figure the EELS spectra for different positions of the electron beam are presented. At position (A) of the beam (the lowest and uppermost curve) we observe the resonance corresponding to the bright mode with

longitudinal polarization. In position (B1) and (B2) of the beam we see small peaks at around 3.6 eV identified by the authors as the bulk plasmon. The plasmon resonance of the dark mode can be seen for the electron beam in position (C).

The dimer structures, besides their own interesting applications set a good starting point toward the study of more complex arrays such as nanoparticle chains.

1.3 Theoretical approaches on plasmon guiding

The proposal of using a chain of metallic spherical nanoparticles as a sub-wavelength-scale light guide was issued in 1998 by Quinten *et al.* [37]. The transmission of the electromagnetic energy results from the electromagnetic coupling between the particles. Using the generalized Mie theory [36], the authors of Ref. [37] obtained the equations for the expansion coefficients (in the basis of the vector spherical harmonics) of the electromagnetic wave scattered by the metallic nanoparticle chain in the case where the incoming field is a plane wave absorbed by the first nanoparticle. Solving these equations for the chain of $\mathcal{N}$ identical nanoparticles separated by a distance d and using a superposition of the obtained scattered fields, they were able to calculate the intensity of the electromagnetic field along the chain.

As an example Quinten *et al.* calculated an intensity of the electric field for a chain of 50 Ag nanoparticles with radii 25 nm [37]. The resulting intensity followed an exponential decay along the chain (see Figure 1.7). In addition, the authors found that the polarization of the incoming light highly influenced the propagation of the signal along the chain. It was shown that only for a polarization parallel to the chain axis (i.e. longitudinal polarization) the propagation was significant. Moreover, the authors of Ref. [37] tried to determine an optimal interparticle distance maximizing the possible propagation. In Figure 1.7 the results of this study are presented. It was found that the best propagation length (900 nm) was obtained for the interparticle distance $d = 3a$, where a is the radius of the nanoparticles, which corresponds to the uppermost curve in Figure 1.7.

Studies of a similar chain as the one of Ref. [37], as well as structures containing corners and junctions, were conducted by Brongersma *et al.* [40]. These authors used a considerably simpler model of electrostatically coupled point dipoles. It was shown that the equations of motion for these dipoles are these of an ensemble of coupled driven harmonic oscillators, with damping terms due to both radiative and non-radiative losses.

The solution proposed in Ref. [40] was that of a traveling wave.

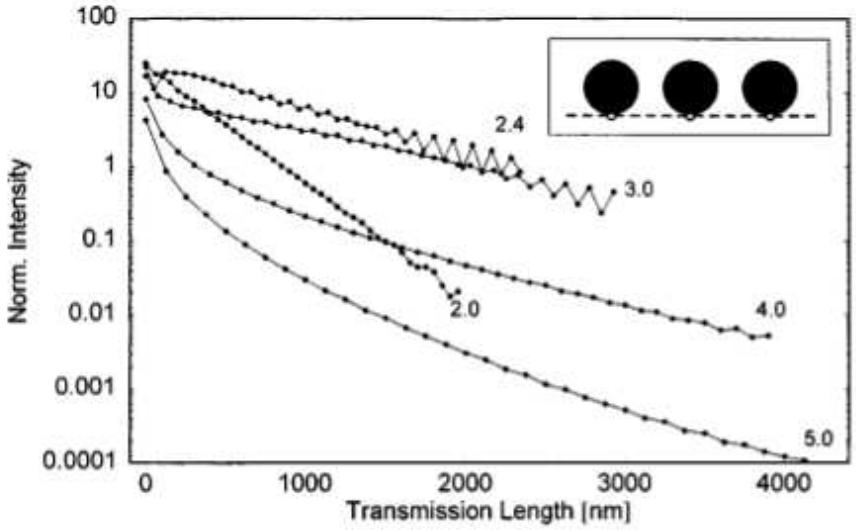

Figure 1.7: Decay of the field intensity in the chain axis direction. Values are taken at identical positions of each particle as shown by the open circles in the inset. The given parameter d_{ij}/a is the ratio of interparticle (center-to-center) distance and particle radius. The intensities are normalized to the irradiated light-field intensity. Note the strong nonexponential decay for $d_{ij}/a > 3$. Reproduced from Ref. [37].

Using as an approximation the small damping limit and assuming that the radiation damping is the same as the one of an isolated nanoparticle, Brongersma *et al.* obtained an analytical form for the dispersion relation for the plasmon frequency as well as an analytical form of the plasmon attenuation. The former was shown to be only weakly dependent on couplings beyond nearest neighbors, while the latter depended on both radiative and non-radiative damping mechanisms. Moreover, these authors argued that the estimation of the radiative losses based on the single oscillating electron proved that the radiative term might be dropped, since it is much smaller than the non-radiative one. In the sequel these authors showed that the above-mentioned approximations led to a similar result for the propagation length as the one found by Quinten *et al.* [37], with the exception that not only the longitudinal but also the transverse modes present a significant propagation. The attenuation coefficients were estimated to be 3dB/500nm for the longitudinal mode and 6dB/500nm for the transverse modes, as compared to 2.4dB/500nm for the longitudinal mode reported in [37].

Later on, within the same group, Maier *et al.* [41, 44] used the finite difference time domain (FDTD) simulation to confirm their point dipole model [40], but using Au nanoparticles instead of Ag ones. Figure 1.8 shows a plasmon pulse propagation along the chain of spherical

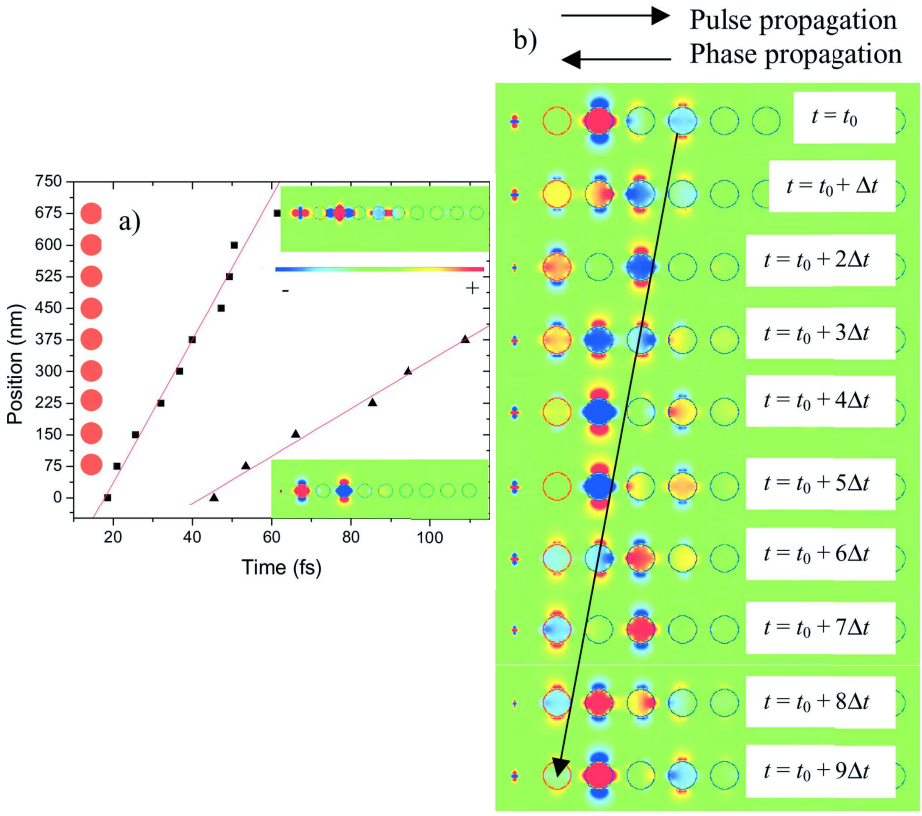

Figure 1.8: (a) Pulse peak position over time in a plasmon waveguide consisting of spherical particles for both longitudinal (black spheres) and transverse (black triangles) polarization. The spheres along the ordinate indicate the position of the Au nanoparticles. Snapshots of the x (y) component of the electric field in the xy plane for longitudinal (transverse) polarization are shown in upper (lower) inset. (b) Time snapshots of the electric field for transverse pulse propagation showing a negative phase velocity with an anti-parallel orientation of the phase and group velocities. Reproduced from Ref. [44].

Au nanoparticles obtained in those studies. In panel (a) of Figure 1.8 a plasmon peak position is depicted for both transverse (black triangles) and longitudinal (black squares) modes showing that the group velocity of the longitudinal mode is higher than the group velocity of the transverse modes. Panel (b) of Figure 1.8 presents time snapshots of the pulse propagation of the transverse mode showing that it has a negative phase velocity. Based on the FDTD simulations Maier *et al.* [44] estimated the attenuation coefficients of the longitudinal and trans-

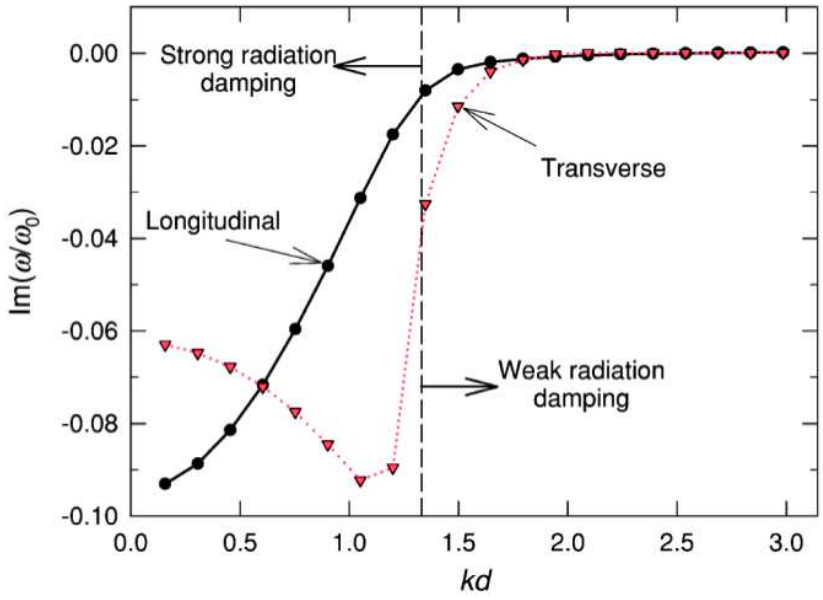

Figure 1.9: Imaginary part of the normal mode frequencies of the full retarded solution for a 20-sphere chain of lossless metal particles. The dashed vertical line corresponds approximately to $k_{\text{mode}} = \omega/c$, with k_{mode} being the plasmon momentum. Reproduced from Ref. [46].

verse modes to be 3dB/140nm and 3dB/43nm, respectively, which are a factor of 2 to 3 higher than their estimates based on the point dipole model. This discrepancy was argued to be due to the finite size of the studied chain.

Further theoretical studies focused on the retardation effects in the dipole-dipole interaction for the point dipole model. It was shown [46, 47] that the retardation in the interaction causes a nonmonotonic behavior in the dispersion relation of the transverse modes (lower panel in Figure 1.10), as opposed to the longitudinal one (upper panel in Figure 1.10). The authors of Ref. [46] argued that this nonmonotonic behavior present for the transverse modes arises from the phase matching between plasmon dispersion and the free photon of the same frequency. Moreover, the influence of the interaction onto radiation losses was shown [46, 47] to lead to the mode dependent radiation damping presented in the lower panel of Figure 1.9. The mode-dependence of the radiation damping leads to the separation of the modes into bright modes ($k_{\text{mode}} \leq \omega/c$) influenced by radiation damping and into dark modes ($k_{\text{mode}} \geq \omega/c$) immune to radiation losses. Here k_{mode} denotes the momentum of the plasmonic mode.

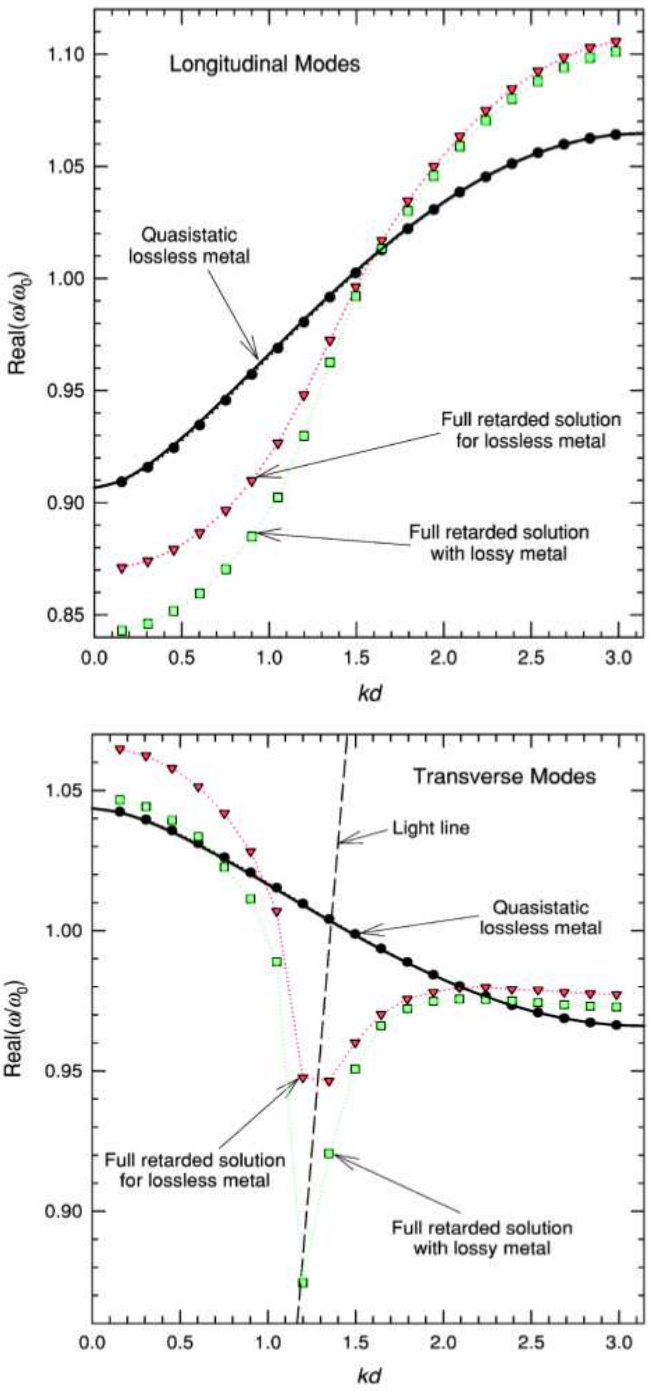

Figure 1.10: Dispersion curves for the longitudinal (upper panel) and transverse (lower panel) modes. Solid black lines represent the quasistatic limit of an infinite chain. Points represent results for a finite chain with $\mathcal{N} = 20$: Black circles are for the quasistatic approximation, green squares for the full retarded solution with a lossy metal, red triangles for the full retarded solution and an ideal metal. The dashed line in the left panel is the light line, $\omega = ck$. Reproduced from Ref. [46].

Furthermore, Weber *et al.* [46] investigated the propagation of the plasmon along the chain under a continuous pumping. For this study they considered chains of Ag nanoparticles with radii 25 nm and center-to-center distance 75 nm, that is the same parameters as previously studied in Refs. [37, 40]. It was shown [46] that initially the modes corresponding to both polarizations decay in a non-exponential fashion, with the transverse mode decaying faster. Nonetheless, for longer distances the signal decay progressively became exponential-like. Such a conclusion turned out to be in contradiction with earlier reports suggesting that the decay of the transverse modes is weaker than the decay of the longitudinal mode for long distances. Moreover, the resulting decay length for the longitudinal mode (700 nm) was comparable to the one obtained by Quinten *et al.* in Ref. [37] (900 nm). The difference in the propagation of the transverse modes between the results of Weber *et al.* and Quinten *et al.* was argued by the former group to be due to the inclusion of retardation effects.

Later studies of chains with fully retarded dipole-dipole interaction investigated the influence of disorder onto the system properties. Merkel *et al.* [53] studied both, ordered and disordered chains, using a similar approach as Weber *et al.* [46], confirming the previous findings (dispersion and damping). Ref. [53] also reported a double exponential decay for ordered chains, in which the transverse modes propagate for longer distances. In addition, two types of plasmons were discussed: ordinary, subradiative modes which localize in the presence of any disorder strength, and extraordinary, radiative modes which weakly depend on the disorder.

More recent developments focused on quantum effects for the plasmon propagation in nanoparticle chains. Lee *et al.* [57] introduced a quantum model for a nanoparticle chain connected to the plasmon reservoirs in order to study the possibility of a coherent qubit transfer. The role of the qubit is played by the plasmonic wave packet. It was shown that, even under realistic conditions, coherent transfer is possible on short distances, thus opening the possibility for metallic nanoparticle chains to act on short distances as on-chip nanophotonic quantum comunication devices.

Other work investigating quantum properties of metallic nanoparticle chains was done by Pino *et al.* [61]. Using a simple quantum model based on nearest neighbor interaction with constant damping and using the master equation in Lindblad form, the authors obtained the equations of motion for the plasmons. Using their model, the authors presented a prescription how to calculate propagation length and entanglement of the plasmonic excitation.

The theoretical investigations of nanoparticle chains, summarized in this secion, spanned many fronts covering important properties (dispersion, damping and propagation). In Chapter 4 of this thesis we will

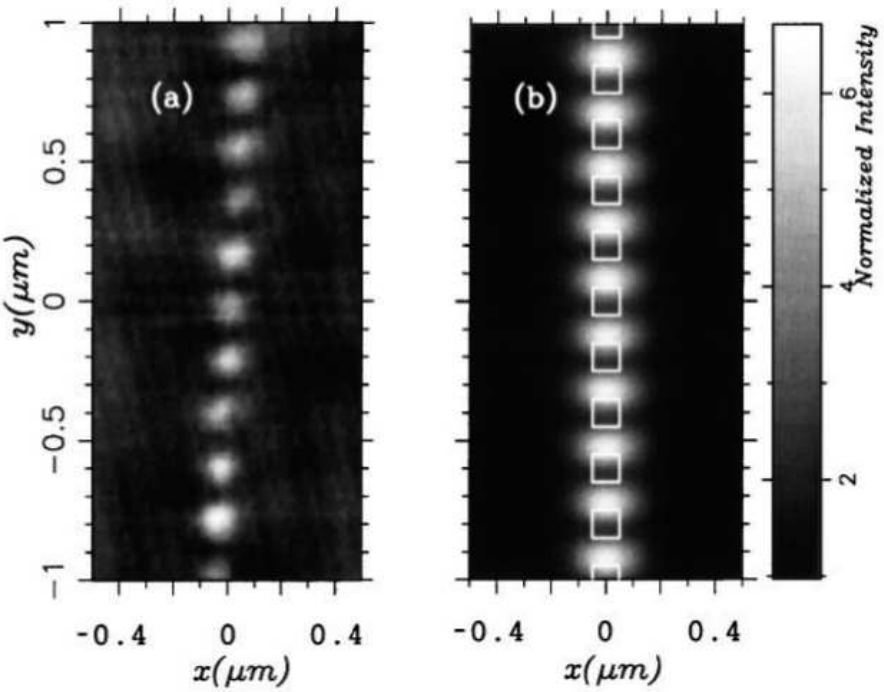

Figure 1.11: (a) Constant height PSTM image recorded above the chain of Au nanoparticles (individual size $100 \times 100 \times 40\text{nm}^3$) separated from each other by a distance of 100nm and deposited on an ITO substrate. A comparison with a numerical simulation (b) shows that the bright spots are not on top of the Au particles (the surface projections of the particles correspond to the white squares). The intensity scale of the experimental data (a) is normalized to the one of the numerical calculation. Reproduced from Ref. [38].

present a model for ordered homogeneous metallic nanoparticle chains incorporating all the important properties discussed earlier. Moreover, using this model we show the origin of the exponential decay in the plasmon propagation reported earlier [37, 40, 46].

1.4 Experimental treatment of nanoparticle chains

The first experimental observation of the near field associated with collective plasmons in ordered nanoparticle chains was reported by Krenn *et al.* [38]. This experiment used the electron beam lithography technique to fabricate a chain of 10000 Au nanoparticles on an indium-tin-oxide (ITO) substrate (see Figure 1.11). The nanoparticle shape was akin to oblate spheroids with dimensions $100 \times 100 \times 40$ nm^3 and interparticle separation of 100 nm. In order to measure the near field

around the metallic nanoparticles the authors of Ref. [38] used a photon scanning tunneling microscope (PSTM). PSTM works similarly to the standard STM, where the tip measures tunneling of electrons. Instead of electrons, a PSTM measures photons which undergo total internal reflection in the sample when the tip of the PSTM (which has an optical fiber) is nearby. In order to confirm that the PTSM truly measures the near field, Krenn *et al.* compared the measurements to their numerical simulations for both single nanoparticle as well as the full chain. The numerical scheme which they used was Green's dyadic technique [87] with a reference system of the ITO substrate and the nanoparticles treated as a perturbation. In the computations the authors assumed that the incoming electric field was TM (transverse magnetic) polarized and incident through the substrate under the condition of total internal reflection. The result of their investigations was the proof that the PSTM truly measures the optical near field intensity close to the metallic objects. They also reported the observation of the squeezed optical near field coming from the coupled plasmons in the chain. The main comparison between numerical simulation and experimental measurements is presented in Figure 1.11, where we observe both experimentally [panel (a)] and numerically [panel (b)] obtained intensities. The comparison gives encouragement to the statement, that PSTM measures near-field. Moreover, in the figure we see that regions with high intensities are present in between the nanoparticles.

Contrary to the near field measurements presented by Krenn and coworkers, the experiments by Maier *et al.* [41, 42] used far field polarization spectroscopy to study the influence of the near field coupling between plasmons in Au nanoparticle chains. Using electron beam lithography, they fabricated the Au nanoparticle chains with particle diameters of 50 nm and various interparticle separations as well as various chain length. From the far field measurements the authors succeeded to obtain energies of both, the longitudinal and the transverse modes, depending on the polarization of the illuminating light. Typical far field extinction spectra of single nanoparticles and a nanoparticle chain is presented in Figure 1.12. In the figure we observe a comparison between extinction spectra of an isolated Ag nanorod and a linear chain of Ag nanorods. We see that in addition to the blue-shift of the resonance peak its linewidth and extinction value are increased .

In Ref. [42] these authors investigated a dependence of the central peak position (the energy of the lowest momentum mode) obtained from the far field measurements onto the interparticle separation. They fabricated three chains of 80 closely spaced Au nanoparticles with diameters of 50 nm and center-to-center separations of 75 nm, 100 nm and 125 nm. This corresponds to a radius over interparticle distance ratio a/d of 1/3, 1/4 and 1/5, respectively. The measurements of the shift of the peaks for both longitudinal and transverse modes confirmed

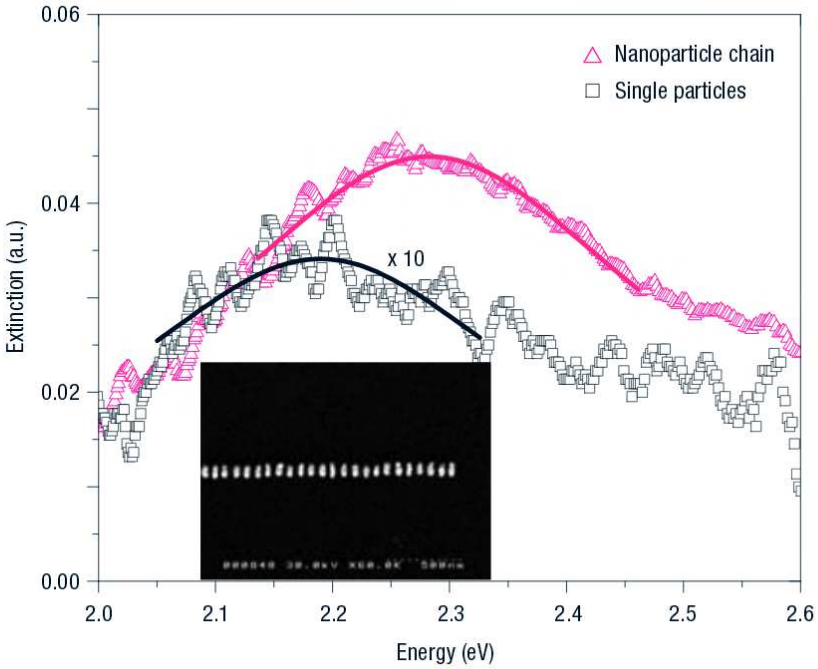

Figure 1.12: Far field extinction spectrum of a plasmon waveguide consisting of Ag nanorods with a 3 : 1 aspect ratio and a surface to surface spacing of 50 nm between adjacent particles showing that the plasmon resonance peak shifts to higher energies (red triangle and Lorentz fit) compared with the extinction spectrum of isolated, non interacting particles (black squares and Lorentz fit). The exciting light is polarized along the long axis of the nanorods, perpendicular to the chain axis. The inset shows a scanning electron micrograph of the plasmon waveguide layout under study. Reproduced from Ref. [43].

their predictions from the point dipole model [40], pointing towards the relevance of near-field coupling between the particles. In another article Maier *et al.* [41] studied different chain lengths of Au nanoparticles and compared the obtained peak energies to those obtained by the FDTD calculations. Furthermore, based on their point dipole model [40] they estimated the attenuation of the plasmon propagation for the longitudinal mode, which turns out to be much larger than the ones predicted for Ag nanoparticle chains [37, 40, 46].

In their work from 2003 [43] Maier *et al.* shifted from the spherical Au nanoparticle chains to Ag nanorod chains (see inset in Figure 1.12). Using electron beam lithography the authors fabricated a chain of Ag nanorods with dimensions $90 \times 30 \times 30$ nm^3 and surface-to-surface spacing of 50 nm. The goal of the experiment was to probe the energy transport along the chain via plasmon propagation. In order to obtain

a local excitation the authors used the tip of the illumination mode near field optical microscope. Energy transport was probed by placing fluorescent molecules in the vicinity of the nanoparticle chain away from the illuminated particle. The authors of Ref. [43] managed to observe transport of energy along the chain and estimated the losses along the chain to be 6dB per 195 ± 28nm.

More recent experimental developments focused on the spatial imaging of the plasmon modes. Appuzo *et al.* [60] mapped the propagating plasmon using a scanning near field optical microscope in elliptical Au nanocylinders. The elliptic parameters were measured to be $D_1 = 211$ nm, $D_2 = 66$ nm with the thickness of the nanocylinder of 30 nm. The center-to-center distance was 150 nm. Successfully measured near field of the propagating lowest momentum plasmon was compared to the numerical simulations. Other experiments performed by Barrow *et al.* [62] used the EELS technique to investigate the dark modes of a short nanoparticle chains (form 2 to 5).

Most of the experimental work on coupled nanoparticle systems did not probe the propagation of the excitation, with an exception of Refs. [43, 58] which proved the existence of plasmon propagation. Rather than propagation the experiments proved the existence of the collective behavior of the plasmons, which is at the origin of the propagation. The main issue, concerning propagation, that needs to be addressed relates to the influence of the intrinsic losses onto the limitation of the propagation [11]. Our investigation of nanoparticle chains in Chapter 4 will focus on this exact issue.

1.5 Outlook of the thesis

In this thesis we propose a general open quantum system approach to interacting plasmons in one dimensional assemblies of metallic nanoparticles. The proposed model will give us tools to obtain a deeper understanding on how the interparticle interaction influences the dispersion relation and damping mechanisms in the system. It will also allow us to investigate the propagation of excitations through nanoparticle chains. The thesis is organized as follows:

In Chapter 2 we review the theoretical framework to calculate the properties of the plasmon inside an isolated spherical metallic nanoparticle. We start from the microscopic Hamiltonian for electrons and show how one obtains through separation of the coordinates (center-of-mass and relative) a coupling between plasmons and electronic and photonic baths. Further, using a mean-field approximation and semi-classical expansions we show how one can evaluate damping rates for the plasmons.

In Chapter 3 we turn to the investigation of nanoparticle dimers, which is a building block of more complex nanoparticle-based metas-

tructures. Using the theoretical framework presented in Chapter 2 we extend the model to the interacting plasmons case. Using Bogoliubov diagonalization we obtain coupled plasmonic modes. Using techniques from Chapter 2 we obtain both Landau and radiation damping of the coupled plasmonic modes, which we then analyze for various sizes of the system.

In Chapter 4 we focus on nanoparticle chains. Extending further the model obtained in Chapter 3, we investigate coupled plasmonic modes of the chain. Using a master equation approach, which we derive under Markovian hypothesis and in the weak-coupling regime, we evaluate dissipation rates (Landau and radiation) for the collective plasmons. Further, with the use of master equations we investigate the plasmon propagation along the chain under continuous and pulsed excitations of the plasmon. We find that the plasmonic excitation decays in two regimes. For short distance from the excitation position, the decay is exponential, and algebraic for longer distances. We show that the exponential decay is of purely non-radiative origin, and use this observation to derive an analytical expression for the propagation length in the case of continuous excitation.

Finally we conclude the thesis in Chapter 5 and give some perspectives that our work offers.

Chapter 2

Lifetime of the localized surface plamon in isolated single spherical metallic nanoparticles

The localized surface plasmon in an isolated metallic spherical nanoparticle undergoes two types of damping: radiative damping due to the radiation of the accelerated electrons into the far field and non-radiative damping, which is composed of bulk Ohmic losses and size-dependent Landau damping. In this chapter we review the theoretical framework to investigate the problem of localized surface plasmon lifetimes in an isolated spherical metallic nanoparticle [1, 14, 17, 19, 24, 25, 91].

Section 2.1 introduces microscopic Hamiltonian and with the separation into the center-of-mass (plasmon) and relative coordinates (electrons), the origin of the coupling between plasmon and electrons as well as the plasmon and photons is shown. The mean-field approximation introduced in Section 2.2 allows evaluation of the Landau damping using semiclassical expansion in Section 2.3 [14, 17, 19, 24, 25], and the radiation damping in Section 2.4 [91, 92].

2.1 Microscopic Hamiltonian

Let us consider a single isolated spherical metallic nanoparticle with radius a containing N_e electrons. Writing the microscopic Hamiltonian for the electrons within the *jellium* approximation [88], i.e. with the positive ions as a uniformly charged sphere of radius a, and in the

Coulomb gauge (i.e. $\nabla \cdot \mathbf{A}(\mathbf{r}) = 0$), one has

$$H = \sum_{i=1}^{N_\mathrm{e}} \left\{ \frac{[\mathbf{p}_i + e\mathbf{A}(\mathbf{r}_i)]^2}{2m_\mathrm{e}} + U(r_i) \right\} + \frac{e^2}{2} \sum_{\substack{i,j=1 \\ i \neq j}}^{N_\mathrm{e}} \frac{1}{|\mathbf{r}_i - \mathbf{r}_j|} + \frac{1}{8\pi} \int \mathrm{d}^3 r \, (E^{\perp 2}(\mathbf{r}) + c^2 B^2(\mathbf{r})), \tag{2.1}$$

where e and m_e are the electron charge and mass, respectively, and c is the speed of light. In the above equation $\mathbf{r}_i$ is the position of the i-th electron and $\mathbf{p}_i$ its momentum, $\mathbf{A}(\mathbf{r}_i)$ is the vector potential at position $\mathbf{r}_i$ with associated transverse electric and magnetic fields, $E^\perp(\mathbf{r}) = -(1/c)\partial \mathbf{A}(\mathbf{r})/\partial t$ and $B(\mathbf{r}) = \nabla \times \mathbf{A}(\mathbf{r})$, respectively. While, the longitudinal part of the electric field reads $\mathbf{E}^\parallel = -\nabla\phi(\mathbf{r})$, with $\phi(\mathbf{r})$ being responsible for the electron-electron interaction (c.f. second term on the right-hand-side of Eq. (2.1)). Note, that the jellium model is an approximation simple enough to be applied to spherical nanoparticles and, at the same time, accurate enough to catch the essential physics of the considered system [88].

The single-electron potential in Eq. (2.1) coming from the positively charged sphere

$$U(\mathbf{r}) = \frac{N_\mathrm{e} e^2}{2a^3}(r^2 - 3a^2)\Theta(a - r) - \frac{N_\mathrm{e} e^2}{r}\Theta(r - a), \tag{2.2}$$

is harmonic with the Mie frequency $\omega_0 = \sqrt{N_\mathrm{e} e^2/m_\mathrm{e} a^3}$ inside the nanoparticle and Coulomb-like outside (see Figure 2.1). In Eq. (2.2) $\Theta(x)$ is the Heaviside step function.

Since in most of the nanoparticles experimentally under consideration the number of electron is too large to be able to diagonalize the Hamiltonian (2.1) exactly, there exists a particularly useful decomposition of it [21,93] by introducing the center-of-mass coordinate (corresponding to the localized surface plasmon) and the relative coordinates. The electronic center-of-mass coordinate writes $\mathbf{R} = \sum_{i=1}^{N_\mathrm{e}} \mathbf{r}_i/N_\mathrm{e}$ and its conjugate momentum $\mathbf{P} = \sum_{i=1}^{N_\mathrm{e}} \mathbf{p}_i$. Noting that the photons responsible for the plasmon decay are the optical ones (ω_0 is in the optical range), one may rewrite the Hamiltonian (2.1) with $\mathbf{A}(\mathbf{r}_i) \simeq \mathbf{A}(0)$, as

$$H = \frac{\mathbf{P}^2}{2N_\mathrm{e} m_\mathrm{e}} + H_\mathrm{eh} + \sum_{i=1}^{N_\mathrm{e}} [U(|\mathbf{R} - \mathbf{r}'_i|) - U(r'_i)] + H_\mathrm{ph} + H_\mathrm{pl-ph}, \tag{2.3}$$

where the relative coordinate Hamiltonian reads

$$H_\mathrm{eh} = \sum_{i=1}^{N_\mathrm{e}} \left[\frac{\mathbf{p}'^{\,2}_i}{2m_\mathrm{e}} + U(r'_i) \right] + \frac{e^2}{2} \sum_{\substack{i,j=1 \\ i \neq j}}^{N_\mathrm{e}} \frac{1}{|\mathbf{r}'_i - \mathbf{r}'_j|}, \tag{2.4}$$

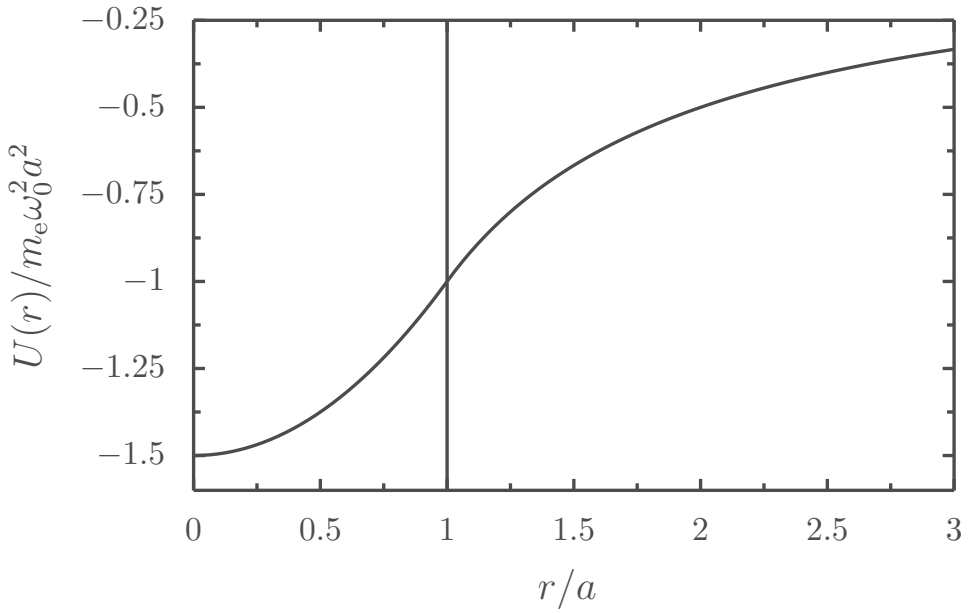

Figure 2.1: Single electron confinement potential produced by a homogeneously charged jellium sphere.

with $\mathbf{r}'_i = \mathbf{r}_i - \mathbf{R}$ and $\mathbf{p}'_i = \mathbf{p}_i - \mathbf{P}/N_\mathrm{e}$. In Eq. (2.3) the Hamiltonian $H_\mathrm{ph} = \frac{1}{8\pi}\int \mathrm{d}^3r\,(E^{\perp 2}(\mathbf{r}) + c^2B^2(\mathbf{r}))$ describes the free photon energy (c.f. last term on the right-hand-side of Eq. (2.1)). The last term on the right-hand-side of Eq. (2.3) describes the plasmon-photon coupling $H_\mathrm{pl-ph} = \frac{e}{m_\mathrm{e}}\mathbf{P}\cdot\mathbf{A}(0)$.

Assuming that the center-of-mass displacement $\mathbf{R}$ is much smaller than the radius of the nanoparticle, one can expand the third term in the right-hand-side of Eq. (2.3) to second order in $|\mathbf{R}|/a$ to get

$$U(|\mathbf{R}-\mathbf{r}'|) - U(r') \simeq \mathbf{R}\cdot\nabla U(r') + \frac{1}{2}(\mathbf{R}\cdot\nabla)^2 U(r'), \tag{2.5}$$

where the derivatives are taken at $\mathbf{r}' = \mathbf{r}$ (*i.e.* $\mathbf{R} = 0$). Using the expression of the single electron confinement (2.2) one has

$$\mathbf{R}\cdot\nabla U(r') = m_\mathrm{e}\omega_0^2\mathbf{R}\cdot\left[\mathbf{r}'\Theta(a-r') - \frac{\mathbf{r}'a^3}{r^3}\Theta(r'-a)\right], \tag{2.6}$$

$$(\mathbf{R}\cdot\nabla)^2 U(r') \simeq \mathbf{R}^2\frac{N_\mathrm{e}e^2}{a^3}\Theta(a-r'). \tag{2.7}$$

Inserting the above equations into the Hamiltonian (2.3) one gets

$$H = H_\mathrm{pl} + H_\mathrm{eh} + H_\mathrm{pl-eh} + H_\mathrm{ph} + H_\mathrm{pl-ph}, \tag{2.8}$$

where the center-of-mass (plasmonic) part reads

$$H_\mathrm{pl} = \frac{\mathbf{P}^2}{2N_\mathrm{e}m_\mathrm{e}} + \frac{1}{2}N_\mathrm{e}m_\mathrm{e}\tilde{\omega}_0\mathbf{R}^2. \tag{2.9}$$

The resonance frequency $\tilde{\omega}_0$ is shifted with respect to the the Mie frequency due to the spill-out effect [1, 18, 88]

$$\tilde{\omega}_0 = \omega_0 \sqrt{1 - \frac{N_{\mathrm{e,out}}}{N_{\mathrm{e}}}}. \tag{2.10}$$

Here $N_{\mathrm{e,out}}$ is the number of electrons that are outside of the nanoparticle , i.e. $r_i > a$.

The third term in the right-hand-side of Eq. (2.8) represents the coupling between the center-of-mass (plasmon) and the relative coordinates (electrons)

$$H_{\mathrm{pl-eh}} = \sum_{i=1}^{N_{\mathrm{e}}} \mathbf{R} \cdot \nabla U(\mathbf{r}_i). \tag{2.11}$$

Such a coupling stems from the breakdown of Kohn's theorem [89], which states that for a purely harmonic confinement the center-of-mass and the relative coordinates are decoupled. The breakdown of the theorem comes from the Coulombic part of the single electron confinement (2.2), which originates from the positive ionic background. If the confinement were a purely harmonic one, then Eq. (2.11) would identically be zero.

The last term on the right-hand-side of Eq. (2.8) corresponds to the plasmon-photon coupling

$$H_{\mathrm{pl-ph}} = \frac{e}{m_{\mathrm{e}}} \mathbf{P} \cdot \mathbf{A}(0). \tag{2.12}$$

The full Hamiltonian (2.8) is characteristic of an open quantum system [19, 22, 24–27, 30, 91]. That is, a small quantum system coupled to an environment that induces dissipation. In the case of the Hamiltonian (2.8) the coupling of plasmons (2.9) to the electronic (2.11) and photonic (2.12) baths, leads to a dissipation of the former. This dissipation is govern by the Landau and radiation damping rates, respectively.

2.2 Mean-field approximation and second quantization

Although the separation into the relative and center-of-mass coordinates is very useful, due to the large number of electrons it is still difficult to solve the problem exactly. This is why one may introduce a mean-field approximation to the relative coordinates [19, 22, 24, 25], and moreover rewrite the center-of-mass Hamiltonian (2.9) in its second quantized form. It will be especially helpful in determining the Landau damping of the plasmon which is a pure quantum effect. Since

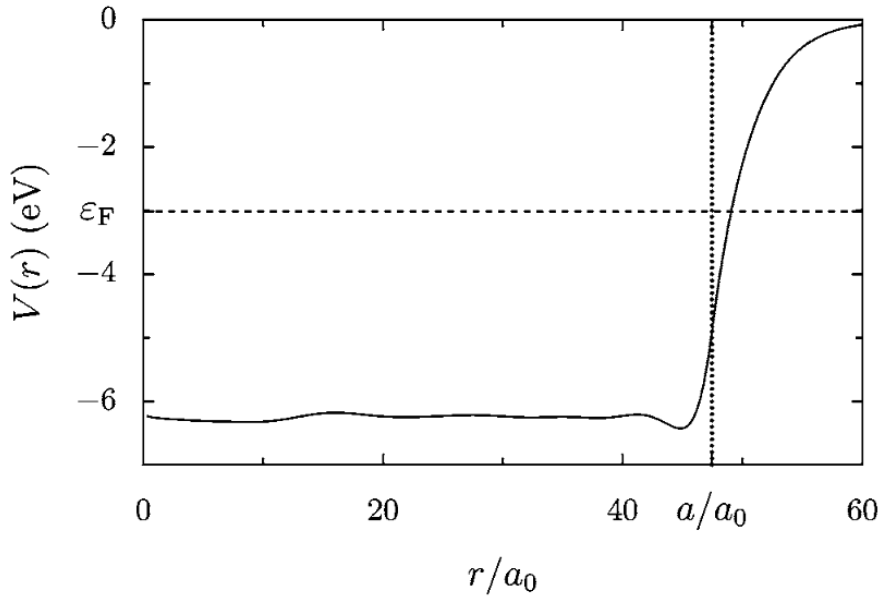

Figure 2.2: LDA self-consistent potential V as a function of the radial coordinate r for a sodium nanoparticle containing $N_e = 1760$ valence electrons. The radius a is indicated by the vertical dotted line. The Fermi level is marked by the dashed line. a_0 is the Bohr radius. Reproduced from Ref. [25].

the radiation damping is a classical phenomena, one may use classical electromagnetism to evaluate it [70]. Obviously the same result is obtainable in a quantum manner [91], since classical phenomena of radiation corresponds to spontaneous emission of photons.

Introducing the annihilation and creation operators for the localized surface plasmon in the $\hat{\sigma} = \hat{x}, \hat{y}, \hat{z}$ direction

$$b^{\sigma} = \sqrt{\frac{N_e m_e \tilde{\omega}_0}{2\hbar}} \hat{\sigma} \cdot \mathbf{R} + \frac{\mathrm{i}}{\sqrt{2N_e m_e \hbar \tilde{\omega}_0}} \hat{\sigma} \cdot \mathbf{P}, \tag{2.13}$$

$$b^{\sigma\dagger} = \sqrt{\frac{N_e m_e \tilde{\omega}_0}{2\hbar}} \hat{\sigma} \cdot \mathbf{R} - \frac{\mathrm{i}}{\sqrt{2N_e m_e \hbar \tilde{\omega}_0}} \hat{\sigma} \cdot \mathbf{P}, \tag{2.14}$$

one writes the center-of-mass Hamiltonian (2.9) as

$$H_{\mathrm{cm}} = \sum_{\sigma=x,y,z} \hbar \tilde{\omega}_0 b^{\sigma\dagger} b^{\sigma}. \tag{2.15}$$

Since the relative-coordinate Hamiltonian (2.4) contains the electron-electron interactions one replaces it by its mean-field counterpart [19, 22, 24–26]. In second quantization one can express the relative Hamiltonian (2.4) as

$$H_{\mathrm{eh}} = \sum_{\alpha} \varepsilon_{\alpha} c_{\alpha}^{\dagger} c_{\alpha}, \tag{2.16}$$

where the operator $c_\alpha^\dagger$ (c_α) creates (annihilates) an electron in the state $|\alpha\rangle$ with the energy ε_α in the self-consistent mean-field potential V. From local density approximation (LDA) calculations [25] the form of the potential V can be approximated by a spherical square well of height V_0 (see Figure 2.2). Noting that the typical plasmon energy is lower than the work function of the metal of which the nanoparticle is composed of (we see that the excited electron will not ionize). Therefore, in what follows we take the limit of the height of the potential to infinity ($V_0 \to \infty$).

Rewriting the coupling Hamiltonian (2.11) in second quantized form within the mean-field approximation, one has

$$H_{\rm c} = \sum_{\sigma=x,y,z} \sum_{\alpha\beta} \Lambda(b^\sigma + b^{\sigma\dagger})\hat{\sigma} \cdot \mathbf{d}_{\alpha\beta} c_\alpha^\dagger c_\beta, \tag{2.17}$$

where

$$\mathbf{d}_{\alpha\beta} = \langle\alpha|\mathbf{r}\Theta(a-r) + \frac{\mathbf{r}a^3}{r^3}\Theta(r-a)|\beta\rangle. \tag{2.18}$$

Within the approximation of an infinite height for the self-consistent potential, the above expression becomes a dipole matrix elements reading

$$\mathbf{d}_{\alpha\beta} = \mathcal{R}(\varepsilon_\alpha, \varepsilon_\beta)\left(\sum_{s=\pm} \mathcal{A}_{\ell_\alpha \ell_\beta s}^{m_\alpha m_\beta} \frac{\hat{x} - {\rm i}s\hat{y}}{\sqrt{2}} + \mathcal{A}_{\ell_\alpha \ell_\beta 0}^{m_\alpha m_\beta} \hat{z}\right), \tag{2.19}$$

with the radial part given by [17]

$$\mathcal{R}(\varepsilon_\alpha, \varepsilon_\beta) = \frac{2\hbar^2}{m_{\rm e} a} \frac{\sqrt{\varepsilon_\alpha \varepsilon_\beta}}{(\varepsilon_\alpha - \varepsilon_\beta)^2}. \tag{2.20}$$

The angular part of Eq. (2.19) is expressed in terms of Wigner-3j symbols as [30]

$$\begin{aligned} \mathcal{A}_{\ell_\alpha \ell_\beta s}^{m_\alpha m_\beta} &= (-1)^{m_\alpha + s}\sqrt{(2\ell_\alpha + 1)(2\ell_\beta + 1)} \\ &\times \begin{pmatrix} \ell_\alpha & \ell_\beta & 1 \\ 0 & 0 & 0 \end{pmatrix} \begin{pmatrix} \ell_\alpha & \ell_\beta & 1 \\ -m_\alpha & m_\beta & s \end{pmatrix}. \end{aligned} \tag{2.21}$$

Notice that the expression above encapsulates the angular momentum selection rules $\ell_\alpha = \ell_\beta \pm 1$, $m_\alpha = m_\beta$ (for $s = 0$) and $m_\alpha = m_\beta \mp 1$ (for $s = \pm 1$).

In Eq. (2.17) the constant

$$\Lambda = \sqrt{\frac{\hbar m_{\rm e} \omega_0^3}{2N_{\rm e}}}, \tag{2.22}$$

neglects the spill-out effect. The reason behind this approximation is that the spill out effect scales with $1/k_{\rm F}a$ [25] (where $k_{\rm F}$ is Fermi's

wavevector) and since Landau damping also scales with $1/k_{\mathrm{F}}a$ [14, 17, 19, 22, 24, 25], keeping the spill-out effect would amount to higher order corrections in $k_{\mathrm{F}}a \gg 1$. Thus, one restricts oneself only to the first order in $1/k_{\mathrm{F}}a$ by neglecting the spill-out effect in the coupling (2.17).

The free photon Hamiltonian (c.f. forth term on right-hand-side of Eq. (2.3)) in second quantization reads [91]

$$H_{\mathrm{ph}} = \sum_{\mathbf{k},\hat{\lambda}_{\mathbf{k}}} \hbar\omega_{\mathbf{k}} a^{\dagger}_{\mathbf{k}\hat{\lambda}_{\mathbf{k}}} a_{\mathbf{k}\hat{\lambda}_{\mathbf{k}}}, \tag{2.23}$$

where $a_{\mathbf{k}\hat{\lambda}_{\mathbf{k}}}$ ($a^{\dagger}_{\mathbf{k}\hat{\lambda}_{\mathbf{k}}}$) annihilates (creates) a photon with momentum $\mathbf{k}$, transverse polarization $\hat{\lambda}_{\mathbf{k}}$ ($\hat{\lambda}_{\mathbf{k}} \cdot \mathbf{k} = 0$) and dispersion $\omega_{\mathbf{k}} = c|\mathbf{k}|$.

The vector potential in second quantization reads [91]

$$\mathbf{A}(\mathbf{r}) = \sum_{\mathbf{k},\hat{\lambda}_{\mathbf{k}}} \sqrt{\frac{2\pi\hbar}{\mathcal{V}\omega_{\mathbf{k}}}} \left(\hat{\lambda}_{\mathbf{k}} a_{\mathbf{k},\hat{\lambda}_{\mathbf{k}}} e^{\mathrm{i}\mathbf{k}\cdot\mathbf{r}} + \hat{\lambda}^{*}_{\mathbf{k}} a^{\dagger}_{\mathbf{k},\hat{\lambda}_{\mathbf{k}}} e^{-\mathrm{i}\mathbf{k}\cdot\mathbf{r}} \right) \tag{2.24}$$

leads to the plasmon-photon coupling (c.f. last term on right-hand-side of Eq. (2.3)) in the form

$$H_{\text{pl-ph}} = \mathrm{i}\hbar \sum_{\sigma=x,y,z} \sum_{\mathbf{k},\hat{\lambda}_{\mathbf{k}}} \sqrt{\frac{\pi\omega_0^3 a^3}{\mathcal{V}\omega_{\mathbf{k}}}} \left(b^{\sigma\dagger} - b^{\sigma} \right) \left(\hat{\sigma} \cdot \hat{\lambda}_{\mathbf{k}} a_{\mathbf{k}\hat{\lambda}_{\mathbf{k}}} + \hat{\sigma} \cdot \hat{\lambda}^{*}_{\mathbf{k}} a^{\dagger}_{\mathbf{k}\hat{\lambda}_{\mathbf{k}}} \right). \tag{2.25}$$

The above coupling leads to a process in which plasmon is annihilated (created) by creation (annihilation) of the photon. We will use this coupling to determine the radiative losses for the plasmons.

2.3 Landau damping

One may now evaluate the Landau damping linewidth of the plasmon first excited state. Assuming a weak coupling $H_{\mathrm{pl-eh}}$, the inverse lifetime of the plasmon can be approximated by the Fermi golden rule

$$\gamma^{\sigma,\mathrm{L}} = \frac{2\pi}{\hbar} \sum_{eh} |\langle 0^{\sigma}, eh | H_{\mathrm{pl-eh}} | 1^{\sigma}, 0 \rangle|^2 \delta(\hbar\omega_0 - E_e + E_h), \tag{2.26}$$

where the sum goes over all the possible electron $|e\rangle$ and hole $|h\rangle$ states in the self-consistent potential V, with $|0\rangle$ representing the ground state of the electron bath. The state $|1^{\sigma}\rangle$ represents a plasmon in the first excited state with a polarization $\hat{\sigma}$. In Eq. (2.26) $\delta(x)$ is Dirac's delta function.

Inserting Eq. (2.17) into Eq. (2.26), the Landau damping reads as

$$\gamma^{\sigma,\mathrm{L}} = \Sigma^{\sigma}(\omega_0), \tag{2.27}$$

with

$$\Sigma^{\sigma}(\omega) = \frac{2\pi}{\hbar^2}\Lambda^2 \sum_{eh} |\langle e| \sigma |h\rangle|^2 \, \delta(\hbar\omega - \varepsilon_e + \varepsilon_h). \tag{2.28}$$

In Eq. (2.28) one can evaluate the summation over electron e and hole h states by introducing the density of states $\varrho_\ell(E)$ with fixed angular momentum ℓ at energy E, which gives

$$\Sigma^{\sigma}(\omega) = 2\frac{2\pi}{\hbar} \sum_{\ell_e,\ell_h} \sum_{m_e,m_h} \int \mathrm{d}\varepsilon_e \mathrm{d}\varepsilon_h \varrho_{\ell_e}(\varepsilon_e)\varrho_{\ell_h}(\varepsilon_h) |\Lambda\hat{\sigma}\cdot\mathbf{d}_{eh}|^2 \delta(\hbar\omega - \varepsilon_e + \varepsilon_h), \tag{2.29}$$

where the factor of 2 comes from the spin degree of freedom. Inserting the dipole matrix elements (2.19) into Eq. (2.29) and making the use of the angular momentum selection rules one gets

$$\begin{aligned}\Sigma^{\sigma}(\omega) =& \frac{16\pi}{3\hbar m_{\mathrm{e}}^2\omega^4}\frac{\Lambda^2}{a^2} \int\limits_{\max\{E_{\mathrm{F}},\hbar\omega\}}^{E_{\mathrm{F}}+\hbar\omega} \mathrm{d}\varepsilon \\ & \times \varepsilon(\varepsilon-\hbar\omega) \sum_{\ell} \varrho_\ell(\varepsilon) \left[(\ell+1)\varrho_{\ell+1}(\varepsilon-\hbar\omega) + \ell\varrho_{\ell-1}(\varepsilon-\hbar\omega)\right],\end{aligned} \tag{2.30}$$

where E_{F} is the Fermi energy of the nanoparticle. Note that the function $\Sigma^{\sigma}(\omega)$ is independent of the direction σ, due to the spherical symmetry of the system. To recover Eq. (2.30) one uses the equalities

$$\sum_{m=-\ell}^{\ell} \left(\mathcal{A}_{\ell\ell+1s}^{mm+s}\right)^2 = \frac{\ell+1}{3} \tag{2.31}$$

and

$$\sum_{m=-\ell}^{\ell} \left(\mathcal{A}_{\ell\ell-1s}^{mm+s}\right)^2 = \frac{\ell}{3}, \tag{2.32}$$

for $s = 0, \pm 1$.

The density of states $\varrho_\ell(E)$ with fixed angular momentum ℓ can be obtained using semiclassical methods [95, 96]. The leading order of the semiclassical form of the density of states $\varrho_\ell(E)$ [24] reads

$$\varrho_\ell(\varepsilon) \simeq \frac{\sqrt{2m_{\mathrm{e}}a^2\varepsilon/\hbar^2 - (\ell+1/2)^2}}{2\pi\varepsilon}. \tag{2.33}$$

Inserting the above equation into the expression for the function $\Sigma^{\sigma}(\omega)$ (2.30) and changing the summation over the angular momentum ℓ to an integral, in the limit $\ell \gg 1$ one gets

$$\begin{aligned}\Sigma^{\sigma}(\omega) =& \frac{8}{3\hbar m_{\mathrm{e}}^2\omega^4}\frac{\Lambda^2}{a^2} \int\limits_{\max\{E_{\mathrm{F}},\hbar\omega\}}^{E_{\mathrm{F}}+\hbar\omega} \mathrm{d}\varepsilon \int\limits_{0}^{2m_{\mathrm{e}}a^2(\varepsilon-\hbar\omega)/\hbar^2} \mathrm{d}\ell \\ & \times \ell\sqrt{\varepsilon(\varepsilon-\hbar\omega)}\sqrt{2m_{\mathrm{e}}a^2\varepsilon/\hbar^2 - \ell^2}\sqrt{2m_{\mathrm{e}}a^2(\varepsilon-\hbar\omega)/\hbar^2 - \ell^2}.\end{aligned} \tag{2.34}$$

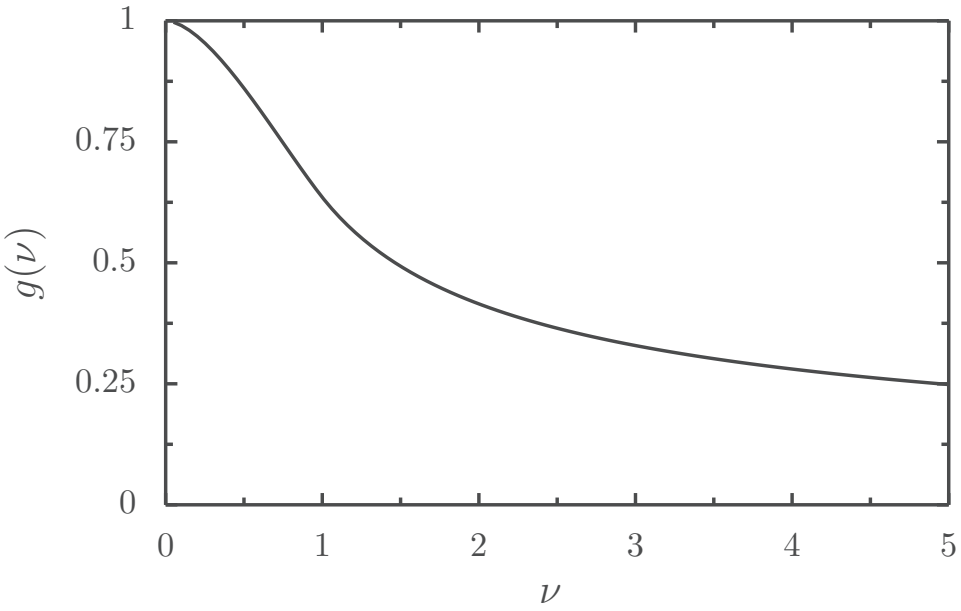

Figure 2.3: Function $g(\nu)$ defined in Eq. (2.37).

Evaluating the above expression one finds the final form for the function

$$\Sigma^{\sigma}(\omega) = \left(\frac{\omega_0}{\omega}\right)^3 \frac{3v_{\mathrm{F}}}{4a} g\left(\frac{\hbar\omega}{E_{\mathrm{F}}}\right), \tag{2.35}$$

where the function $g(\nu)$ can be represented as an integral through

$$g(\nu) = \frac{2}{\nu} \int\limits_{\max\{1,\nu\}}^{1+\nu} \mathrm{d}x \int\limits_{0}^{x-\nu} \mathrm{d}y \sqrt{(x-y)(x-y-\nu)}, \tag{2.36}$$

or explicitly written as [17, 24, 25, 30]

$$\begin{aligned} g(\nu) =& \frac{1}{3\nu}\left[(1+\nu)^{3/2} - (1-\nu)^{3/2}\right] + \frac{\nu}{4}\left(\sqrt{1+\nu} - \sqrt{1-\nu} - \nu\ln\nu\right) + \\ &+ \frac{\nu}{2}\left[\left(1+\frac{\nu}{2}\right)\ln\left(\sqrt{1+\nu}-1\right) - \left(1-\frac{\nu}{2}\right)\ln\left(1-\sqrt{1-\nu}\right)\right], \end{aligned} \tag{2.37a}$$

for $\nu \leq 1$ and

$$\begin{aligned} g(\nu) =& \frac{1}{3\nu}(1+\nu)^{3/2} + \frac{\nu}{4}\left(\sqrt{1+\nu} - \ln\nu\right) \\ &+ \frac{\nu}{2}\left[\left(1+\frac{\nu}{2}\right)\ln\left(\sqrt{1+\nu}-1\right) - \frac{\nu}{2}\ln\sqrt{\nu}\right], \end{aligned} \tag{2.37b}$$

for $\nu > 1$. This is a monotonically decreasing function of its argument ν, as presented in Figure 2.3.

With the use of Eq. (2.35), Landau damping (2.27) can be expressed as

$$\gamma_0^{\mathrm{L}} = \frac{3v_{\mathrm{F}}}{4a} g\left(\frac{\hbar\omega_0}{E_{\mathrm{F}}}\right). \tag{2.38}$$

The above form of the Landau damping agrees with the one proposed by Kawabata and Kubo (1.2) showing inverse proportionality to the size of the nanoparticle a. Moreover, the function $g(\nu)$ in Eq. (2.38) is corrected as compared to $g_{\mathrm{KK}}(\nu)$ (1.3) discussed in the introduction.

2.4 Radiation losses

In this section the evaluation of the radiation damping linewidth of the plasmon in its first excited state is presented. Towards this end one may use the Fermi golden rule for the plasmon-photon coupling (2.25)

$$\gamma^{\sigma,\mathrm{r}} = \frac{2\pi}{\hbar} \sum_{\mathbf{k},\hat{\lambda}_{\mathbf{k}}} |\langle 0^{\sigma}, \{1\}_{\mathbf{k},\hat{\lambda}_{\mathbf{k}}} | H_{\mathrm{pl-ph}} | 1^{\sigma}, \{0\}_{\mathbf{k},\hat{\lambda}_{\mathbf{k}}} \rangle|^2 \delta(\hbar\omega_0 - \hbar\omega_{\mathbf{k}}), \quad (2.39)$$

where the state $|\{0\}_{\mathbf{k},\hat{\lambda}_{\mathbf{k}}}\rangle$ describes photon vacuum. The above process describes dissipation of the plasmon through spontaneous emission of a photon. Inserting Eq. (2.25) into (2.39) we get

$$\gamma^{\sigma,\mathrm{r}} = 2\pi^2 \sum_{\mathbf{k},\hat{\lambda}_{\mathbf{k}}} \frac{\omega_0^3 a^3}{\mathcal{V}\omega_{\mathbf{k}}} |\hat{\sigma} \cdot \hat{\lambda}_{\mathbf{k}}|^2 \delta(\omega_0 - \omega_{\mathbf{k}}). \quad (2.40)$$

The sum over the photon polarization $\hat{\lambda}_{\mathbf{k}}$ yields [91]

$$\sum_{\hat{\lambda}_{\mathbf{k}}} |\hat{\sigma} \cdot \hat{\lambda}_{\mathbf{k}}|^2 = 1 - \frac{(\hat{\sigma} \cdot \mathbf{k})^2}{k^2}. \quad (2.41)$$

Inserting the above equation into Eq. (2.40) and changing the summation over photon wave vector $\mathbf{k}$ into integral (i.e. taking limit $\mathcal{V} \to \infty$)

$$\sum_{\mathbf{k}} \to \frac{\mathcal{V}}{8\pi^3} \int \mathrm{d}^3 k, \quad (2.42)$$

yields

$$\gamma^{\sigma,\mathrm{r}} = \frac{\omega_0^3 a^3}{4\pi} \int \mathrm{d}^3 k \, \frac{1}{\omega_{\mathbf{k}}} [1 - (\hat{\sigma} \cdot \hat{k})^2] \delta(\omega - \omega_{\mathbf{k}}). \quad (2.43)$$

Using the spherical coordinates and the dispersion of photons $\omega_{\mathbf{k}} = ck$ one can write

$$\gamma^{\sigma,\mathrm{r}} = \frac{\omega_0^3 a^3}{4\pi c^3} \int_0^{\infty} \mathrm{d}\omega_{\mathbf{k}} \int_0^{2\pi} \mathrm{d}\phi \int_0^{\pi} \mathrm{d}\theta \, \omega_{\mathbf{k}} \sin\theta [1 - (\hat{\sigma} \cdot \hat{k})^2] \delta(\omega - \omega_{\mathbf{k}}). \quad (2.44)$$

Evaluating the above integrals one finds the final result

$$\gamma_0^{\mathrm{r}} = \frac{2\omega_0^4}{3c^3} a^3, \quad (2.45)$$

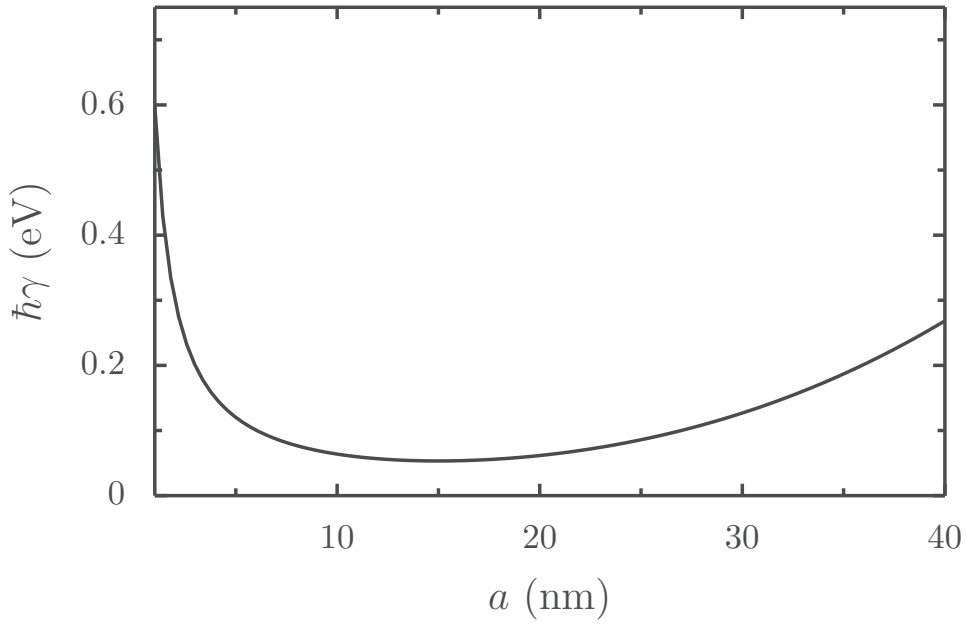

Figure 2.4: Sum of the Landau and radiation damping linewidths as a function of the size a of Ag nanoparticle. In the figure $\hbar\omega_0 = 2.6$ eV and $E_{\mathrm{F}} = 5.49$ eV.

which is polarization-independent, due to the spherical symmetry of the system. Note also that the radiation damping linewidth (2.45) scales with the volume of the particle, which relates to the number of electrons composing the plasmon. The same result for the radiation damping (2.45) can be recovered using classical electrodynamics [70], which we present in Appendix A, but using quantum theory helps to make the presentation more uniform.

2.5 Comparison of Landau and radiation damping

We will now briefly analyze the two different scalings appearing for the Landau and radiation damping linewidths. In Figure 2.4 we present the size dependence of the combined linewidth $\gamma = \gamma_0^{\mathrm{L}} + \gamma_0^{\mathrm{r}}$ for the case of Ag nanoparticle with the Mie frequency $\hbar\omega_0 = 2.6$ eV and $E_{\mathrm{F}} = 5.49$ eV. As seen in the figure there is an interplay between the scalings of the Landau ($\propto 1/a$) and radiation ($\propto a^3$) damping. We see that there exist clear minimum around 15 nm separating the regions dominated by the Landau (lower sizes) and radiation (larger sizes) damping mechanisms. This relation will be modified in the case of nanoparticle dimers once we include interaction between two plasmons, which will be done in the following chapter.

2.6 Conclusion to Chapter 2

In this chapter we have surveyed the theoretical framework used to calculate the radiation and Landau damping decay rate of the localized surface plasmon in single metallic nanoparticles. Starting from the microscopic Hamiltonian in the Coulomb gauge and introducing the relative (electrons) and center-of-mass (plasmon) coordinates allows one to describe how plasmons couple to electronic and photonic bath. Furthermore, with the help of the Fermi golden rule we showed how one can evaluate Landau and radiation damping linewidths. Both of these dampings have different scalings with the size of the nanoparticle. While the former scales with the inverse of the radius $\propto 1/a$ (c.f. Eq. (2.38)) the latter scales with the particle volume $\propto a^3$ (c.f. Eq. (2.45)). Thus, in the case of an isolated spherical nanoparticle, there exists an optimal size at which total linewidth is minimal. This size for the most metals is around $10 - 20$ nm.

The results obtained in this chapter constitute a starting point toward investigating the influence of the presence of other nanoparticles onto the Landau and radiation damping linewidths. In the following chapter we will address the question of how the interaction between plasmons influences their dissipation mechanisms.

Chapter 3

Plasmonic properties of metallic nanoparticle dimers

In this chapter we will investigate the coupled plasmonic modes of a metallic nanoparticle dimer. In Section 3.1 we present the Hamiltonian of the system and derive the couplings present therein. In Section 3.2 we calculate the eigenmodes and evaluate their damping rates for both radiative and non-radiative processes. In Section 3.3 we analyze the obtained rates for various sizes of the system as well as for the cases of the homogeneous and heterogeneous dimers. This chapter is based on the article 1 of my publication list.

3.1 Plasmonic Hamiltonian

We consider a system of two spherical metallic nanoparticles with radii a_1 and a_2, separated by a distance d (as presented in Figure 3.1). The nanoparticles contain respectively N_1 and N_2 electrons. We assume that the interparticle separation d is large enough to neglect the tunneling of electrons and multipolar effects [45]. Under the above assumption we may write the system Hamiltonian within the jellium approximation [88] and in the Coulomb gauge as

$$H = \sum_{n=1}^{2}\sum_{i=1}^{N_n}\left\{\frac{[\mathbf{p}_{n,i} + e\mathbf{A}(\boldsymbol{\rho}_{n,i})]^2}{2m_\mathrm{e}} + U_\mathrm{2NP}(\boldsymbol{\rho}_{n,i})\right\} + \frac{e^2}{2}\sum_{n=1}^{2}\sum_{\substack{i,j=1\\(i\neq j)}}^{N_n}\frac{1}{|\boldsymbol{\rho}_{n,i} - \boldsymbol{\rho}_{n,j}|}$$
$$+e^2\sum_{i=1}^{N_1}\sum_{j=1}^{N_2}\frac{1}{|\boldsymbol{\rho}_{1,i} - \boldsymbol{\rho}_{2,j}|} + H_\mathrm{ph}. \tag{3.1}$$

In the above equation $\boldsymbol{\rho}_{n,i}$ is the position of the i-th electron belonging to the n-th nanoparticle and $\mathbf{p}_{n,i}$ its momentum. The vector potential $\mathbf{A}(\mathbf{r})$ is given in Eq. (2.24). The forth term in Eq. (3.1) describes the electron-electron interaction inside the respective nanoparticles, while

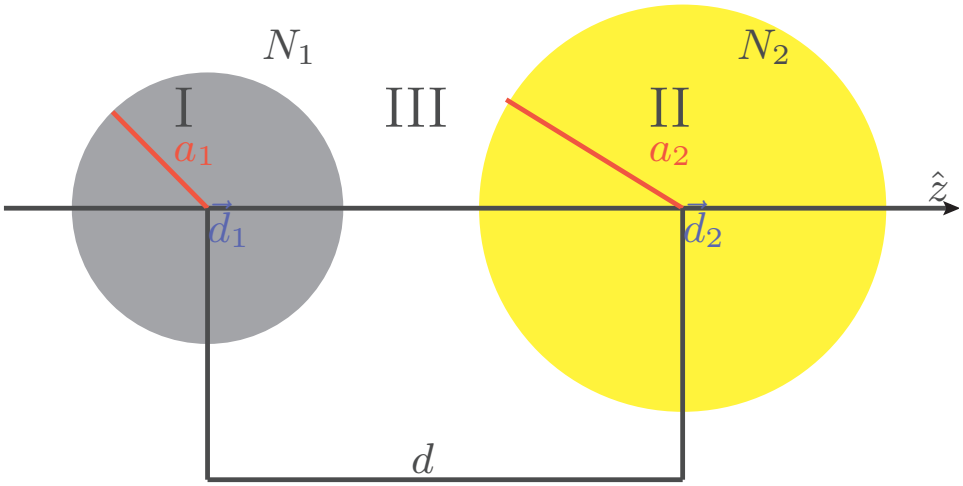

Figure 3.1: Sketch of a heterogeneous nanoparticle dimer composed of two metallic nanoparticles with radii a_1 and a_2 containing, respectively, N_1 and N_2 electrons, separated by a distance d. $\vec{d}_1$ and $\vec{d}_2$ denote the center of nanoparticle 1 and 2, respectively.

the fifth term of the same equation corresponds to interparticle electron-electron interaction. The last term on the right hand side of Eq. (3.1) is the free photon Hamiltonian, c.f. Eq. (2.23).

The single electron confinement potential $U_{2\mathrm{NP}}(\rho)$ created by the two positively charged spheres reads

$$U_{2\mathrm{NP}}(\boldsymbol{\rho}) = \begin{cases} \frac{N_1 e^2}{2a_1^3}(r_1^2 - 3a_1^2) - \frac{N_2 e^2}{r_2} & \rho \in \text{ I} \\ \frac{N_2 e^2}{2a_2^3}(r_2^2 - 3a_2^2) - \frac{N_1 e^2}{r_1} & \rho \in \text{ II} \\ -\frac{N_1 e^2}{r_1} - \frac{N_2 e^2}{r_2} & \rho \in \text{III} \end{cases}, \tag{3.2}$$

where $\mathbf{r}_n = \boldsymbol{\rho} - \mathbf{d}_n$, with $\mathbf{d}_n$ being the location of the center of the n-th nanoparticle. Here, the regions I and II are inside the nanoparticle 1 and 2, respectively, and the region III corresponds to the space outside both nanoparticles (see Figure 3.1). As an example we present a cut of the potential $U_{2\mathrm{NP}}(z)$ along the $\hat{z}$ direction, for the cases of a homogeneous nanoparticle dimer (Figure 3.2(a)) and a heterogeneous dimer with the radii ratio $a_2/a_1 = 1.2$ and frequency ratio $\omega_2/\omega_1 = 1.05$ (Figure 3.2(b)).

Assuming that the interparticle separation d is much larger than the nanoparticle radii a_n, we expand the Hamiltonian (3.1) to second order in r_n/d. Within this approximation, the expansion of the interparticle

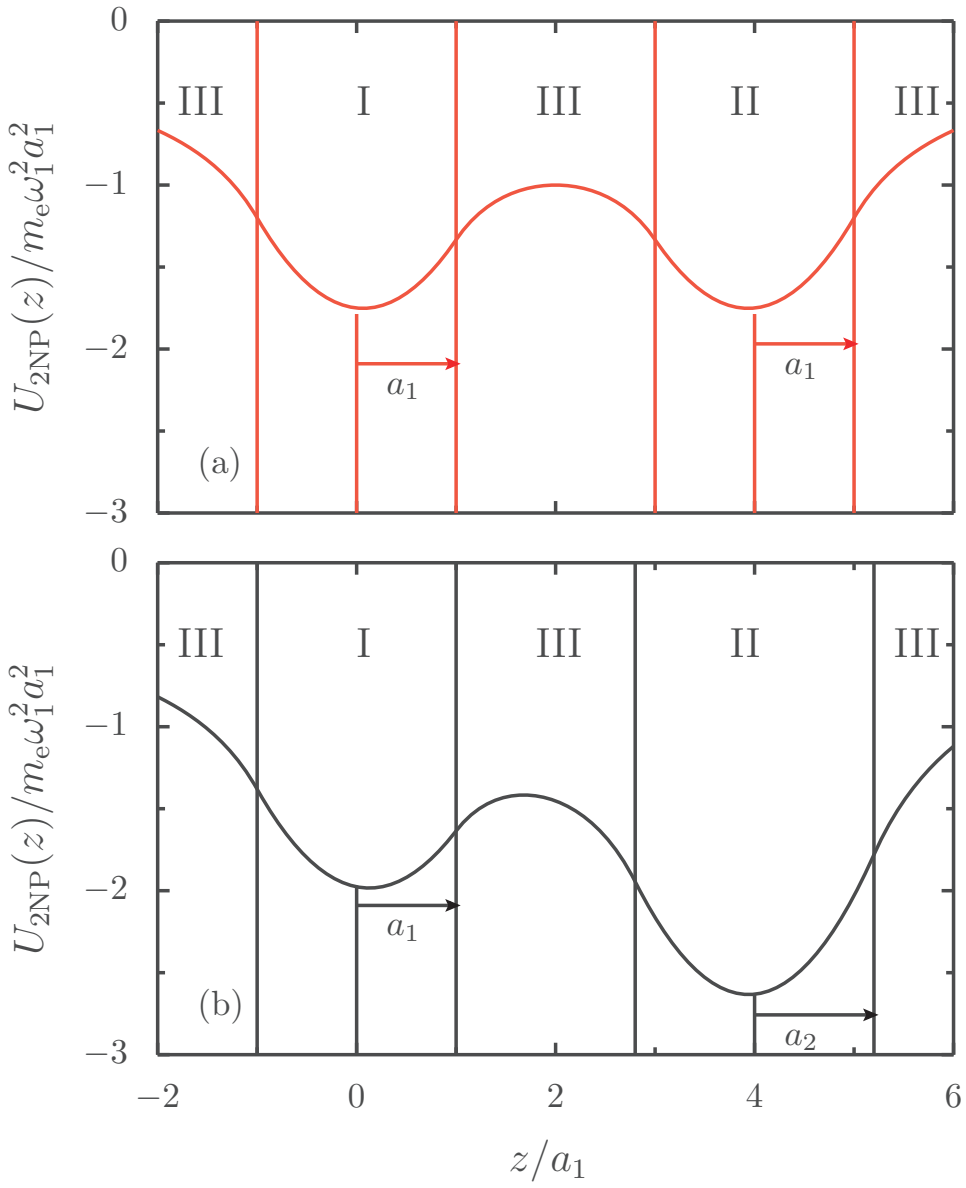

Figure 3.2: Cut along the $\hat{z}$ direction of the single electron confining potential $U_{2NP}(r)$ [Eq. (3.2)] for (a) a homogeneous nanoparticle dimer (red solid line) and (b) a heterogeneous nanoparticle dimer (black solid line). The heterogeneous dimer is described by the radii ratio $a_2/a_1 = 1.2$ and frequency ratio $\omega_2/\omega_1 = 1.05$. Regions I, II and III correspond to the regions depicted in Figure 3.1.

electron-electron interaction entering Eq. (3.1) yields

$$e^2\sum_{i=1}^{N_1}\sum_{j=1}^{N_2}\frac{1}{|\boldsymbol{\rho}_{1,i}-\boldsymbol{\rho}_{2,j}|}\simeq\frac{e^2}{d}\sum_{i=1}^{N_1}\sum_{j=1}^{N_2}\left\{1+\frac{(\mathbf{r}_{1,i}-\mathbf{r}_{2,j})\cdot\hat{\mathbf{d}}}{d}\right.$$
$$\left.-\frac{(\mathbf{r}_{1,i}-\mathbf{r}_{2,j})\cdot[\mathbf{r}_{1,i}-\mathbf{r}_{2,j}-3\hat{\mathbf{d}}(\mathbf{r}_{1,i}-\mathbf{r}_{2,j})\cdot\hat{\mathbf{d}}]}{2d^2}\right\}. \tag{3.3}$$

Here $\mathbf{r}_{n,i}$ denotes the position of i-th electron belonging to the n-th nanoparticle relative to its center and $\hat{\mathbf{d}} = (\mathbf{d}_2 - \mathbf{d}_1)/|\mathbf{d}_2 - \mathbf{d}_1|$. Similarly, the expansion of the single particle confinement (3.2) gives

$$U_{\rm 2NP}(\boldsymbol{\rho}_{1,i}) \simeq U_1(\mathbf{r}_{1,i}) - \frac{N_2 e^2}{d}\left\{1 + \frac{\mathbf{r}_{1,i}\cdot\hat{\mathbf{d}}}{d} - \frac{\mathbf{r}_{1,i}\cdot[\mathbf{r}_{1,i} - \hat{\mathbf{d}}(\mathbf{r}_{1,i}\cdot\hat{\mathbf{d}})]}{2d^2}\right\}, \tag{3.4a}$$

$$U_{\rm 2NP}(\boldsymbol{\rho}_{2,i}) \simeq U_2(\mathbf{r}_{2,i}) - \frac{N_1 e^2}{d}\left\{1 + \frac{\mathbf{r}_{2,i}\cdot\hat{\mathbf{d}}}{d} - \frac{\mathbf{r}_{2,i}\cdot[\mathbf{r}_{2,i} - \hat{\mathbf{d}}(\mathbf{r}_{2,i}\cdot\hat{\mathbf{d}})]}{2d^2}\right\}, \tag{3.4b}$$

where

$$U_n(\mathbf{r}_n) = \frac{N_n e^2}{2a_n^3}(r_n^2 - 3a_n^2)\Theta(a_n - r_n) - \frac{N_n e^2}{r_n}\Theta(r_n - a_n), \tag{3.5}$$

is the single particle confinement potential of an isolated nanoparticle [c.f. Eq. (2.2)].

Using Eqs. (3.3) and (3.4) to express Eq. (3.1), we obtain the Hamiltonian

$$H = \sum_{n=1}^{2} H_n + H_{\rm d-d}, \tag{3.6}$$

up to an irrelevant constant. In Eq. (3.6),

$$H_n = \sum_{i=1}^{N_n}\left[\frac{(\mathbf{p}_{n,i} + e\mathbf{A}(\boldsymbol{\rho}_{n,i}))^2}{2m_{\rm e}} + U_n(\mathbf{r}_{n,i})\right] + \frac{e^2}{2}\sum_{\substack{i,j=1\\ i\neq j}}^{N_n}\frac{1}{|\mathbf{r}_{n,i} - \mathbf{r}_{n,j}|} + H_{\rm ph}, \tag{3.7}$$

representing the Hamiltonian of the single isolated nanoparticle n (c.f. Eq. (2.1)), while

$$H_{\rm d-d} = \frac{e^2}{d^3}\sum_{i=1}^{N_1}\sum_{j=1}^{N_2}[\mathbf{r}_{1,i}\cdot\mathbf{r}_{2,j} - 3(\mathbf{r}_{1,i}\cdot\hat{\mathbf{d}})(\mathbf{r}_{2,j}\cdot\hat{\mathbf{d}})] \tag{3.8}$$

stands for the dipole-dipole interaction between the two electron distributions in the respective nanoparticles. Note that Eq. (3.8) corresponds to the quasi-static form of dipole-dipole interaction, where plasmons (dipoles) interact only via their near fields.

As in Chapter 2, it is convenient to express the Hamiltonian (3.6) using the electronic center-of-mass coordinates $\mathbf{R}_n = \sum_{i=1}^{N_n}\mathbf{r}_{n,i}/N_n$, $\mathbf{P}_n = \sum_{i=1}^{N_n}\mathbf{p}_{n,i}$, and relative coordinates $\mathbf{r}'_{n,i} = \mathbf{r}_{n,i} - \mathbf{R}_n$, $\mathbf{p}'_{n,i} = \mathbf{p}_{n,i} - \mathbf{P}_n/N_n$ $(n = 1, 2)$ [21, 93]. Moreover, expanding the single particle confinement potential $U_n(\mathbf{r}_{n,i})$ up to second order in the parameter $|\mathbf{R}_n|/a_n \ll 1$, we have

$$U_n(\mathbf{r}'_{n,i} + \mathbf{R}_n) - U_n(\mathbf{r}'_{n,i}) \simeq \mathbf{R}_n\cdot\nabla U_n(\mathbf{r}_{n,i}) + \frac{1}{2}(\mathbf{R}_n\cdot\nabla)^2 U_n(\mathbf{r}_n), \tag{3.9}$$

with the derivatives taken at $\mathbf{R}_n = 0$. We then write the Hamiltonian (3.6) as

$$H = H_{\rm pl} + H_{\rm eh} + H_{\rm pl-eh} + H_{\rm ph} + H_{\rm pl-ph}. \tag{3.10}$$

In Eq. (3.10) the plasmonic part of the Hamiltonian $H_{\rm pl}$ reads

$$H_{\rm pl} = \sum_{n=1}^{2}\left(\frac{\mathbf{P}_n^2}{2M_n} + \frac{M_n}{2}\tilde{\omega}_n^2\mathbf{R}_n^2\right) + \frac{Q_1Q_2}{d^3}[\mathbf{R}_1\cdot\mathbf{R}_2 - 3(\mathbf{R}_1\cdot\hat{\mathbf{d}})(\mathbf{R}_2\cdot\hat{\mathbf{d}})], \tag{3.11}$$

with $M_n = N_n m_{\rm e}$ and $Q_n = N_n e$ being the total electronic mass and charge in the n-th nanoparticle, respectively, and $\tilde{\omega}_n$ is the Mie frequency of the plasmon in the n-th nanoparticle red shifted due to the spill-out effect, [1, 18, 88]

$$\tilde{\omega}_n = \omega_n\sqrt{1 - \frac{N_{n,\rm out}}{N_n}}, \quad \omega_n = \sqrt{\frac{N_n e^2}{a_n^3 m_{\rm e}}}. \tag{3.12}$$

In Eq. (3.10),

$$H_{\rm eh} = \sum_{n=1}^{2}\sum_{i=1}^{N_n}\left[\frac{\mathbf{p}'_{n,i}{}^2}{2m_{\rm e}} + U_n(\mathbf{r}'_{n,i})\right] + \frac{e^2}{2}\sum_{n=1}^{2}\sum_{\substack{i,j=1\\ i\neq j}}^{N_n}\frac{1}{|\mathbf{r}'_{n,i} - \mathbf{r}'_{n,j}|} \tag{3.13}$$

represents the Hamiltonian for the relative electronic coordinates, while

$$H_{\rm pl-eh} = \sum_{n=1}^{2}\sum_{i=1}^{N_n}\mathbf{R}_n\cdot\nabla U_n(\mathbf{r}'_{n,i})\big|_{\mathbf{R}_n=0}, \tag{3.14}$$

is the coupling Hamiltonian between the center-of-mass and relative coordinates. As in the case of an isolated nanoparticle (c.f. Chapter 2) this coupling is the consequence of the breakdown of Kohn's theorem [89] by the non-harmonic part of the single electron confinement (3.5) arising from the positive ionic background (see Figure 3.2).

The last term on the right hand side of the total Hamiltonian (3.10) represents the coupling between plasmons and photons, which similarly as in the case of an isolated nanoparticle (c.f. Eq. (2.12)) reads

$$H_{\rm pl-ph} = \frac{e}{m_{\rm e}}\sum_{n=1}^{2}\mathbf{P}_n\cdot\mathbf{A}(\mathbf{d}_n). \tag{3.15}$$

This coupling will lead to the dissipation of plasmons via spontaneous emission of photons.

3.2 Plasmonic eigenmodes

In this section we diagonalize the plasmonic Hamiltonian (3.11) which will lead to new collective modes. These modes will decay due to the

coupling to electronic (3.14) and photonic (3.15) baths. Since the coupling of plasmons to the electron bath leads to the Landau damping, which is a purely quantum mechanical effect, we will work in the second quantization, as in Chapter 2.

3.2.1 Plasmonic Hamiltonian in second quantization

First, let us introduce the annihilation and creation operators

$$b_n^\sigma = \sqrt{\frac{N_n m_\mathrm{e}\tilde{\omega}_n}{2\hbar}}\mathbf{R}_n \cdot \hat{\sigma} + \frac{\mathrm{i}}{\sqrt{2N_n m_\mathrm{e}\hbar\tilde{\omega}_n}}\mathbf{P}_n \cdot \hat{\sigma}, \tag{3.16a}$$

$$b_n^{\sigma\dagger} = \sqrt{\frac{N_n m_\mathrm{e}\tilde{\omega}_n}{2\hbar}}\mathbf{R}_n \cdot \hat{\sigma} - \frac{\mathrm{i}}{\sqrt{2N_n m_\mathrm{e}\hbar\tilde{\omega}_n}}\mathbf{P}_n \cdot \hat{\sigma} \tag{3.16b}$$

for a localized surface plasmon in nanoparticle n with polarization σ. The above operators satisfy the bosonic commutation relations $\left[b_n^\sigma, b_{n'}^{\sigma'\dagger}\right] = \delta_{nn'}\delta_{\sigma\sigma'}$ and $\left[b_n^{\sigma(\dagger)}, b_{n'}^{\sigma'(\dagger)}\right] = 0$.

Using the operators defined in Eq. (3.16) we write the plasmonic Hamiltonian (3.11) as

$$H_\mathrm{pl} = \sum_{n=1}^{2}\sum_{\sigma=x,y,z}\hbar\tilde{\omega}_n b_n^{\sigma\dagger}b_n^\sigma + \hbar\Omega\sum_{\sigma=x,y,z}\eta^\sigma(b_1^\sigma + b_1^{\sigma\dagger})(b_2^\sigma + b_2^{\sigma\dagger}), \tag{3.17}$$

where

$$\Omega = \frac{1}{2}\prod_{n=1}^{2}\left[\frac{\tilde{\omega}_n}{1 - N_{\mathrm{out},n}/N_n}\right]^{1/2}\left(\frac{a_n}{d}\right)^{3/2}, \tag{3.18}$$

with $\eta^{x,y} = 1$ and $\eta^z = -2$.

3.2.2 Diagonalization of the plasmonic Hamiltonian

The quadratic Hamiltonian (3.17) can be diagonalized using the Bogoliubov transformation to read

$$H_\mathrm{pl} = \sum_{\alpha=\pm}\sum_{\sigma=x,y,z}\hbar\omega_\alpha^\sigma B_\alpha^{\dagger\sigma}B_\alpha^\sigma. \tag{3.19}$$

This diagonalization is done based on the general method proposed by Tsalis [90] that we describe in the sequel.

One starts by introducing the operators

$$|\mathbf{b}^\sigma\rangle = \begin{pmatrix} b_1^\sigma \\ b_2^\sigma \\ b_1^{\sigma\dagger} \\ b_2^{\sigma\dagger} \end{pmatrix} \tag{3.20a}$$

$$\langle \mathbf{b}^{\sigma}| = |\mathbf{b}^{\sigma}\rangle^{\dagger} = \begin{pmatrix} b_1^{\sigma\dagger} & b_2^{\sigma\dagger} & b_1^{\sigma} & b_2^{\sigma} \end{pmatrix} \tag{3.20b}$$

and

$$|\mathbf{B}^{\sigma}\rangle = \begin{pmatrix} B_+^{\sigma} \\ B_-^{\sigma} \\ B_+^{\sigma\dagger} \\ B_-^{\sigma\dagger} \end{pmatrix} = \mathcal{T}^{\sigma\dagger} |\mathbf{b}^{\sigma}\rangle , \tag{3.21a}$$

$$\langle \mathbf{B}^{\sigma}| = \begin{pmatrix} B_+^{\sigma\dagger} & B_-^{\sigma\dagger} & B_+^{\sigma} & B_-^{\sigma} \end{pmatrix} = \langle \mathbf{b}^{\sigma}| \mathcal{T}^{\sigma}. \tag{3.21b}$$

The transformation matrix $\mathcal{T}^{\sigma}$ is defined as

$$\mathcal{T}^{\sigma} = \begin{pmatrix} u_{1,+}^{\sigma} & u_{1,-}^{\sigma} & \bar{u}_{1,+}^{\sigma} & \bar{u}_{1,-}^{\sigma} \\ u_{2,+}^{\sigma} & u_{2,-}^{\sigma} & \bar{u}_{2,+}^{\sigma} & \bar{u}_{2,-}^{\sigma} \\ \bar{u}_{1,+}^{\sigma} & \bar{u}_{1,-}^{\sigma} & u_{1,+}^{\sigma} & u_{1,-}^{\sigma} \\ \bar{u}_{2,+}^{\sigma} & \bar{u}_{2,-}^{\sigma} & u_{2,+}^{\sigma} & u_{2,-}^{\sigma} \end{pmatrix} , \tag{3.22}$$

so that the plasmonic Hamiltonian (3.17) can be written as

$$H_{\mathrm{pl}} = \sum_{\sigma=x,y,z} \langle \mathbf{b}^{\sigma}| \mathcal{H}_{\mathrm{pl}}^{\sigma} |\mathbf{b}^{\sigma}\rangle = \sum_{\sigma=x,y,z} \langle \mathbf{B}^{\sigma}| \mathcal{H}_{\mathrm{pl}}^{\sigma\mathrm{D}} |\mathbf{B}^{\sigma}\rangle , \tag{3.23}$$

where we have defined the matrix

$$\mathcal{H}_{\mathrm{pl}}^{\sigma} = \frac{\hbar}{2} \begin{pmatrix} \tilde{\omega}_1 & \eta_{\sigma}\Omega & 0 & \eta_{\sigma}\Omega \\ \eta_{\sigma}\Omega & \tilde{\omega}_2 & \eta_{\sigma}\Omega & 0 \\ 0 & \eta_{\sigma}\Omega & \tilde{\omega}_1 & \eta_{\sigma}\Omega \\ \eta_{\sigma}\Omega & 0 & \eta_{\sigma}\Omega & \tilde{\omega}_2 \end{pmatrix} \tag{3.24}$$

and the diagonalized plasmonic Hamiltonian matrix $\mathcal{H}_{\mathrm{pl}}^{\sigma\mathrm{D}}$

$$\mathcal{H}_{\mathrm{pl}}^{\sigma\mathrm{D}} = \frac{\hbar}{2} \begin{pmatrix} \omega_+^{\sigma} & 0 & 0 & 0 \\ 0 & \omega_-^{\sigma} & 0 & 0 \\ 0 & 0 & \omega_+^{\sigma} & 0 \\ 0 & 0 & 0 & \omega_-^{\sigma} \end{pmatrix} . \tag{3.25}$$

Imposing that the new operators $B_{\pm}^{\sigma}$ are bosonic requires that the coefficients entering the transformation matrix $\mathcal{T}^{\sigma}$ (3.22) obey

$$\sum_{n=1}^{2} (u_{n,\pm}^{\sigma 2} - \bar{u}_{n,\pm}^{\sigma 2}) = 1. \tag{3.26}$$

It is worth writing the commutation relation in a general form as

$$|\mathbf{b}^{\sigma}\rangle \langle \mathbf{b}^{\sigma}| - (\left|\mathbf{b}^{\sigma\dagger}\right\rangle \left\langle \mathbf{b}^{\sigma\dagger}\right|)^{\mathrm{T}} = \mathcal{J} \tag{3.27}$$

where

$$\mathcal{J} = \begin{pmatrix} 1 & 0 & 0 & 0 \\ 0 & 1 & 0 & 0 \\ 0 & 0 & -1 & 0 \\ 0 & 0 & 0 & -1 \end{pmatrix} . \tag{3.28}$$

It is easy to see that the requirement for the new operators $|\mathbf{B}^\sigma\rangle$ to be bosonic amounts to the relation [90]

$$\mathcal{T}^{\sigma\dagger}\mathcal{J}\mathcal{T}^\sigma\mathcal{J} = \mathbb{I}, \tag{3.29}$$

where $\mathbb{I}$ is the unit matrix.

In order for the Hamiltonian (3.17) to be diagonal one needs

$$[H_{\rm pl}, B_\alpha^\sigma] = -\hbar\omega_\alpha^\sigma B_\alpha^\sigma \quad \text{and} \quad \left[H_{\rm pl}, B_\alpha^{\sigma\dagger}\right] = \hbar\omega_\alpha^\sigma B_\alpha^{\sigma\dagger}, \tag{3.30}$$

or in short

$$[H_{\rm pl}, |\mathbf{B}^\sigma\rangle] = -2\mathcal{J}\mathcal{H}_{\rm pl}^{\sigma\rm D}\,|\mathbf{B}^\sigma\rangle\,. \tag{3.31}$$

Making use of Eq. (3.21) one may write Eq. (3.31) as

$$\left[H_{\rm pl}, \mathcal{T}^{\sigma\dagger}\,|\mathbf{b}^\sigma\rangle\right] = \mathcal{T}^{\sigma\dagger}\,[H_{\rm pl}, |\mathbf{b}^\sigma\rangle] = -2\mathcal{T}^{\sigma\dagger}\mathcal{J}\mathcal{H}_{\rm pl}^\sigma\,|\mathbf{b}^\sigma\rangle\,. \tag{3.32}$$

Using now Eqs. (3.21), (3.31) and (3.32) one obtains

$$\mathcal{J}\mathcal{H}_{\rm pl}^{\sigma\rm D}\mathcal{T}^{\sigma\dagger} = \mathcal{T}^{\sigma\dagger}\mathcal{J}\mathcal{H}_{\rm pl}^\sigma, \tag{3.33}$$

or with Eq. (3.29)

$$\mathcal{H}_{\rm pl}^{\sigma\rm D}\mathcal{J} = \mathcal{T}^{\sigma(-1)}\mathcal{H}_{\rm pl}^\sigma\mathcal{J}\mathcal{T}^\sigma. \tag{3.34}$$

Thus in order to obtain the diagonal form of the plasmonic Hamiltonian (3.17) one needs to diagonalize the matrices $2\mathcal{H}_{\rm pl}^\sigma\mathcal{J}$ for each σ. The condition $\det\{\mathcal{H}_{\rm pl}^\sigma\mathcal{J} - \hbar\omega\mathbb{I}\} = 0$ yields the eigenvalue equation

$$(\omega^2 - \tilde{\omega}_1^2)(\omega^2 - \tilde{\omega}_2^2) = 4\eta_\sigma^2\Omega^2\tilde{\omega}_1\tilde{\omega}_2. \tag{3.35}$$

Solving this equation yields the eigenfrequencies of the coupled plasmonic modes

$$\omega_\alpha^\sigma = \sqrt{\frac{(\tilde{\omega}_1 + \tilde{\omega}_2)^2}{4} + \alpha\sqrt{\frac{(\tilde{\omega}_1^2 - \tilde{\omega}_2^2)^2}{4} + 4\eta_\sigma^2\Omega^2\tilde{\omega}_1\tilde{\omega}_2}}, \tag{3.36}$$

with $\alpha = \pm$.

The eigenvectors of the matrix $2\mathcal{H}_{\rm pl}^\sigma\mathcal{J}$ determine the coefficients of the transformation matrix $\mathcal{T}^\sigma$ (3.22) through

$$\begin{pmatrix} \tilde{\omega}_1 - \omega_\pm^\sigma & \eta_\sigma\Omega & 0 & \eta_\sigma\Omega \\ \eta_\sigma\Omega & \tilde{\omega}_2 - \omega_\pm^\sigma & \eta_\sigma\Omega & 0 \\ 0 & \eta_\sigma\Omega & -\tilde{\omega}_1 - \omega_\pm^\sigma & -\eta_\sigma\Omega \\ \eta_\sigma\Omega & 0 & -\eta_\sigma\Omega & -\tilde{\omega}_2 - \omega_\pm^\sigma \end{pmatrix} \begin{pmatrix} u_{1,\pm}^\sigma \\ u_{2,\pm}^\sigma \\ \bar{u}_{1,\pm}^\sigma \\ \bar{u}_{2,\pm}^\sigma \end{pmatrix} = 0. \tag{3.37}$$

Solving the above system of equations and making use of the condition (3.26), as well as, (3.35) results in coefficients of the form

$$u_{n,\alpha}^\sigma = \text{sign}[\alpha\eta_\sigma]^{n-1}\,\frac{\omega_\alpha^\sigma + \tilde{\omega}_n}{2\sqrt{\tilde{\omega}_n\omega_\alpha^\sigma}}\sqrt{\frac{\omega_\alpha^{\sigma 2} - \tilde{\omega}_{\hat{n}}^2}{2\omega_\alpha^{\sigma 2} - \tilde{\omega}_1^2 - \tilde{\omega}_2^2}}, \tag{3.38}$$

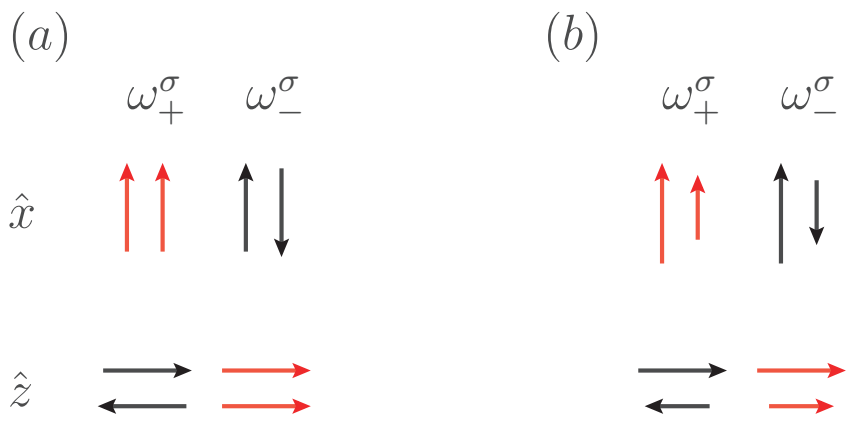

Figure 3.3: Sketch of plasmonic eigenmodes for (a) a homogeneous and (b) a heterogeneous nanoparticle dimer.

and

$$\bar{u}_{n,\alpha}^{\sigma} = \text{sign}[\alpha\eta_\sigma]^{n-1} \frac{\omega_\alpha^\sigma - \tilde{\omega}_n}{2\sqrt{\tilde{\omega}_n \omega_\alpha^\sigma}} \sqrt{\frac{\omega_\alpha^{\sigma 2} - \tilde{\omega}_{\hat{n}}^2}{2\omega_\alpha^{\sigma 2} - \tilde{\omega}_1^2 - \tilde{\omega}_2^2}}, \tag{3.39}$$

where $\hat{n} = 1(2)$ for $n = 2(1)$.

The new collective plasmonic modes have an intuitive pictorial representation. In Figure 3.3 we present a sketch of the $\pm$ plasmonic modes for different polarizations ($\hat{\sigma} = \hat{x}(\hat{y}), \hat{z}$, transverse and longitudinal, respectively). In addition, we color-coded the strength of the interaction between the $\pm$ plasmons and the light, noting that for antiparallel alignment of the plasmons (+ mode in transverse direction and $-$ mode in longitudinal direction) we have a low net dipole moment, meaning weak coupling to the light. Thus, we refer to these modes as *dark* while the other two (red arrows in Figure 3.3) as *bright*.

In Figure 3.4 we present the eigenfrequencies [c.f. Eq. (3.36)] as a function of the interparticle separation d defined in Figure 3.1. We see that the dependence of $\omega_\pm^\sigma$ on the interparticle distance comes from the coupling constant Ω [c.f. Eq. (3.18)] and it is proportional to d^{-3}. The limit of vanishing coupling $\Omega/\sqrt{\omega_1\omega_2} \to 0$ (i.e. $(a_q a_2/d^2)^{(3/2)} \to 0$ corresponds to isolated particles (dotted lines in Figure 3.4). For the heterogeneous dimer (thick red and black lines on Figure 3.4) we use the parameters from the previous section (i.e. $a_2/a_1 = 1.2$ and $\omega_2/\omega_1 = 1.05$). In Figure 3.4 we observe changes in frequencies approximately proportional to d^{-3} that reach asymptotic values (dotted lines) of $\Omega/\sqrt{\omega_1\omega_2} \to 0$ rather quickly. We see a stronger modulation of frequency for the longitudinal modes (over 5% between $d/\sqrt{a_1 a_2} = 3$ to 4) as compared to the transverse ones. These results are consistent

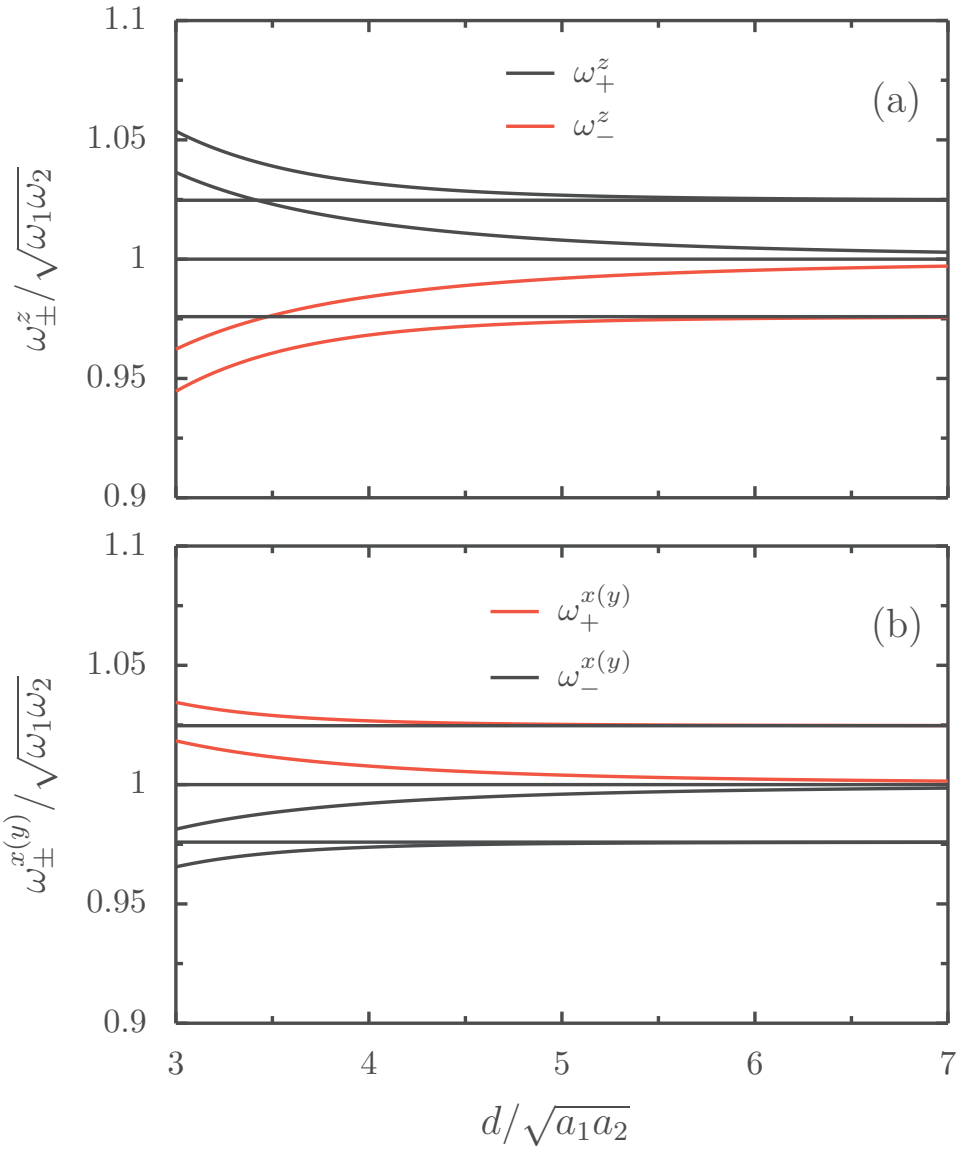

Figure 3.4: Eigenfrequencies of the ± plasmonic modes defined in Eq. (3.36) as a function of interparticle distance d for the (a) longitudinal and (b) transverse directions. Thick red and black lines correspond to respectively bright and dark plasmonic modes of a heterogeneous dimer with radii ratio $a_2/a_1 = 1.2$ and frequency ration $\omega_2/\omega_1 = 1.05$. Thin red and black lines correspond to respectively bright and dark plasmonic modes of a homogeneous dimer. Dotted lines represent asymptotes for $\Omega/\sqrt{\omega_1\omega_2} \to 0$.

with both, experimental [79, 80, 86] and theoretical [33, 73, 75, 77, 82] findings.

3.3 Landau damping

Now that we obtained the eigenstates of the coupled system, we may address their lifetime. We first treat the purely quantum dissipation channel, which comes from the coupling of plasmons to electrons [c.f. Eq. (3.14)].

3.3.1 Second quantized Hamiltonian

Assuming that electronic correlations are not important for the present problem, similarly as in Eq. (2.16) we approximate the Hamiltonian (3.13) by its mean-field counterpart

$$H_{\mathrm{eh}} = \sum_{n=1}^{2} \sum_{\alpha} \varepsilon_{n\alpha} c_{n\alpha}^{\dagger} c_{n\alpha}, \tag{3.40}$$

where $c_{n\alpha}^{\dagger}$ ($c_{n\alpha}$) creates (annihilates) electron in a state $|n\alpha\rangle$ with energy $\varepsilon_{n\alpha}$ in a self-consistent potential V_n. Note that the form of Eq. (3.40) implicitly assumes that tunneling of electrons between the two nanoparticles is suppressed. Density functional theory calculations [75] suggest that the self-consistent potential V can be approximated by two spherical square wells of height V_0 centered around each nanoparticle

$$V(\boldsymbol{\rho}) = \begin{cases} 0 & \boldsymbol{\rho} \in \text{ I \& II} \\ V_0 & \boldsymbol{\rho} \in \text{ III} \end{cases}, \tag{3.41}$$

where regions I and II correspond to the inside of the first and second nanoparticle respectively, and region III is outside of the nanoparticles (see Figure 3.1).

With our mean-field approximation the coupling between the center of mass and relative coordinates (3.14) takes the form

$$\begin{aligned} H_{\mathrm{pl-eh}} = & \sum_{n=1}^{2} \sum_{\sigma=x,y,z} \sum_{\alpha\beta} \sqrt{\frac{\hbar}{2m_{\mathrm{e}} N_n \tilde{\omega}_n}} \left(b_n^{\sigma\dagger} + b_n^{\sigma}\right) \\ & \times \langle n\alpha \left| \hat{\sigma} \cdot \nabla U_n(r) \right| n\beta \rangle c_{n\alpha}^{\dagger} c_{n\beta}. \end{aligned} \tag{3.42}$$

By relating the collective and relative coordinates, this expression provides a way to calculate the decay rate of the coupled plasmonic modes within a quantum-mechanical approach.

3.3.2 Fermi's golden rule

We now turn to the evaluation of the non-radiative linewidth of the collective plasmonic modes. Their Landau damping decay rates are

given by the zero-temperature Fermi's golden rule as

$$\begin{aligned}\gamma_{\pm}^{\sigma,\mathrm{L}} =& \frac{2\pi}{\hbar}\sum_{n=1}^{2}\sum_{eh}\left|\left\langle\{eh\}_n,\{0\}_{\pm}^{\sigma}\right|H_{\mathrm{pl-eh}}\left|\{0\}_n,\{1\}_{\pm}^{\sigma}\right\rangle\right|^2 \\ &\times\delta(\hbar\omega_{\pm}^{\sigma}-E_{ne}+E_{nh}),\end{aligned} \tag{3.43}$$

where the sum $\sum_{eh}$ runs over all electron and hole states, $|e_n\rangle$ and $|h_n\rangle$ respectively, in each nanoparticle. The state $\left|\{1\}_{\pm}^{\sigma}\right\rangle$ represents a collective $\pm$ plasmon in the first excited state with polarization σ. Inserting the coupling Hamiltonian from Eq. (3.42) and inverting the transformation for bosonic operators $B_{\pm}^{\sigma}$ defined in Eq. (3.21)

$$\begin{aligned}|\mathbf{b}^{\sigma}\rangle &= \left(\mathcal{T}^{\sigma\dagger}\right)^{-1}|\mathbf{B}^{\sigma}\rangle = \mathcal{J}\mathcal{T}^{\sigma}\mathcal{J}\,|\mathbf{B}^{\sigma}\rangle \\ &= \begin{pmatrix} u_{1,+}^{\sigma} & u_{1,-}^{\sigma} & -\bar{u}_{1,+}^{\sigma} & -\bar{u}_{1,-}^{\sigma} \\ u_{2,+}^{\sigma} & u_{2,-}^{\sigma} & -\bar{u}_{2,+}^{\sigma} & -\bar{u}_{2,-}^{\sigma} \\ \bar{u}_{1,+}^{\sigma} & \bar{u}_{1,-}^{\sigma} & -u_{1,+}^{\sigma} & -u_{1,-}^{\sigma} \\ \bar{u}_{2,+}^{\sigma} & \bar{u}_{2,-}^{\sigma} & -u_{2,+}^{\sigma} & -u_{2,-}^{\sigma} \end{pmatrix}\begin{pmatrix} B_{+}^{\sigma} \\ B_{-}^{\sigma} \\ B_{+}^{\sigma\dagger} \\ B_{-}^{\sigma\dagger} \end{pmatrix},\end{aligned} \tag{3.44}$$

we write the Landau damping linewidth as

$$\begin{aligned}\gamma_{\pm}^{\sigma,\mathrm{L}} =& \frac{2\pi}{\hbar}\sum_{n=1}^{2}\sum_{eh}\left|\left\langle\{eh\}_n,\{0\}_{\pm}^{\sigma}\right|\sum_{n'=1}^{2}\sum_{\sigma'=x,y,z}\sum_{\alpha\beta}\sum_{\tau=\pm}\Lambda_{n'}\Delta u_{n'\tau}^{\sigma'}\hat{\sigma}'\cdot\mathbf{d}_{\alpha\beta}^{n'}\right. \\ &\left.\times\left(B_{\tau}^{\sigma'}+B_{\tau}^{\sigma'\dagger}\right)c_{n'\alpha}^{\dagger}c_{n'\beta}\left|\{0\}_n,\{1\}_{\pm}^{\sigma}\right\rangle\right|^2\delta(\hbar\omega_{\pm}^{\sigma}-E_{ne}+E_{nh}),\end{aligned} \tag{3.45}$$

where

$$\Lambda_n = \sqrt{\frac{\hbar m_{\mathrm{e}}\omega_n^3}{2N_n}}, \tag{3.46}$$

and

$$\Delta u_{n\pm}^{\sigma} = u_{n\pm}^{\sigma} - \bar{u}_{n\pm}^{\sigma}. \tag{3.47}$$

In evaluating Eq. (3.45) we approximated the self-consistent potential V (3.41) as infinite outside the nanoparticles, thus neglecting the spill-out effect. Such an assumption is justified by density functional theory calculations for dimers, [75] as well as the assumption that the plasmon energies for the considered nanoparticles are smaller than the work function. The dipole matrix elements $\mathbf{d}_{\alpha\beta}^{\sigma,n} = \langle n\alpha|\,\hat{\sigma}\cdot\nabla U_n(r)\,|n\beta\rangle$ evaluated under the above approximation yield

$$\mathbf{d}_{\alpha\beta}^{n} = \mathcal{R}_n(E_\alpha,E_\beta)\left(\sum_{s=\pm}\mathcal{A}_{\ell_\alpha\ell_\beta s}^{m_\alpha m_\beta}\frac{\hat{x}-\mathrm{i}s\hat{y}}{\sqrt{2}}+\mathcal{A}_{\ell_\alpha\ell_\beta 0}^{m_\alpha m_\beta}\hat{z}\right) \tag{3.48}$$

with the radial part given by [17]

$$\mathcal{R}_n(E_\alpha,E_\beta) = \frac{2\hbar^2}{m_{\mathrm{e}}a_n}\frac{\sqrt{E_\alpha E_\beta}}{(E_\alpha-E_\beta)^2}. \tag{3.49}$$

The angular part of Eq. (3.48) is expressed in terms of Wigner-3j symbols, see Eq. (2.21).

Simplifying Eq. (3.45) we get

$$\gamma_{\pm}^{\sigma,\mathrm{L}} = \frac{2\pi}{\hbar} \sum_{n=1}^{2} \sum_{eh} |\Lambda_n \Delta u_{n,\pm}^{\sigma} \hat{\sigma} \cdot \mathbf{d}_{eh}^{n}|^2 \delta(\hbar\omega_{\pm}^{\sigma} - E_{ne} + E_{nh}). \tag{3.50}$$

Evaluating the above expression gives the Landau damping linewidth in the form

$$\gamma_{\pm}^{\sigma,\mathrm{L}} = \sum_{n=1}^{2} \Delta u_{\pm,n}^{\sigma 2} \Sigma_n^{\sigma}(\omega_{\pm}^{\sigma}), \tag{3.51}$$

with

$$\Sigma_n^{\sigma}(\omega) = \frac{2\pi}{\hbar^2} \Lambda_n^2 \sum_{eh} |\langle e|\hat{\sigma} \cdot \mathbf{r}|h\rangle|^2 \delta(\omega - \omega_{eh}), \tag{3.52}$$

where $\omega_{eh} = (\varepsilon_e - \varepsilon_h)/\hbar$. The expression for $\Sigma^{\sigma}(\omega)$ was evaluated in Chapter 2 to yield Eq. (2.35). Thus, evaluating Eq. (3.51), we write the Landau damping linewidth in the form

$$\gamma_{\pm}^{\sigma,\mathrm{L}} = \sum_{n=1}^{2} \frac{3v_{\mathrm{F}}^{n}}{4a_n} \Delta u_{\pm,n}^{\sigma 2} \left(\frac{\omega_n}{\omega_{\pm}^{\sigma}}\right)^3 g\left(\frac{\hbar\omega_{\pm}^{\sigma}}{E_{\mathrm{F}}^{n}}\right), \tag{3.53}$$

where the function $g(\nu)$ is defined in Eq. (2.37).

For the homogeneous dimer Eq. (3.53) simplifies to

$$\gamma_{\pm}^{\sigma,\mathrm{L,hom.}} = \frac{3v_{\mathrm{F}}}{4a} \left(\frac{\omega_0}{\omega_{\pm}^{\sigma 4}}\right)^4 g\left(\frac{\hbar\omega_{\pm}^{\sigma}}{E_{\mathrm{F}}}\right). \tag{3.54}$$

In Figure 3.5 we present the behavior of the Landau damping decay rate for the homogeneous and heterogeneous nanoparticle dimers [Eqs. (3.53) and (3.54)] with varying nanoparticle separation d. We observe a decrease (increase) of the Landau damping with the increasing interparticle distance for the $-$ ($+$) modes, which is opposite of the trends for the eigenfrequencies, see Figure 3.4. In addition, we see a much bigger modulation, going up to 25% for the longitudinal modes [see Figure 3.5(a)]. Moreover, we observe a crossover between the dark and bright modes in the case of the longitudinal modes of the heterogeneous dimer [thick red and black solid lines in Figure 3.5(a)].

The increase of Landau damping with decreasing interparticle distance d for the longitudinal bright mode [red thin and thick lines in Figure 3.5(a)] is consistent with density functional calculations [75]. Note that in the density functional calculations the authors of Ref. [75] only considered internal processes, thus the origin of the damping presented in their work was only quantum (i.e. Landau damping).

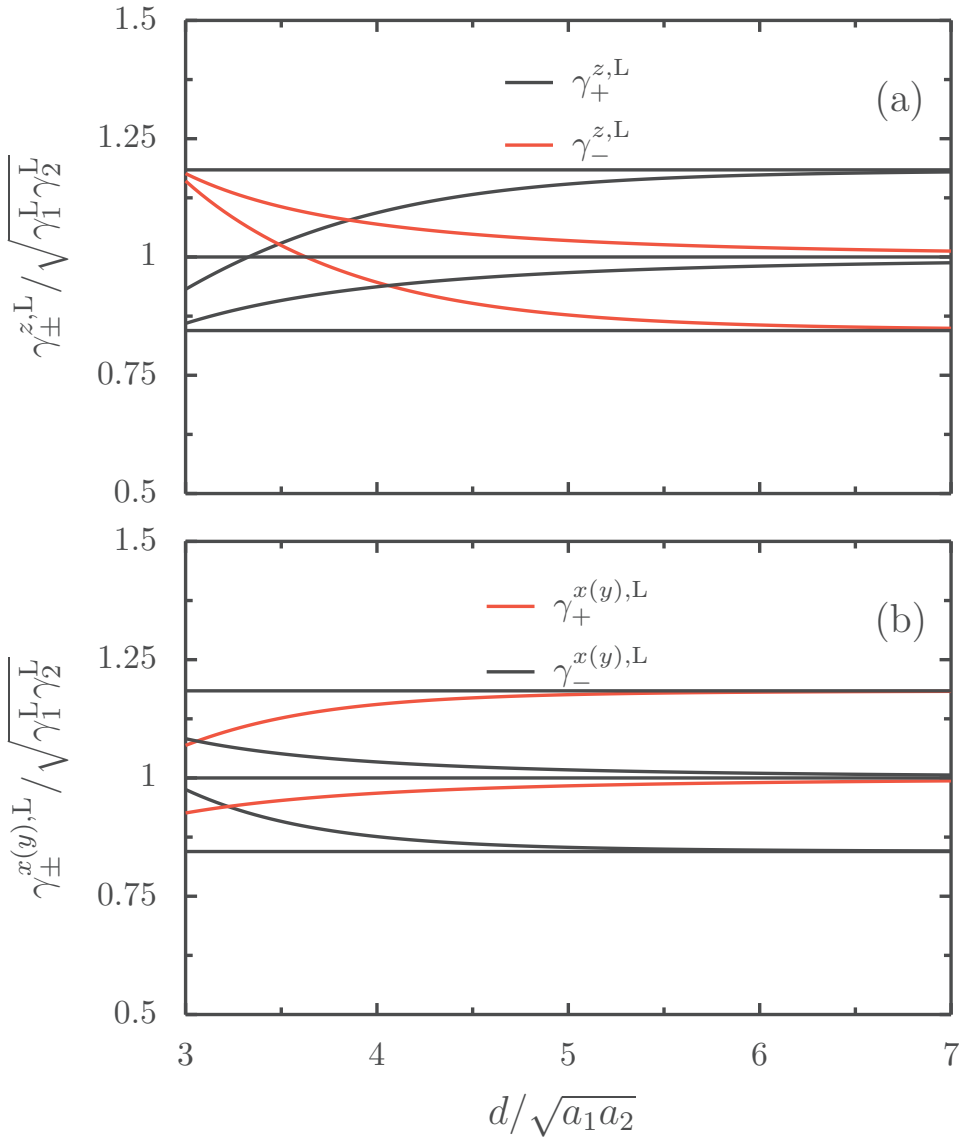

Figure 3.5: Landau damping $\gamma_\pm^{\sigma,\mathrm{L}}$ [c.f. Eq. (2.29)] as a function of the interparticle distance d for the (a) longitudinal and (b) transverse directions. Thick red and black lines correspond to, respectively, bright and dark plasmonic modes of the heterogeneous dimer with radii ratio $a_2/a_1 = 1.2$ and frequency ration $\omega_2/\omega_1 = 1.05$. Thin red and black lines correspond to respectively bright and dark plasmonic modes of the homogeneous dimer. Dotted lines represent asymptotes for $\Omega/\sqrt{\omega_1\omega_2} \to 0$. On the figure γ_n^{L} is the Landau damping of an isolated nanoparticle n.

3.4 Radiation damping

In this section we address the other mechanism of dissipation of the coupled plasmonic modes described by their coupling to the photonic bath (3.15). This mechanism classically is described by the radiation

of accelerated charges. Thus, this section will be a revisit of the related problem of radiation from two point dipoles [76].

Inserting the expression for the momentum conjugated to the center-of-mass displacements

$$\mathbf{P}_n = \mathrm{i}\sqrt{\frac{N_n m_e \hbar \omega_n}{2}} \sum_{\sigma=x,y,z} \hat{\sigma} \left(b_n^{\sigma\dagger} - b_n^{\sigma} \right), \tag{3.55}$$

and the expression of vector potential $\mathbf{A}(\mathbf{r})$ (2.24) into the coupling Hamiltonian (3.15) we get

$$\begin{aligned} H_{\mathrm{pl-ph}} =& \mathrm{i}\hbar \sum_{\sigma=x,y,z} \sum_{n=1}^{2} \sum_{\mathbf{k},\hat{\lambda}_{\mathbf{k}}} \sqrt{\frac{\pi \omega_n^3 a_n^3}{\mathcal{V}\omega_{\mathbf{k}}}} \left(b_n^{\sigma\dagger} - b_n^{\sigma} \right) \\ & \times \left(\hat{\sigma} \cdot \hat{\lambda}_{\mathbf{k}} a_{\mathbf{k},\hat{\lambda}_{\mathbf{k}}} e^{\mathrm{i}\mathbf{k}\cdot\mathbf{d}_n} + \hat{\sigma} \cdot \hat{\lambda}_{\mathbf{k}}^{*} a_{\mathbf{k},\hat{\lambda}_{\mathbf{k}}}^{\dagger} e^{-\mathrm{i}\mathbf{k}\cdot\mathbf{d}_n} \right). \end{aligned} \tag{3.56}$$

Using the inverse transformation for $B_{\pm}^{\sigma}$ Eq. (3.44), we write the coupling Hamiltonian (3.56) in the following form

$$\begin{aligned} H_{\mathrm{pl-ph}} =& \mathrm{i}\hbar \sum_{\sigma=x,y,z} \sum_{n=1}^{2} \sum_{\tau=\pm} \sum_{\mathbf{k},\hat{\lambda}_{\mathbf{k}}} \sqrt{\frac{\pi \omega_n^3 a_n^3}{\omega_{\mathbf{k}}\mathcal{V}}} U_{n,\tau}^{\sigma} \left(B_{\tau}^{\sigma\dagger} - B_{\tau}^{\sigma} \right) \\ & \times \left(\hat{\sigma} \cdot \hat{\lambda}_{\mathbf{k}} a_{\mathbf{k},\hat{\lambda}_{\mathbf{k}}} e^{\mathrm{i}\mathbf{k}\cdot\mathbf{d}_n} + \hat{\sigma} \cdot \hat{\lambda}_{\mathbf{k}}^{*} a_{\mathbf{k},\hat{\lambda}_{\mathbf{k}}}^{\dagger} e^{-\mathrm{i}\mathbf{k}\cdot\mathbf{d}_n} \right), \end{aligned} \tag{3.57}$$

where $U_{n,\tau}^{\sigma} = u_{n,\tau}^{\sigma} + \bar{u}_{n,\tau}^{\sigma}$.

3.4.1 Fermi's golden rule

In a similar manner as in the case of the Landau damping, we now turn to the evaluation of the Fermi golden rule for the coupling Hamiltonian (3.57) in order to get the radiative decay rate for the collective plasmonic modes. The golden rule reads

$$\gamma_{\pm}^{\sigma,\mathrm{r}} = \frac{2\pi}{\hbar} \sum_{\mathbf{k},\hat{\lambda}_{\mathbf{k}}} \left| \langle \{1\}_{\mathbf{k},\hat{\lambda}_{\mathbf{k}}}, \{0\}_{\pm}^{\sigma} | H_{\mathrm{pl-ph}} | \{0\}_{\mathbf{k},\hat{\lambda}_{\mathbf{k}}}, \{1\}_{\pm}^{\sigma} \rangle \right|^2 \delta(\hbar\omega_{\pm}^{\sigma} - \hbar\omega_{\mathbf{k}}), \tag{3.58}$$

and represents the process of annihilating a plasmon from its first excited state $|\{1\}_{\pm}^{\sigma}\rangle$ and creating a photon in the state $|\{1\}_{\mathbf{k},\hat{\lambda}_{\mathbf{k}}}\rangle$. The summation in Eq. (3.58) runs over all possible photon states with the wavevector $\mathbf{k}$ and polarization $\hat{\lambda}_{\mathbf{k}}$. Inserting the coupling Hamiltonian obtained in Eq. (3.57) to Fermi's golden rule (3.58) we get

$$\gamma_{\pm}^{\sigma,\mathrm{r}} = 2\pi^2 \sum_{\mathbf{k},\hat{\lambda}_{\mathbf{k}}} \frac{1}{\omega_{\mathbf{k}}\mathcal{V}} |\hat{\sigma} \cdot \hat{\lambda}_{\mathbf{k}}|^2 \left| \sum_{n=1}^{2} \sqrt{\omega_n^3 a_n^3} U_{n,\pm}^{\sigma} e^{-\mathrm{i}\mathbf{k}\cdot\mathbf{d}_{\mathrm{n}}} \right|^2 \delta(\omega_{\pm}^{\sigma} - \omega_{\mathbf{k}}). \tag{3.59}$$

Changing the summation in Eq. (3.59) over photon wavevector $\mathbf{k}$ into an integral (2.42) (i.e. taking the continuous limit $\mathcal{V} \to \infty$) we write the radiative decay rate as

$$\gamma_{\pm}^{\sigma,\mathrm{r}} = \frac{1}{4\pi} \int_0^{\infty} \mathrm{d}k k^2 \int_0^{\pi} \mathrm{d}\theta \sin\theta \int_0^{2\pi} \mathrm{d}\phi \, \frac{1}{\omega_{\mathbf{k}}} (1 - |\hat{\sigma} \cdot \hat{k}|^2) \left[\omega_1^3 a_1^3 U_{1,\pm}^{\sigma 2} + \omega_2^3 a_2^3 U_{n,\pm}^{\sigma 2} + 2\sqrt{\omega_1^3 a_1^3 \omega_2^3 a_2^3} U_{1,\pm}^{\sigma} U_{2,\pm}^{\sigma} \cos(kd\cos\theta) \right] \delta(\omega_{\pm}^{\sigma} - \omega_{\mathbf{k}}). \tag{3.60}$$

Note that in evaluating the above expression we used Eq. (2.41). To proceed, we make use of the photon dispersion relation $\omega_k/c = k$ to change the integration variable. Moreover, due to symmetry reasons the radiative decay rates of the plasmons polarized in the transverse ($\hat{x}$ and $\hat{y}$) directions are equal. After evaluating the integral in Eq. (3.60) over ω_k and ϕ we get

$$\gamma_{\pm}^{\sigma,\mathrm{r}} = \frac{|\eta_\sigma| \omega_{\pm}^{\sigma}}{4c^3} \int_{-1}^{1} \mathrm{d}t (1 + \mathrm{sign}[\eta_\sigma] t^2) \left[\omega_1^3 a_1^3 U_{1,\pm}^{\sigma 2} + \omega_2^3 a_2^3 U_{2,\pm}^{\sigma 2} + 2\sqrt{\omega_1^3 a_1^3 \omega_2^3 a_2^3} U_{1,\pm}^{\sigma} U_{2,\pm}^{\sigma} \cos(\omega_{\pm}^{\sigma} dt/c) \right], \tag{3.61}$$

where $t = \cos\theta$. The above integral yields the final form for the radiation damping

$$\gamma_{\pm}^{\sigma,\mathrm{r}} = \frac{2\omega_{\pm}^{\sigma}}{3c^3} \left\{ \omega_1^3 a_1^3 U_{1,\pm}^{\sigma 2} + \omega_2^3 a_2^3 U_{2,\pm}^{\sigma 2} + 3\eta_\sigma \sqrt{\omega_1^3 a_1^3 \omega_2^3 a_2^3} U_{1,\pm}^{\sigma} U_{2,\pm}^{\sigma} f_\sigma \left(\frac{\omega_{\pm}^{\sigma} d}{c} \right) \right\}, \tag{3.62}$$

with

$$f_{x(y)}(t) = \left[\frac{\sin t}{t} + \frac{\cos t}{t^2} - \frac{\sin t}{t^3} \right], \tag{3.63}$$

$$f_z(t) = \left[\frac{\cos t}{t^2} - \frac{\sin t}{t^3} \right]. \tag{3.64}$$

Assuming that the interparticle distance d is much smaller than the $\pm$ plasmon wavelengths we expand Eq. (3.62) to third order in the parameter $\omega_{\pm}^{\sigma} d/c \ll 1$ to get the form

$$\gamma_{\pm}^{\sigma,\mathrm{r}} = \frac{2\omega_{\pm}^{\sigma 3}}{3c^3} \left(\sum_{n=1}^{2} \sqrt{\omega_n a_n^3} \Delta u_{n,\pm}^{\sigma} \right)^2, \tag{3.65}$$

where $\Delta u_{n,\pm}^{\sigma}$ were defined in Eq. (3.47).

Rewriting the above expression for the homogeneous dimer gives

$$\gamma_{\pm}^{\sigma,\mathrm{r,hom.}} = \frac{\omega_0^2 \omega_{\pm}^{\sigma 2}}{3c^3} a^3 \left(1 \pm \mathrm{sign}[\eta_\sigma]\right)^2 = \gamma_0^{\mathrm{r}} \frac{\omega_{\pm}^{\sigma 2}}{2\omega_0^2} \left(1 \pm \mathrm{sign}[\eta_\sigma]\right)^2 , \quad (3.66)$$

where γ_0^{r} is the single nanoparticle plasmon radiation decay [c.f. Eq. (2.45)]. From the above equation we see that for the dark modes (+ mode in $\hat{z}$ direction and − modes in $\hat{x}$ and $\hat{y}$ directions) we have a vanishing radiation damping. The immunity to radiation losses makes these modes interesting from the point of view of the energy storage. Although, there exist a setback regarding inability to excite these modes using light, this issue is resolved using the electric field of an electron beam in EELS (electron energy loss spectroscopy) experiments [62, 84, 85]. Although immune to radiation damping, dark modes are still subject to Landau damping (3.54) and Ohmic losses.

We present the radiation damping [Eqs. (3.65) and (3.66)] as a function of the interparticle distance d for the homogeneous and heterogeneous nanoparticle dimer in Figure 3.6. We observe a very small modulation for the bright modes of the homogeneous dimer (thin red solid lines), while the dark modes, as shown in Eq. (3.66), have vanishing radiation damping (thick dashed black lines). In contrast, we see a much larger modulation in the case of the heterogeneous dimer (thick solid red and black lines). In the transverse direction [panel (b) of Figure 3.6], we have a monotonic change of radiation damping for both dark and bright modes. The observed modulation for the transverse modes exceeds 50%. Note that the modulation of the Landau damping for the transverse modes [see Figure 3.5(b)] reached around 10%. The situation is even more interesting for the longitudinal mode, where as in the case of Landau damping [thick red and black solid lines in Figure 3.5(a)] we observe a crossover between the bright and dark modes [thick red and black solid lines in Figure 3.6 (b)]. In addition, we observe a much larger modulation for the dark longitudinal mode (reaching almost 100%), as compared to all the other modes.

For large interparticle distances d (i.e. $d/\sqrt{a_1 a_2} \simeq 7$) in the case of the bright homogeneous nanoparticle modes (thin red solid lines in Figure 3.6), the value of the radiation damping linewidth is the double of that of an isolated nanoparticle. The reason is that in this regime we may view the power radiated from the system as coming from a single point, with twice the number of electrons of each nanoparticle.

The observed trends of the bright longitudinal mode damping rates (increase of both Landau and radiation damping with decreasing distance d) are consistent with experimental findings [79, 80, 86]. For the case of the bright transverse modes, Refs. [79, 80, 86] found that the full width at half maximum of the plasmon resonance is also increasing with decreasing interparticle distance d. Our results show a competition between radiation (increase of the linewidth with decreasing d) and

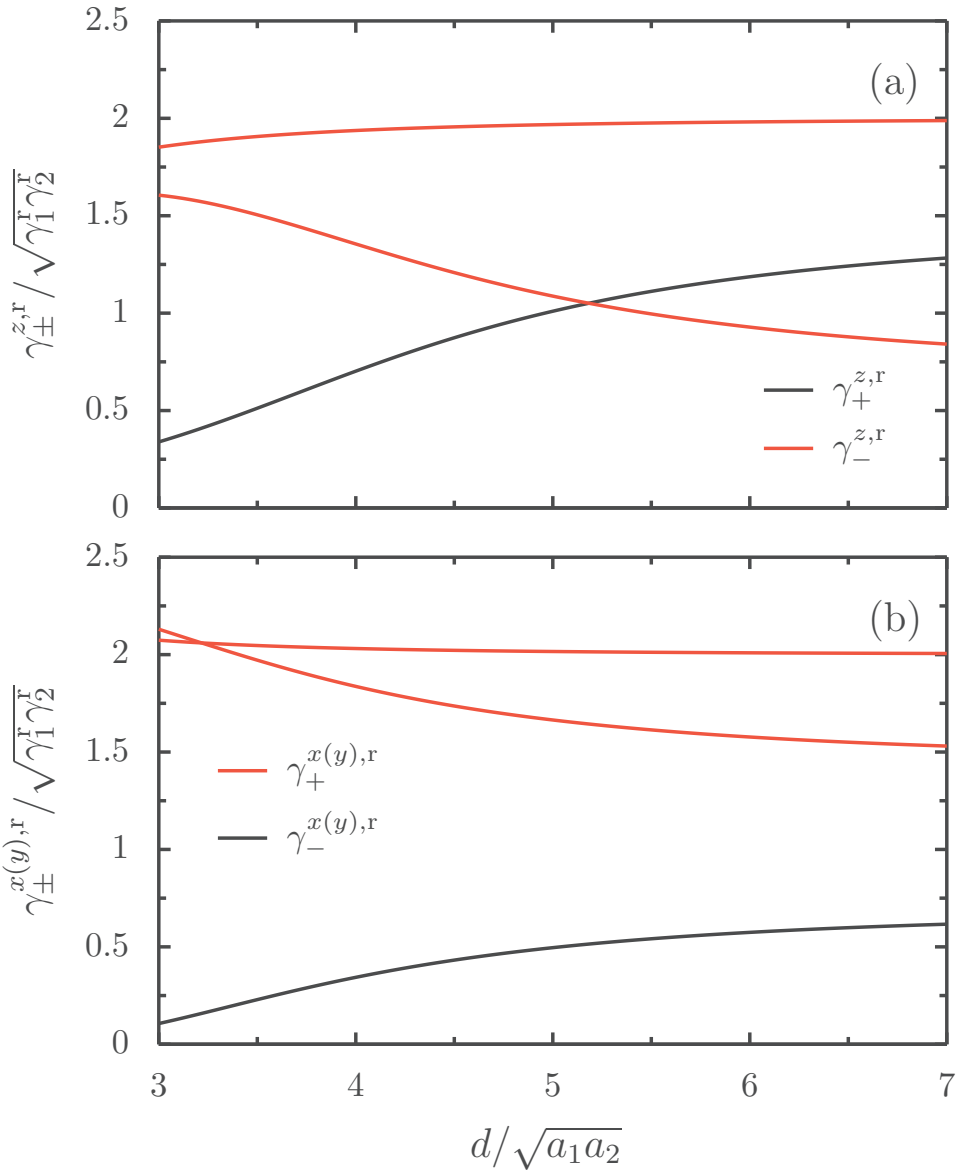

Figure 3.6: Radiation damping $\gamma_\pm^{\sigma,\mathrm{r}}$ [c.f. Eq. (3.65)] as a function of the interparticle distance d for the (a) longitudinal and (b) transverse directions. Thick red and black lines correspond to respectively bright and dark plasmonic modes of a heterogeneous dimer with radii ratio $a_2/a_1 = 1.2$ and frequency ratio $\omega_2/\omega_1 = 1.05$. Thin red and black dashed lines correspond to respectively bright and dark plasmonic modes of a homogeneous dimer. We note γ_n^r is the radiation damping of an isolated nanoparticle n.

Landau (decrease of the linewidth with decreasing d) damping in this area [see Figures 3.5(b) and 3.6(b)]. This leads to a conclusion that the experiments [79, 80, 86] used nanoparticles for which the radiation damping was dominant.

3.5 Size effects in nanoparticle dimers

Since Landau damping follows a $1/a$ scaling [c.f. Eq. (3.53)], while radiation damping scales as a^3 [c.f. Eq. (3.65)] we will now turn to see these two scalings interplay with each other. To this end we will consider the particular cases of a homogeneous dimer composed of two Ag nanoparticles and a heterogeneous dimer composed of an Ag-Au pair. We take the following values of the Mie frequencies [1] and Fermi energy: $\hbar\omega_{\mathrm{Ag}} = 2.6$ eV, $\hbar\omega_{\mathrm{Au}} = 2.2$ eV, $E_{\mathrm{F}}^{\mathrm{Ag}} = 5.49$ eV, $E_{\mathrm{F}}^{\mathrm{Au}} = 5.53$ eV.

In Figures 3.7 and 3.8 we present the sum of Landau and radiation damping as a function of the nanoparticle size a_1 for the homogeneous (Ag-Ag) and heterogeneous (Ag-Au) dimer, respectively, keeping the ratio of interparticle distance to radius constant (i.e. $d/a_1 = 3$). We observe that for the dark modes of the homogeneous dimer the sum follows only the a^{-1} size dependence of the Landau damping, since it is immune to the radiation losses [c.f. Eq. (3.66)]. In contrast, the case of the dark modes of the heterogeneous dimer is influenced by radiation damping.

For all modes (with the exception of the dark mode of the homogeneous dimer) we observe a clear minimum of the total damping rates. This minimum gives the optimal sizes of the particles for which the lifetime of coupled plasmonic modes is the longest. It is worth mentioning that the minimum damping for the bright mode of the homogeneous dimer (red solid lines in Figure 3.7) is weakly influenced by the polarization, and stays in the range $10 - 15$ nm. The situation is not as simple as in the case of the heterogeneous dimer (see Figure 3.8). We see that the minimal damping for the heterogeneous dimer bright mode in the longitudinal direction is located in a similar range as those of the homogeneous dimer bright modes, while in the case of the transverse directions we see a clear shift of the minimum toward larger radii [panel (b) of Figure 3.8]. The opposite behavior is exhibited by the dark modes of the heterogeneous dimer (black solid lines in Figure 3.8), meaning that the dark mode in the longitudinal direction has a minimum at a larger size than the one in the transverse direction.

As we saw in Figures 3.7 and 3.8, there exist certain sizes of the nanoparticles at which damping is minimal, with the exception of the dark modes of the homogeneous dimer. Note that the latter follows from the fact that the interparticle distance d is much smaller than the wavelength of the plasmons, leading to radiation damping in the form (3.65). In reality, even for the dark modes of the homogeneous dimer radiation damping will get noticeably bigger for increased size of the nanoparticles and/or interparticle separation. Moreover, this scenario exceeds the scope of our approximations.

We will now turn to a broader picture of the damping and analyze

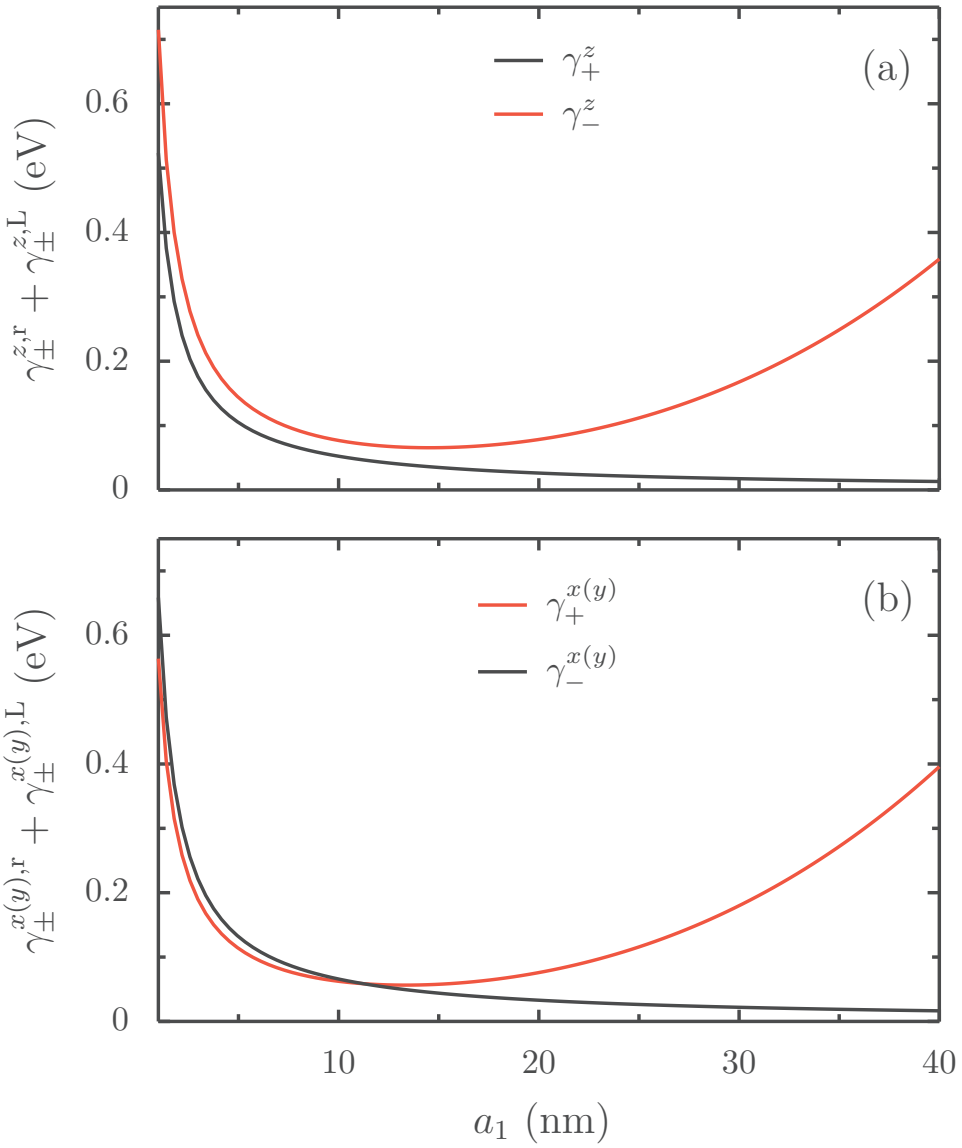

Figure 3.7: Sum of radiation and Landau damping of a homogeneous (Ag-Ag) nanoparticle dimer as a function of the nanoparticle size a_1 for the (a) longitudinal and (b) transverse directions. Black (red) solid lines represent dark (bright) plasmonic modes. In the figure $d = 3a_1$.

its behavior while changing both the size and interparticle distance, independently. We are using again particular cases of the Ag-Ag homogeneous dimer and the Ag-Au heterogeneous dimer with size ratio $a_2/a_1 = 1.2$.

In Figure 3.9 we present two-dimensional maps of $\gamma_\pm^\sigma = \gamma_\pm^{\sigma,\mathrm{L}} + \gamma_\pm^{\sigma,\mathrm{r}}$ for the homogeneous Ag-Ag dimer modes as a function of the size a_1 and interparticle distance d. From panels (a) and (d) of the figure we see that the low damping regions are pushed toward greater particle sizes, as expected of the dark modes. On panels (b) and (c) we observe

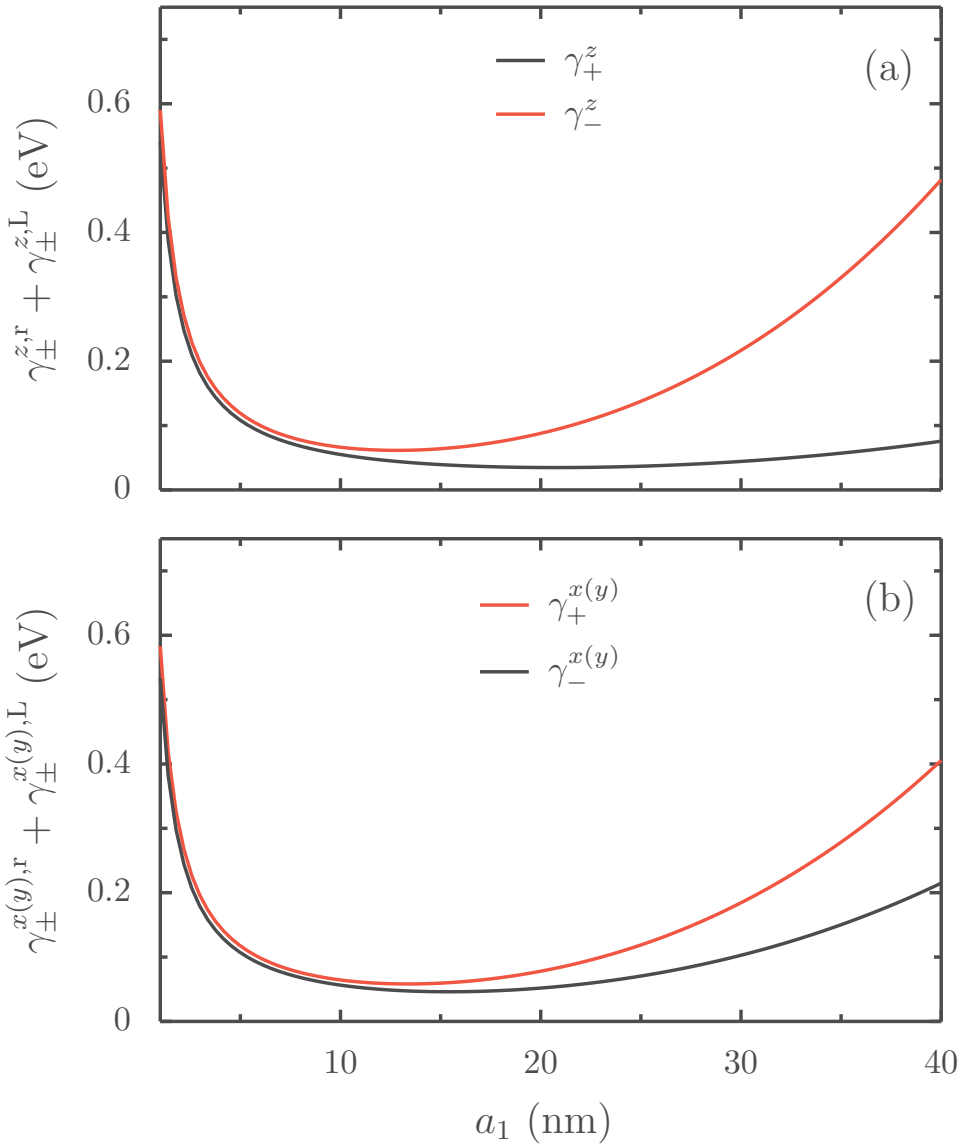

Figure 3.8: Sum of radiation and Landau damping of heterogeneous (Ag-Au) nanoparticle dimer as a function of the nanoparticle size a_1 for the (a) longitudinal and (b) transverse directions. Black (red) solid lines represent dark (bright) plasmonic modes. In the figure $a_2/a_1 = 1.2$ and $d = 3\sqrt{a_1 a_2}$.

a range of the sizes a_1 at which damping is minimal with little influence of the separation d. These regions are similar in width and span sizes in the range of $10 - 20$ nm.

Figure 3.10 presents the sum $\gamma_\pm^\sigma = \gamma_\pm^{\sigma,\mathrm{L}} + \gamma_\pm^{\sigma,\mathrm{r}}$ as a function of the size a_1 and interparticle distance d for the heterogeneous dimer Ag-Au with the fixed ratio $a_2/a_1 = 1.2$. Panels (a) and (d) of the figure show the dark modes while panels (b) and (c) present the bright modes. We see that the situation is more complex than in the case of homogeneous

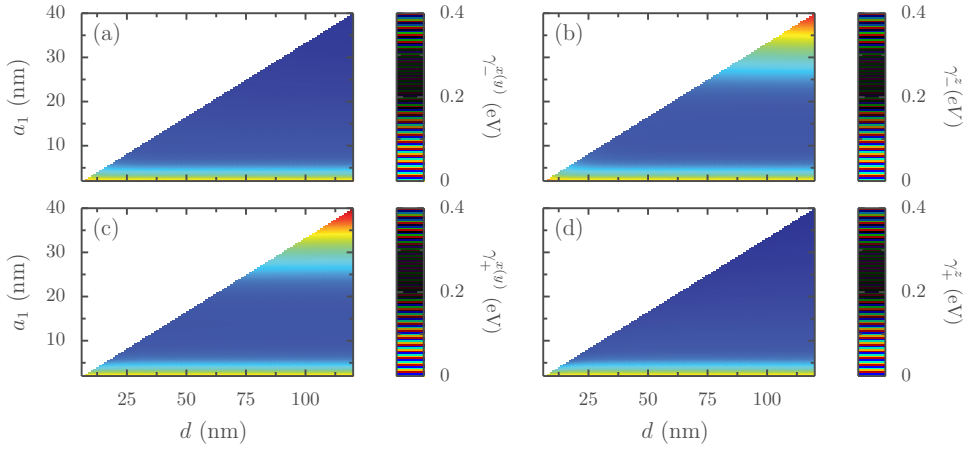

Figure 3.9: Sum of Landau and radiation damping for the homogeneous Ag-Ag nanoparticle dimer as a function of particle size a_1 and interparticle distance d. Panels (a) and (d) show dark modes while (b) and (c) show bright modes.

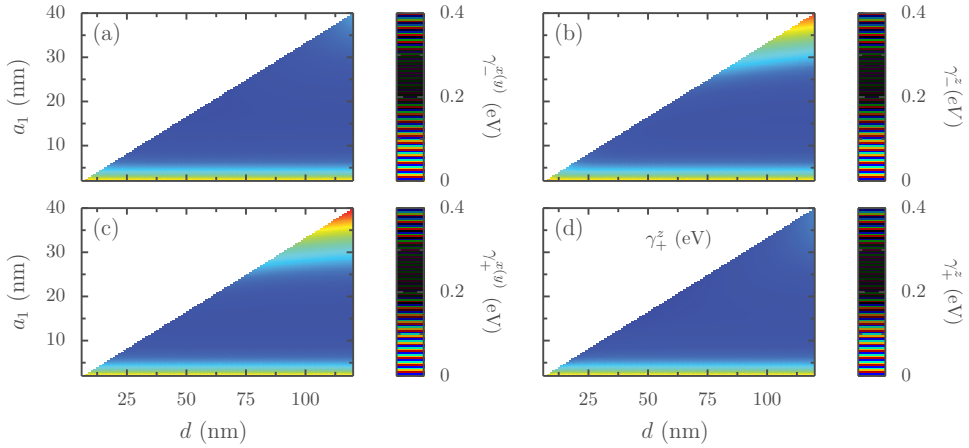

Figure 3.10: Sum of Landau and radiation damping for the heterogeneous Ag-Au nanoparticle dimer as a function of particle size a_1 and interparticle distance d. Panels (a) and (d) show dark modes while (b) and (c) show bright modes. In the figures $a_2 = 1.2a_1$.

dimer Ag-Ag.

From panel (c) of the figure we see that the range of sizes which minimize the damping is reduced as compared to Figure 3.9(c) for the Ag-Ag dimer. The opposite behavior appears for the bright mode in the longitudinal direction [compare panels (b) of Figures 3.9 and 3.10], where the sizes range spans from $10 - 25$ nm. The broadest range of sizes for minimization of the damping (i.e. $10-30$ nm) is present for the transverse dark mode (see Figure 3.10(a)). At the same time the longitudinal dark mode has a noticeably lower range (see Figure 3.10(b)), which follows from the dependence on the interparticle distance of its

Landau and radiation damping (see solid black lines in Figures 3.5(a) and 3.6(a)).

Note that in Figures 3.9 and 3.10 the white zones are regions for which the interparticle spacing is lower than allowed by our model. The borderline is determined by $d = 3\sqrt{a_1 a_2}$ which is a lower limit for the dipole-dipole interaction (for interparticle spacing below this limit, multipolar interaction might play a role [45]).

3.6 Conclusions to chapter 3

In this chapter we extended the theoretical framework of Chapter 2 for the case of nanoparticle dimers. Dimer structures are the most basic arrays, thus investigating them sets a good starting point toward further studies, such as nanoparticle chains studied in Chapter 4.

As a result of the study on the nanoparticle dimers we obtained the answers to the question: How does the interaction between plasmons influence their lifetime? We have found that the Landau damping linewidth varies with the interparticle distance having a modulation of up to 25% in the case of the longitudinal modes. The radiation damping linewidth was found to vary strongly with respect to the intrerparticle distance in the heterogeneous dimer systems. In the case of the homogeneous dimers the collective modes separate into strongly radiative bright modes (with radiation damping twice as big as the one of an isolated nanoparticle) and non-radiative dark modes.

We started with the microscopic Hamiltonian for the system of two metallic nanoparticles in the Coulomb gauge. Using the jellium approximation and separating the system into center-of-mass and relative coordinates lead us to a near-field dipole-dipole interaction between plasmons and to the coupling of plasmons to electrons and photons. We diagonalized the plasmonic part of the total Hamiltonian and obtained new collective modes, dubbed $\pm$, for all polarizations, $\hat{\sigma} = \hat{x}, \hat{y}$ and $\hat{z}$.

Using our results we analyzed the influence of various parameters on plasmon damping. We showed that there exists an optimum nanoparticle size range for which we may minimize the damping and that this range varies among different modes.

Chapter 4

Plasmon propagation in one-dimensional metallic nanoparticle assemblies

In this chapter we investigate the plasmonic properties of one-dimensional chains of nanoparticles. In Section 4.1 we present the Hamiltonian of the systems as well as the plasmonic eigenmodes of the chain. In Section 4.2 we present a derivation of the master equation for the reduced density matrix describing a plasmon evolution in the presence of electronic and photonic environments. In Section 4.3 we evaluate damping rates found in the final form of the master equation. Using the master equation we investigate the propagation of the plasmon along the chain in Section 4.4. This chapter is based on article 2 of my publication list.

4.1 Hamiltonian of the system

We consider a linear chain of $\mathcal{N}$ identical spherical metallic nanoparticles with a radius a, separated by a distance d, as sketched in Figure 4.1. Each nanoparticle can sustain a localized surface plasmon resonance which couples to the neighboring ones via quasi-static dipole-dipole interaction.

We write the full Hamiltonian of the system, extending the models presented in chapters 2 and 3 [c.f. Eqs. (2.8) and (3.10)], as

$$H = H_{\rm pl} + H_{\rm eh} + H_{\rm ph} + H_{\text{pl-eh}} + H_{\text{pl-ph}} + H_{\rm drive}, \tag{4.1}$$

where $H_{\rm pl}$ is a plasmonic Hamiltonian, $H_{\rm eh}$ corresponds to the electronic bath and $H_{\rm ph}$ is a free photon Hamiltonian. $H_{\rm pl-eh}$ describes the coupling between plasmons and electrons, while $H_{\rm pl-ph}$ corresponds to the plasmon-photon coupling. $H_{\rm drive}$ is an external driving term.

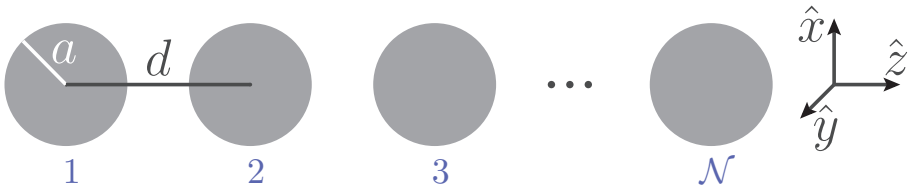

Figure 4.1: Sketch of a linear chain of $\mathcal{N}$ identical spherical metallic nanoparticles of radius a separated by a distance d of each other.

4.1.1 Plasmonic Hamiltonian

The first part of the system Hamiltonian [the first term on the right-hand-side of Eq. (4.1)] consists of the near-field coupled system of localized plasmons described by

$$H_{\rm pl} = \hbar\omega_0 \sum_{n=1}^{\mathcal{N}} \sum_{\sigma=x,y,z} b_n^{\sigma\dagger} b_n^{\sigma} + \hbar\Omega \sum_{n=1}^{\mathcal{N}-1} \sum_{\sigma=x,y,z} \eta_\sigma \left(b_n^{\sigma} + b_n^{\sigma\dagger}\right)\left(b_{n+1}^{\sigma} + b_{n+1}^{\sigma\dagger}\right) \tag{4.2}$$

with n the index identifying the particle number in the chain (see Figure 4.1). Each nanoparticle supports a dipolar plasmon with resonance frequency ω_0 which, for alkaline nanoparticles in vacuum, and neglecting the spill-out effect [1], corresponds to the Mie frequency.

Our open chain of coupled metallic nanoparticles is conveniently described using the basis

$$b_n^{\sigma} = \sqrt{\frac{2}{\mathcal{N}+1}} \sum_q \sin\left(nqd\right) b_q^{\sigma}, \tag{4.3}$$

with $q = \pi m/(\mathcal{N}+1)d$ the plasmonic momentum, where the integer $m \in [1, \mathcal{N}]$. Using Eq. (4.3), the plasmonic Hamiltonian (4.2) is expressed in momentum space, yielding yielding

$$H_{\rm pl} = \sum_{q\sigma} \left[\hbar\omega_0 + 2\eta_\sigma\hbar\Omega\cos\left(qd\right)\right] b_q^{\sigma\dagger} b_q^{\sigma} + \hbar\Omega \sum_{q\sigma} \eta_\sigma \cos\left(qd\right)\left(b_q^{\sigma\dagger} b_q^{\sigma\dagger} + b_q^{\sigma} b_q^{\sigma}\right). \tag{4.4}$$

The above Hamiltonian can be diagonalized by means of a bosonic Bogoliubov transformation. We introduce new bosonic operators expressed as a linear combination of the b_q^{σ} and $b_q^{\sigma\dagger}$ in the form

$$B_q^{\sigma} = \cosh\theta_q^{\sigma} b_q^{\sigma} + \sinh\theta_q^{\sigma} b_q^{\sigma\dagger}. \tag{4.5}$$

The above form of the new operators ensures that they satisfy bosonic commutation relations

$$\left[B_q^{\sigma}, B_{q'}^{\sigma'\dagger}\right] = \delta_{qq'}\delta_{\sigma\sigma'}, \qquad \left[B_q^{\sigma(\dagger)}, B_{q'}^{\sigma'(\dagger)}\right] = 0. \tag{4.6}$$

Inverting the transformation from Eqs. (4.5)

$$b_q^\sigma = \cosh\theta_q^\sigma B_q^\sigma - \sinh\theta_q^\sigma B_q^{\sigma\dagger}, \tag{4.7}$$

and inserting it into the plasmonic Hamiltonian (4.2) gives

$$\begin{aligned} H_{\mathrm{pl}} = \sum_{q\sigma} \big[&(\hbar\omega_0 + 2\eta_\sigma \hbar\Omega \cos qd) \cosh 2\theta_q^\sigma \\ &-2\eta_\sigma \hbar\Omega \cos qd \sinh 2\theta_q^\sigma \big] B_q^{\sigma\dagger} B_q^\sigma + \sum_{q\sigma} \Big[\eta_\sigma \hbar\Omega \cos qd \cosh 2\theta_q^\sigma \\ &-\frac{1}{2} (\hbar\omega_0 + 2\eta_\sigma \hbar\Omega \cos qd) \sinh 2\theta_q^\sigma \Big] \left(B_q^\sigma B_q^\sigma + B_q^{\sigma\dagger} B_q^{\sigma\dagger} \right). \end{aligned} \tag{4.8}$$

Imposing a diagonal form for the above Hamiltonian, we obtain the condition for the unknown coefficients θ_q^σ

$$\theta_q^\sigma = \frac{1}{2} \mathrm{atanh} \left(\frac{2\eta_\sigma \Omega \cos qd}{\omega_0 + 2\eta_\sigma \Omega \cos qd} \right). \tag{4.9}$$

Inserting Eq. (4.9) into the plasmonic Hamiltonian (4.8) yields

$$H_{\mathrm{pl}} = \sum_{\sigma=x,y,z} \sum_q \hbar\omega_q^\sigma B_q^{\sigma\dagger} B_q^\sigma, \tag{4.10}$$

where the eigenfrequencies of the collective plasmons are given by

$$\omega_q^\sigma = \omega_0 \sqrt{1 + 4\eta_\sigma \frac{\Omega}{\omega_0} \cos(qd)}. \tag{4.11}$$

Their dependence on q depicted in Figure 4.2 is in agreement with the previous theoretical work [40].

Including the far field and the associated retardation in the dipole-dipole interaction between the nanoparticles along the chain leads to only a slight quantitative modification of the dispersion relations (4.11) [46], justifying that we simply consider the near-field interaction between nearest neighbors [cf. Eq. (4.2)]. In Eq. (4.10), the bosonic operators B_q^σ and their adjoints $B_q^{\sigma\dagger}$ [cf. (4.5)] annihilate and create a collective plasmon excitation with momentum q and polarization σ along the chain, respectively. The coefficients of the Bogoliubov transformation in Eqs. (4.5) and (4.7) read

$$\cosh\theta_q^\sigma = \frac{1}{\sqrt{2}} \sqrt{\frac{1 + 2\eta_\sigma(\Omega/\omega_0)\cos(qd)}{\sqrt{1 + 4\eta_\sigma(\Omega/\omega_0)\cos(qd)}} + 1} \tag{4.12a}$$

and

$$\sinh\theta_q^\sigma = \frac{\mathrm{sgn}\{\eta_\sigma \cos(qd)\}}{\sqrt{2}} \sqrt{\frac{1 + 2\eta_\sigma(\Omega/\omega_0)\cos(qd)}{\sqrt{1 + 4\eta_\sigma(\Omega/\omega_0)\cos(qd)}} - 1}. \tag{4.12b}$$

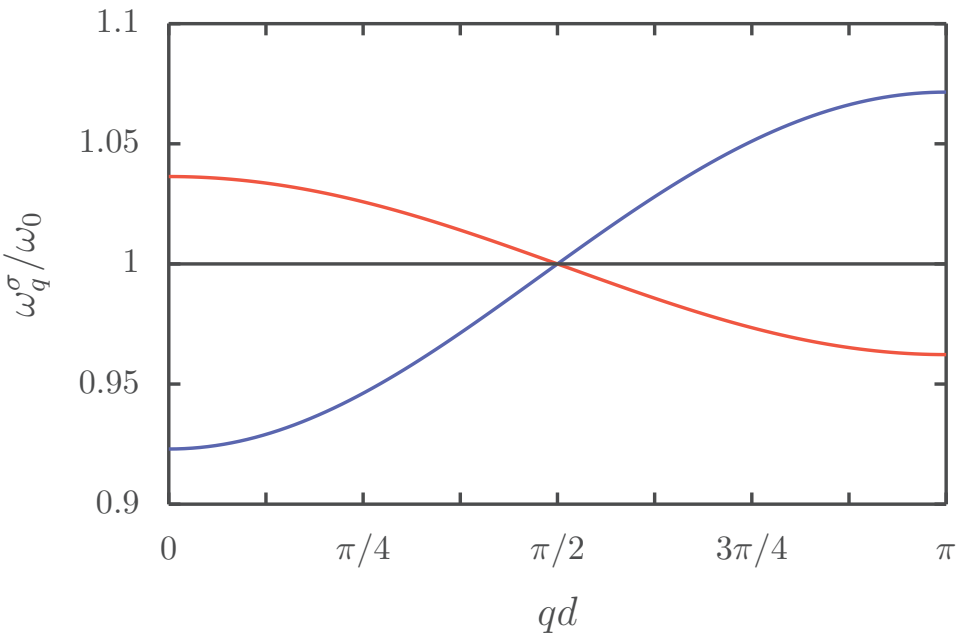

Figure 4.2: Collective plasmon dispersions (4.11) for the longitudinal (blue solid line) and transverse (dashed red line) modes. In the figure interparticle distance $d = 3a$.

4.1.2 Electronic environment

The electronic environment composed of electron-hole excitations was introduced in Chapter 2 for the special case of $\mathcal{N} = 2$ [c.f. Eq. (3.40)]. The generalization to arbitrary $\mathcal{N}$ is straightforward and gives

$$H_{\text{eh}} = \sum_{n=1}^{\mathcal{N}} \sum_{\alpha} \varepsilon_{n\alpha} c_{n\alpha}^\dagger c_{n\alpha}. \tag{4.13}$$

The coupling Hamiltonian $H_{\text{pl-eh}}$ in Eq. (4.1) reads [c.f. Eqs. (2.17) and (3.42)]

$$H_{\text{pl-eh}} = \Lambda \sum_{n=1}^{\mathcal{N}} \sum_{\sigma=x,y,z} \sum_{\alpha\beta} \left(b_n^\sigma + b_n^{\sigma\dagger} \right) \langle n\alpha|\sigma|n\beta\rangle c_{n\alpha}^\dagger c_{n\beta}, \tag{4.14}$$

with $\Lambda = \sqrt{\hbar m_{\text{e}} \omega_0^3 / 2N_{\text{e}}}$. The coupling Hamiltonian (4.14) is responsible for Landau damping of the collective plasmons.

4.1.3 Photonic environment

The photonic environment was introduced in Chapter 2 in Eq. (2.23). The plasmon-photon coupling in Eq. (4.1) takes the form [91] [c.f. Eq. (3.15)]

$$H_{\text{pl-ph}} = \frac{e}{m_{\text{e}}} \sum_{n=1}^{\mathcal{N}} \mathbf{P}_n \cdot \mathbf{A}(\mathbf{d}_n). \tag{4.15}$$

Here

$$\mathbf{P}_n = \mathrm{i}\sqrt{\frac{N_\mathrm{e} m_\mathrm{e} \hbar \omega_0}{2}} \sum_{\sigma=x,y,z} \hat{\sigma} \left(b_n^{\sigma\dagger} - b_n^{\sigma} \right) \tag{4.16}$$

is the momentum associated with the plasmon on nanoparticle n, and the vector potential $\mathbf{A}(\mathbf{d}_n)$ introduced in Chapter 2 [c.f. Eq. (2.24)], is evaluated at the position of the center of the n-th nanoparticle $\mathbf{d}_n = \hat{z}(n-1)d$. Together Eqs. (4.16) and (2.24), yield the plasmon-photon coupling (4.15) which takes the form [c.f. Eq. (3.56)]

$$H_\text{pl-ph} = \mathrm{i}\hbar \sum_{n=1}^{\mathcal{N}} \sum_{\sigma=x,y,z} \sum_{\mathbf{k},\hat{\lambda}_\mathbf{k}} \sqrt{\frac{\pi \omega_0^3 a^3}{\mathcal{V}\omega_\mathbf{k}}} \hat{\sigma} \cdot \hat{\lambda}_\mathbf{k} \left(b_n^{\sigma\dagger} - b_n^{\sigma} \right) \times \left(a_{\mathbf{k}\hat{\lambda}_\mathbf{k}} \mathrm{e}^{\mathrm{i}\mathbf{k}\cdot\mathbf{d}_n} + a^\dagger_{\mathbf{k}\hat{\lambda}_\mathbf{k}} \mathrm{e}^{-\mathrm{i}\mathbf{k}\cdot\mathbf{d}_n} \right). \tag{4.17}$$

4.1.4 Driving force

The last term of the full system Hamiltonian (4.1) is a driving term representing an electric field with a wavelength much larger than the nanoparticle size, acting on the first nanoparticle in the chain. It reads

$$H_\text{drive} = \hbar \Omega_\mathrm{R} f(t) \sum_{\sigma=x,y,z} \left(b_1^{\sigma} + b_1^{\sigma\dagger} \right) \hat{\sigma} \cdot \hat{\epsilon} \tag{4.18}$$

with $\Omega_\mathrm{R} = eE_0\sqrt{N_\mathrm{e}/2m_\mathrm{e}\hbar\omega_0}$ the Rabi frequency, where E_0 is the amplitude of the electric field, and $\hat{\epsilon}$ its polarization. In Sec. 4.4 we will consider two scenarios: First the case of a monochromatic electric field $f(t) = \sin(\omega_\mathrm{d} t)$ with ω_d the driving frequency. Second the case of extremely short laser pulse, modeled by $f(t) = \delta(\omega_0 t)$.

4.2 Reduced density matrix

The dynamics of the system is most conveniently described in terms of the reduced density matrix ρ^σ of the collective plasmonic degrees of freedom with polarization σ.

The evolution of the subsystem with polarization $\hat{\sigma}$ is given by the equation of motion

$$\dot{\rho}^\sigma_\text{tot}(t) = -\frac{\mathrm{i}}{\hbar} \left[H^\sigma + H_\text{eh} + H_\text{ph}, \rho^\sigma_\text{tot}(t) \right], \tag{4.19}$$

with ρ^σ_tot being a density matrix of the plasmonic subsystem together with the baths, and where H^σ reads

$$H^\sigma = H^\sigma_\text{pl} + H^\sigma_\text{pl-eh} + H_\text{pl-ph}, \tag{4.20}$$

with

$$H_{\rm pl}^{\sigma} = \sum_{q} \hbar\omega_q^{\sigma} B_q^{\sigma\dagger} B_q^{\sigma}, \tag{4.21}$$

$$H_{\text{pl-eh}}^{\sigma} = \Lambda \sum_{n=1}^{\mathcal{N}} \sum_{\alpha\beta} \left(b_n^{\sigma} + b_n^{\sigma\dagger}\right) \langle n\alpha|\sigma|n\beta\rangle c_{n\alpha}^{\dagger} c_{n\beta}, \tag{4.22}$$

$$H_{\rm pl-ph}^{\sigma} = \mathrm{i}\hbar \sum_{n=1}^{\mathcal{N}} \sum_{\mathbf{k},\hat{\lambda}_{\mathbf{k}}} \sqrt{\frac{\pi\omega_0^3 a^3}{\mathcal{V}\omega_{\mathbf{k}}}} \hat{\sigma}\cdot\hat{\lambda}_{\mathbf{k}} \left(b_n^{\sigma\dagger} - b_n^{\sigma}\right)$$
$$\times \left(a_{\mathbf{k}\hat{\lambda}_{\mathbf{k}}} \mathrm{e}^{\mathrm{i}\mathbf{k}\cdot\mathbf{d}_n} + a_{\mathbf{k}\hat{\lambda}_{\mathbf{k}}}^{\dagger} \mathrm{e}^{-\mathrm{i}\mathbf{k}\cdot\mathbf{d}_n}\right). \tag{4.23}$$

Assuming that the driving field does not affect the coupling of plasmons to the electronic and photonic environments we omit it for the time being (i.e. $H_{\rm drive} = 0$). We write Eq. (4.19) in the interaction picture as

$$\dot{\tilde{\rho}}_{\rm tot}^{\sigma}(t) = -\frac{\mathrm{i}}{\hbar}\left[\tilde{H}_{\rm pl-eh}^{\sigma}(t) + \tilde{H}_{\rm pl-ph}^{\sigma}(t), \tilde{\rho}_{\rm tot}^{\sigma}(t)\right], \tag{4.24}$$

with

$$\tilde{\rho}_{\rm tot}^{\sigma}(t) = e^{\mathrm{i}H_0 t/\hbar} \rho_{\rm tot}^{\sigma}(t) e^{-\mathrm{i}H_0 t/\hbar}, \tag{4.25}$$

and

$$\tilde{H}_{\rm pl-eh}^{\sigma}(t) = e^{\mathrm{i}H_0 t/\hbar} H_{\rm pl-eh}^{\sigma} e^{-\mathrm{i}H_0 t/\hbar}, \tag{4.26}$$
$$\tilde{H}_{\rm pl-ph}^{\sigma}(t) = e^{\mathrm{i}H_0 t/\hbar} H_{\rm pl-ph}^{\sigma} e^{-\mathrm{i}H_0 t/\hbar}, \tag{4.27}$$

where $H_0 = H_{\rm pl} + H_{\rm eh} + H_{\rm ph}$. Integrating Eq. (4.24) and inserting the result back in (4.24) yields the integro-differential equation

$$\tilde{\rho}_{\rm tot}^{\sigma}(t) = -\frac{\mathrm{i}}{\hbar}\left[\tilde{H}_{\rm pl-eh}^{\sigma}(t) + \tilde{H}_{\rm pl-ph}^{\sigma}(t), \tilde{\rho}_{\rm tot}^{\sigma}(0)\right]$$
$$-\frac{1}{\hbar^2}\int_0^t \mathrm{d}s \left[\tilde{H}_{\rm pl-eh}^{\sigma}(t) + \tilde{H}_{\rm pl-ph}^{\sigma}(t), \left[\tilde{H}_{\rm pl-eh}^{\sigma}(s) + \tilde{H}_{\rm pl-ph}^{\sigma}(s), \tilde{\rho}_{\rm tot}^{\sigma}(s)\right]\right], \tag{4.28}$$

and tracing out electronic and photonic degrees of freedom gives

$$\tilde{\rho}^{\sigma}(t) = -\frac{\mathrm{i}}{\hbar}\mathrm{Tr}_{\rm eh}\mathrm{Tr}_{\rm ph}\left[\tilde{H}_{\rm pl-eh}^{\sigma}(t) + \tilde{H}_{\rm pl-ph}^{\sigma}(t), \tilde{\rho}_{\rm tot}^{\sigma}(0)\right] - \frac{1}{\hbar^2}\int_0^t \mathrm{d}s$$
$$\times \mathrm{Tr}_{\rm eh}\mathrm{Tr}_{\rm ph}\left[\tilde{H}_{\rm pl-eh}^{\sigma}(t) + \tilde{H}_{\rm pl-ph}^{\sigma}(t), \left[\tilde{H}_{\rm pl-eh}^{\sigma}(s) + \tilde{H}_{\rm pl-ph}^{\sigma}(s), \tilde{\rho}_{\rm tot}^{\sigma}(s)\right]\right]. \tag{4.29}$$

A usual approximation at this point is to assume the weak coupling regime [91]: The perturbations $H_{\rm pl-eh}$ and $H_{\rm pl-ph}$ do not change significantly the electronic and photonic environments respectively. Thus,

both electronic and photonic baths stay in thermal equilibrium during the time evolution of the plasmonic system. Moreover, assuming that correlations between plasmons and environments may be neglected on the timescales at which we consider the evolution of the system, we may write

$$\rho^{\sigma}_{\mathrm{tot}}(t) \approx \rho^{\sigma}(t) \otimes \rho_{\mathrm{eh}} \otimes \rho_{\mathrm{ph}}, \tag{4.30}$$

where ρ_{eh} (ρ_{ph}) is density matrix of the electronic (photonic) environment.

Inserting Eq. (4.30) into the first term of the right-hand-side of Eq. (4.28) with the use of Eqs. (4.14) and (4.17) we have

$$\begin{aligned}
&\mathrm{Tr}_{\mathrm{eh}}\mathrm{Tr}_{\mathrm{ph}}\left[\tilde{H}^{\sigma}_{\mathrm{pl-eh}}(t) + \tilde{H}^{\sigma}_{\mathrm{pl-ph}}(t), \rho^{\sigma}(0) \otimes \rho_{\mathrm{eh}} \otimes \rho_{\mathrm{ph}}\right] = \\
&\sum_{n=1}^{\mathcal{N}} \sum_{\sigma=x,y,z} \left[b^{\sigma\dagger}_{n}(t) - b^{\sigma}_{n}(t), \rho^{\sigma}(0)\right] \Bigg[\sum_{\alpha\beta} \Lambda \langle n\alpha|\sigma|n\beta\rangle \mathrm{Tr}_{\mathrm{eh}}\left\{\rho_{\mathrm{eh}} c^{\dagger}_{n\alpha}(t) c_{n\beta}(t)\right\} \\
&+ \sum_{\mathbf{k},\hat{\lambda}_{\mathbf{k}}} \sqrt{\frac{\pi\omega_0^3 a^3}{\mathcal{V}\omega_{\mathbf{k}}}} \hat{\sigma}\cdot\hat{\lambda}_{\mathbf{k}} \mathrm{Tr}_{\mathrm{ph}}\left\{\rho_{\mathrm{ph}}\left(a_{\mathbf{k}\hat{\lambda}_{\mathbf{k}}}(t)\mathrm{e}^{\mathrm{i}\mathbf{k}\cdot\mathbf{d}_n} + a^{\dagger}_{\mathbf{k}\hat{\lambda}_{\mathbf{k}}}(t)\mathrm{e}^{-\mathrm{i}\mathbf{k}\cdot\mathbf{d}_n}\right)\right\}\Bigg] = 0,
\end{aligned} \tag{4.31}$$

where the first term of the squared bracket vanishes due to the non-diagonal form of dipole moment matrix elements (i.e. $\langle n\alpha|\sigma|n\alpha\rangle = 0$) and the second vanishes due to identity $\mathrm{Tr}_{\mathrm{ph}}(\rho_{\mathrm{ph}} a_{\mathbf{k}\hat{\lambda}_{\mathbf{k}}}) = 0$. We therefore arrive at the equation of motion for the reduced density matrix in the form

$$\begin{aligned}
\dot{\tilde{\rho}}^{\sigma}(t) \simeq &-\frac{1}{\hbar^2}\int_0^t \mathrm{d}s\, \mathrm{Tr}_{\mathrm{eh}}\mathrm{Tr}_{\mathrm{ph}} \\
\times &\left[\tilde{H}^{\sigma}_{\mathrm{pl-eh}}(t) + \tilde{H}^{\sigma}_{\mathrm{pl-ph}}(t), \left[\tilde{H}^{\sigma}_{\mathrm{pl-eh}}(s) + \tilde{H}^{\sigma}_{\mathrm{pl-ph}}(s), \tilde{\rho}^{\sigma}(s) \otimes \rho_{\mathrm{eh}} \otimes \rho_{\mathrm{ph}}\right]\right].
\end{aligned} \tag{4.32}$$

Using Eq. (4.31) we may simplify the above equation to

$$\begin{aligned}
\dot{\tilde{\rho}}^{\sigma}(t) \simeq &-\frac{1}{\hbar^2}\int_0^t \mathrm{d}s\, \mathrm{Tr}_{\mathrm{eh}}\left[\tilde{H}^{\sigma}_{\mathrm{pl-eh}}(t), \left[\tilde{H}^{\sigma}_{\mathrm{pl-eh}}(s), \tilde{\rho}^{\sigma}(s) \otimes \rho_{\mathrm{eh}}\right]\right] \\
&-\frac{1}{\hbar^2}\int_0^t \mathrm{d}s\, \mathrm{Tr}_{\mathrm{ph}}\left[\tilde{H}^{\sigma}_{\mathrm{pl-ph}}(t), \left[\tilde{H}^{\sigma}_{\mathrm{pl-ph}}(s), \tilde{\rho}^{\sigma}(s) \otimes \rho_{\mathrm{ph}}\right]\right].
\end{aligned} \tag{4.33}$$

We now turn to the evaluation of the traces in the above equation starting with trace over electrons. Inserting the expression for the

coupling (3.14) we get

$$\mathrm{Tr}_{\mathrm{eh}}\left[\tilde{H}^{\sigma}_{\mathrm{pl-eh}}(t),\left[\tilde{H}^{\sigma}_{\mathrm{pl-eh}}(s),\tilde{\rho}^{\sigma}(s)\otimes\rho_{\mathrm{eh}}\right]\right]=\sum_{n=1}^{\mathcal{N}}\sum_{n'=1}^{\mathcal{N}}\sum_{\alpha\beta\alpha'\beta'}\Lambda^2$$
$$\times\langle n\alpha|\sigma|n\beta\rangle\langle n'\alpha'|\sigma|n'\beta'\rangle\mathrm{Tr}_{\mathrm{eh}}\left[(b^{\sigma}_{n}(t)+b^{\sigma\dagger}_{n}(t))c^{\dagger}_{n\alpha}(t)c_{n\beta}(t),\right.$$
$$\left.\times\left[(b^{\sigma}_{n'}(s)+b^{\sigma\dagger}_{n'}(s))c^{\dagger}_{n'\alpha'}(s)c_{n'\beta'}(s),\tilde{\rho}^{\sigma}(s)\otimes\rho_{\mathrm{eh}}\right]\right], \tag{4.34}$$

or by expressing the plasmonic annihilation and creation operators b^{σ}_{n} and $b^{\sigma\dagger}_{n}$ by the normal mode ones (4.5)

$$b^{\sigma}_{n}=\sqrt{\frac{2}{\mathcal{N}+1}}\sum_{q}\sin(qdn)(\cosh\theta^{\sigma}_{q}B^{\sigma}_{q}-\sinh\theta^{\sigma}_{q}B^{\sigma\dagger}_{q}), \tag{4.35}$$

we may write

$$\mathrm{Tr}_{\mathrm{eh}}\left[\tilde{H}^{\sigma}_{\mathrm{pl-eh}}(t),\left[\tilde{H}^{\sigma}_{\mathrm{pl-eh}}(s),\tilde{\rho}^{\sigma}(s)\otimes\rho_{\mathrm{eh}}\right]\right]=\frac{2}{\mathcal{N}+1}\sum_{n=1}^{\mathcal{N}}\sum_{n'=1}^{\mathcal{N}}\sum_{qq'}\sum_{\alpha\beta\alpha'\beta'}$$
$$\times\Lambda^2\langle n\alpha|\sigma|n\beta\rangle\langle n'\alpha'|\sigma|n'\beta'\rangle(\cosh\theta^{\sigma}_{q}-\sinh\theta^{\sigma}_{q})(\cosh\theta^{\sigma}_{q'}-\sinh\theta^{\sigma}_{q'})$$
$$\times\sin(qdn)\sin(q'dn')\mathrm{Tr}_{\mathrm{eh}}\left[\left(B^{\sigma}_{q}(t)+B^{\sigma\dagger}_{q}(t)\right)c^{\dagger}_{n\alpha}(t)c_{n\beta}(t),\right.$$
$$\left.\times\left[\left(B^{\sigma}_{q'}(s)+B^{\sigma\dagger}_{q'}(s)\right)c^{\dagger}_{n'\alpha'}(s)c_{n'\beta'}(s),\tilde{\rho}^{\sigma}(s)\otimes\rho_{\mathrm{eh}}\right]\right]. \tag{4.36}$$

Putting the explicit time dependence of the annihilation and creation operators into the above equation with the use of the relation

$$\dot{\tilde{\mathcal{O}}}(t)=\frac{\mathrm{i}}{\hbar}e^{\mathrm{i}H_0t/\hbar}\left[H_0,\mathcal{O}\right]e^{-\mathrm{i}H_0t/\hbar}, \tag{4.37}$$

for any operator $\mathcal{O}$, we get

$$B^{\sigma}_{q}(t)=B^{\sigma}_{q}e^{-\mathrm{i}\omega^{\sigma}_{q}t}, \tag{4.38}$$

for the collective plasmons and

$$c_{n\alpha}(t)=c_{n\alpha}e^{-\mathrm{i}\omega_{\alpha}t}, \tag{4.39}$$

for the electrons and where $\omega_{\alpha}=\varepsilon_{\alpha}/\hbar$ and

$$a_{\mathbf{k}\hat{\lambda}_{\mathbf{k}}}(t)=a_{\mathbf{k}\hat{\lambda}_{\mathbf{k}}}e^{-\mathrm{i}\omega_{\mathbf{k}}t}, \tag{4.40}$$

for the photons. Inserting Eq. (4.39) into the trace (4.36) we get

$$\mathrm{Tr}_{\mathrm{eh}}\left[\tilde{H}^{\sigma}_{\mathrm{pl-eh}}(t),\left[\tilde{H}^{\sigma}_{\mathrm{pl-eh}}(s),\tilde{\rho}(s)\otimes\rho_{\mathrm{eh}}\right]\right]=\frac{2}{\mathcal{N}+1}\sum_{n=1}^{\mathcal{N}}\sum_{n'=1}^{\mathcal{N}'}\sum_{qq'}\sum_{\alpha\beta\alpha'\beta'}$$
$$\times\Lambda^2\sin(qdn)\sin(q'dn')\langle n\alpha|\sigma|n\beta\rangle\langle n'\alpha'|\sigma|n'\beta'\rangle$$
$$\times(\cosh\theta^{\sigma}_{q}-\sinh\theta^{\sigma}_{q})(\cosh\theta^{\sigma}_{q'}-\sinh\theta^{\sigma}_{q'})e^{\mathrm{i}(\omega_{\alpha}-\omega_{\beta})t}e^{\mathrm{i}(\omega_{\alpha'}-\omega_{\beta'})s}$$
$$\times\mathrm{Tr}_{\mathrm{eh}}\left[\left(B^{\sigma}_{q}(t)+B^{\sigma\dagger}_{q}(t)\right)c^{\dagger}_{n\alpha}c_{n\beta},\left[\left(B^{\sigma}_{q'}(s)+B^{\sigma\dagger}_{q'}(s)\right)\right.\right.$$
$$\left.\left.\times\ c^{\dagger}_{n'\alpha'}c_{n'\beta'},\tilde{\rho}^{\sigma}(s)\otimes\rho_{\mathrm{eh}}\right]\right]. \tag{4.41}$$

The last term of the right-hand-side of the above equation yields

$$\begin{aligned}
&\mathrm{Tr}_{\mathrm{eh}}\left[\left(B_q^{\sigma}(t)+B_q^{\sigma\dagger}(t)\right)c_{n\alpha}^{\dagger}c_{n\beta},\left[\left(B_{q'}^{\sigma}(s)+B_{q'}^{\sigma\dagger}(s)\right)c_{n'\alpha'}^{\dagger}c_{n'\beta'},\tilde{\rho}^{\sigma}(s)\otimes\rho_{\mathrm{eh}}\right]\right]\\
&=\left[B_q^{\sigma}(t)+B_q^{\sigma\dagger}(t),\left(B_{q'}^{\sigma}(s)+B_{q'}^{\sigma\dagger}(s)\right)\tilde{\rho}^{\sigma}(s)\right]\mathrm{Tr}_{\mathrm{eh}}\left\{\rho_{\mathrm{eh}}c_{n\alpha}^{\dagger}c_{n\beta}c_{n'\alpha'}^{\dagger}c_{n'\beta'}\right\}\\
&-\left[B_q^{\sigma}(t)+B_q^{\sigma\dagger}(t),\tilde{\rho}^{\sigma}(s)\left(B_{q'}^{\sigma}(s)+B_{q'}^{\sigma\dagger}(s)\right)\right]\mathrm{Tr}_{\mathrm{eh}}\left\{\rho_{\mathrm{eh}}c_{n'\alpha'}^{\dagger}c_{n'\beta'}c_{n\alpha}^{\dagger}c_{n\beta}\right\},
\end{aligned}\tag{4.42}$$

where the traces over electronic degrees of freedom leads to

$$\begin{aligned}
\mathrm{Tr}_{\mathrm{eh}}\left\{\rho_{\mathrm{eh}}c_{n'\alpha'}^{\dagger}c_{n'\beta'}c_{n\alpha}^{\dagger}c_{n\beta}\right\}=&\delta_{\alpha'\beta'}\delta_{\alpha\beta}f(\varepsilon_{\alpha'})f(\varepsilon_{\alpha})+\delta_{nn'}\delta_{\alpha'\beta}\delta_{\alpha\beta'}\\
&\times[1-f(\varepsilon_{\alpha})]f(\varepsilon_{\alpha'}),
\end{aligned}\tag{4.43}$$

where $f(\varepsilon)=1/(\exp[(\varepsilon-E_{\mathrm{F}})/k_{\mathrm{B}}T]+1)$ is the Fermi-Dirac distribution, with k_{B} being the Boltzmann constant and T temperature. With the use of $\langle n\alpha|\sigma|n\beta\rangle=\hat{\sigma}\cdot\mathbf{d}_{\alpha\beta}$ and the fact that $\mathbf{d}_{\alpha\alpha}=0$ we may write Eq. (4.41) as

$$\begin{aligned}
&\mathrm{Tr}_{\mathrm{eh}}\left[\tilde{H}_{\mathrm{pl-eh}}(t),\left[\tilde{H}_{\mathrm{pl-eh}}(s),\tilde{\rho}^{\sigma}(s)\otimes\rho_{\mathrm{eh}}\right]\right]=\\
&\sum_q\left\{\mathcal{C}_q^{\sigma}(s-t)\left[B_q^{\sigma}(t)+B_q^{\sigma\dagger}(t),\left(B_q^{\sigma}(s)+B_q^{\sigma\dagger}(s)\right)\tilde{\rho}^{\sigma}(s)\right]\right.\\
&\qquad\left.-\mathcal{C}_q^{\sigma}(t-s)\left[B_q^{\sigma}(t)+B_q^{\sigma\dagger}(t),\tilde{\rho}^{\sigma}(s)\left(B_q^{\sigma}(s)+B_q^{\sigma\dagger}(s)\right)\right]\right\},
\end{aligned}\tag{4.44}$$

where the correlation function $\mathcal{C}_q^{\sigma}(\tau)$ is defined as

$$\mathcal{C}_q^{\sigma}(\tau)=\sum_{\alpha\beta}\Lambda^2(\cosh\theta_q^{\sigma}-\sinh\theta_q^{\sigma})^2|\hat{\sigma}\cdot\mathbf{d}_{\alpha\beta}|^2f(\varepsilon_{\beta})[1-f(\varepsilon_{\alpha})]e^{\mathrm{i}(\omega_{\alpha}-\omega_{\beta})\tau}.\tag{4.45}$$

Following a similar derivation [c.f. Eqs. (4.34) – (4.36)] for the second term of the right-hand-side of Eq. (4.33) we get

$$\begin{aligned}
&\mathrm{Tr}_{\mathrm{ph}}\left[\tilde{H}_{\mathrm{pl-ph}}^{\sigma}(t),\left[\tilde{H}_{\mathrm{pl-ph}}^{\sigma}(s),\tilde{\rho}^{\sigma}(s)\otimes\rho_{\mathrm{ph}}\right]\right]=\frac{-2}{\mathcal{N}+1}\sum_{n=1}^{\mathcal{N}}\sum_{n'=1}^{\mathcal{N}}\sum_{qq'}\sum_{\mathbf{k}\mathbf{k}'\hat{\lambda}_{\mathbf{k}}\hat{\lambda}'_{\mathbf{k}'}}\\
&\times\frac{\hbar^2\pi\omega_0^3a^3}{\sqrt{\mathcal{V}\mathcal{V}'\omega_{\mathbf{k}}\omega_{\mathbf{k}'}}}\sin(qdn)\sin(q'dn')(\cosh\theta_q^{\sigma}+\sinh\theta_q^{\sigma})(\cosh\theta_{q'}^{\sigma}+\sinh\theta_{q'}^{\sigma})\\
&\times(\hat{\sigma}\cdot\hat{\lambda}_{\mathbf{k}})(\hat{\sigma}\cdot\hat{\lambda}'_{\mathbf{k}'})\mathrm{Tr}_{\mathrm{ph}}\left[\left(B_q^{\sigma\dagger}(t)-B_q^{\sigma}(t)\right)\left(a_{\mathbf{k}\hat{\lambda}_{\mathbf{k}}}e^{\mathrm{i}\mathbf{k}\cdot\mathbf{d}_n}+a_{\mathbf{k}\hat{\lambda}_{\mathbf{k}}}^{\dagger}e^{-\mathrm{i}\mathbf{k}\cdot\mathbf{d}_n}\right),\right.\\
&\times\left.\left[\left(B_{q'}^{\sigma\dagger}(s)-B_{q'}^{\sigma}(s)\right)\left(a_{\mathbf{k}'\hat{\lambda}_{\mathbf{k}'}}e^{\mathrm{i}\mathbf{k}'\cdot\mathbf{d}_{n'}}+a_{\mathbf{k}'\hat{\lambda}_{\mathbf{k}'}}^{\dagger}e^{-\mathrm{i}\mathbf{k}'\cdot\mathbf{d}_{n'}}\right),\tilde{\rho}^{\sigma}(s)\otimes\rho_{\mathrm{ph}}\right]\right].
\end{aligned}\tag{4.46}$$

We introduce the array factor defined as

$$F_{\mathbf{k},q}=\sqrt{\frac{2}{\mathcal{N}+1}}\sum_{n=1}^{\mathcal{N}}\sin(nqd)\,\mathrm{e}^{-\mathrm{i}\mathbf{k}\cdot\mathbf{d}_n},\tag{4.47}$$

which is straightforwardly evaluated to yield

$$F_{\mathbf{k},q} = \frac{\mathrm{i}\,\mathrm{e}^{\mathrm{i}k_z d}}{\sqrt{2(\mathcal{N}+1)}} \sum_{\kappa=\pm} \kappa\ \mathrm{e}^{-\mathrm{i}\kappa(\mathcal{N}+1)(q+\kappa k_z)d/2} \frac{\sin\left(\mathcal{N}[q+\kappa k_z]d/2\right)}{\sin\left([q+\kappa k_z]d/2\right)} \tag{4.48}$$

with k_z the z component of the photon momentum $\mathbf{k}$. With the help of Eq. (4.47) we rewrite Eq. (4.46) as

$$\begin{aligned}
\mathrm{Tr}_{\mathrm{ph}}\left[\tilde{H}^{\sigma}_{\mathrm{pl-ph}}(t), \left[\tilde{H}^{\sigma}_{\mathrm{pl-ph}}(s), \tilde{\rho}^{\sigma}(s)\otimes\rho_{\mathrm{ph}}\right]\right] &= -\sum_{qq'}\sum_{\mathbf{k}\mathbf{k}'\hat{\lambda}_{\mathbf{k}}\hat{\lambda}'_{\mathbf{k}'}} \\
&\times \frac{\hbar^2\pi\omega_0^3 a^3}{\sqrt{\mathcal{V}\mathcal{V}'\omega_{\mathbf{k}}\omega_{\mathbf{k}'}}} (\cosh\theta^{\sigma}_q + \sinh\theta^{\sigma}_q)(\cosh\theta^{\sigma}_{q'} + \sinh\theta^{\sigma}_{q'}) \\
&\times (\hat{\sigma}\cdot\hat{\lambda}_{\mathbf{k}})(\hat{\sigma}\cdot\hat{\lambda}'_{\mathbf{k}'})\mathrm{Tr}_{\mathrm{ph}}\left[\left(B^{\sigma\dagger}_q(t) - B^{\sigma}_q(t)\right)\left(a_{\mathbf{k}\hat{\lambda}_{\mathbf{k}}}F^{*}_{\mathbf{k},q} + a^{\dagger}_{\mathbf{k}\hat{\lambda}_{\mathbf{k}}}F_{\mathbf{k},q}\right),\right. \\
&\times \left.\left[\left(B^{\sigma\dagger}_{q'}(s) + B^{\sigma}_{q'}(s)\right)\left(a_{\mathbf{k}'\hat{\lambda}_{\mathbf{k}'}}F^{*}_{\mathbf{k}',q'} + a^{\dagger}_{\mathbf{k}'\hat{\lambda}_{\mathbf{k}'}}F_{\mathbf{k}',q'}\right), \tilde{\rho}^{\sigma}(s)\otimes\rho_{\mathrm{ph}}\right]\right],
\end{aligned} \tag{4.49}$$

where the trace over photon degrees of freedom gives

$$\begin{aligned}
&\mathrm{Tr}_{\mathrm{ph}}\left[\left(B^{\sigma\dagger}_q(t) - B^{\sigma}_q(t)\right)\left(a_{\mathbf{k}\hat{\lambda}_{\mathbf{k}}}F^{*}_{\mathbf{k},q} + a^{\dagger}_{\mathbf{k}\hat{\lambda}_{\mathbf{k}}}F_{\mathbf{k},q}\right), \left[\left(B^{\sigma\dagger}_{q'}(s) + B^{\sigma}_{q'}(s)\right)\right.\right. \\
&\times \left.\left.\left(a_{\mathbf{k}'\hat{\lambda}_{\mathbf{k}'}}F^{*}_{\mathbf{k}',q'} + a^{\dagger}_{\mathbf{k}'\hat{\lambda}_{\mathbf{k}'}}F_{\mathbf{k}',q'}\right), \tilde{\rho}^{\sigma}(s)\otimes\rho_{\mathrm{ph}}\right]\right], \\
&= \left[B^{\sigma\dagger}_q(t) - B^{\sigma}_q(t), \left(B^{\sigma\dagger}_{q'}(s) - B^{\sigma}_{q'}(s)\right)\tilde{\rho}^{\sigma}(s)\right] \qquad (4.50) \\
&\times \mathrm{Tr}_{\mathrm{ph}}\left\{\rho_{\mathrm{ph}}\left(a_{\mathbf{k}\hat{\lambda}_{\mathbf{k}}}F^{*}_{\mathbf{k},q} + a^{\dagger}_{\mathbf{k}\hat{\lambda}_{\mathbf{k}}}F_{\mathbf{k},q}\right)\left(a_{\mathbf{k}'\hat{\lambda}_{\mathbf{k}'}}F^{*}_{\mathbf{k}',q'} + a^{\dagger}_{\mathbf{k}'\hat{\lambda}_{\mathbf{k}'}}F_{\mathbf{k}',q'}\right)\right\} \\
&- \left[B^{\sigma}_q(t) + B^{\sigma\dagger}_q(t), \tilde{\rho}^{\sigma}(s)\left(B^{\sigma}_{q'}(s) + B^{\sigma\dagger}_{q'}(s)\right)\right] \qquad (4.51) \\
&\times \mathrm{Tr}_{\mathrm{ph}}\left\{\rho_{\mathrm{ph}}\left(a_{\mathbf{k}'\hat{\lambda}_{\mathbf{k}'}}F^{*}_{\mathbf{k}',q'} + a^{\dagger}_{\mathbf{k}'\hat{\lambda}_{\mathbf{k}'}}F_{\mathbf{k}',q'}\right)\left(a_{\mathbf{k}\hat{\lambda}_{\mathbf{k}}}F^{*}_{\mathbf{k},q} + a^{\dagger}_{\mathbf{k}\hat{\lambda}_{\mathbf{k}}}F_{\mathbf{k},q}\right)\right\}.
\end{aligned}$$

In the above equation the trace over photons yields

$$\begin{aligned}
&\mathrm{Tr}_{\mathrm{ph}}\left\{\rho_{\mathrm{ph}}\left(a_{\mathbf{k}\hat{\lambda}_{\mathbf{k}}}F^{*}_{\mathbf{k},q} + a^{\dagger}_{\mathbf{k}\hat{\lambda}_{\mathbf{k}}}F_{\mathbf{k},q}\right)\left(a_{\mathbf{k}'\hat{\lambda}_{\mathbf{k}'}}F^{*}_{\mathbf{k}',q'} + a^{\dagger}_{\mathbf{k}'\hat{\lambda}_{\mathbf{k}'}}F_{\mathbf{k}',q'}\right)\right\} \\
&\quad = \delta_{\mathbf{k}\mathbf{k}'}\left[\left(1 - n_{\mathrm{ph}}(\omega_{\mathbf{k}})\right)F^{*}_{\mathbf{k},q}F_{\mathbf{k},q'} + n_{\mathrm{ph}}(\omega_{\mathbf{k}})F_{\mathbf{k},q}F^{*}_{\mathbf{k},q'}\right]
\end{aligned} \tag{4.52}$$

where $n_{\mathrm{ph}}(\omega) = 1/(\exp[\hbar\omega/k_{\mathrm{B}}T] - 1)$ is the Bose-Einstein distribution for the photons. In the large chain limit $\mathcal{N} \gg 1$ we have $F_{\mathbf{k},q}F^{*}_{\mathbf{k},q'} \to |F_{\mathbf{k},q}|^2\delta_{qq'}$, thus allowing us to write Eq. (4.49) as

$$\begin{aligned}
&\mathrm{Tr}_{\mathrm{ph}}\left[\tilde{H}_{\mathrm{pl-ph}}(t), \left[\tilde{H}_{\mathrm{pl-ph}}(s), \tilde{\rho}^{\sigma}(s)\otimes\rho_{\mathrm{ph}}\right]\right] = \\
&\sum_q \left\{\mathcal{D}^{\sigma}_q(s-t)\left[B^{\sigma}_q(t) - B^{\sigma\dagger}_q(t), \left(B^{\sigma}_q(s) - B^{\sigma\dagger}_q(s)\right)\tilde{\rho}^{\sigma}(s)\right]\right. \\
&\qquad \left. -\mathcal{D}^{\sigma}_q(t-s)\left[B^{\sigma}_q(t) - B^{\sigma\dagger}_q(t), \tilde{\rho}^{\sigma}(s)\left(B^{\sigma}_q(s) - B^{\sigma\dagger}_q(s)\right)\right]\right\},
\end{aligned} \tag{4.53}$$

where the correlation function $\mathcal{D}_q^\sigma$ is defined as

$$\begin{aligned}\mathcal{D}_q^\sigma(\tau) =& \frac{\pi\hbar^2\omega_0^3 a^3}{\mathcal{V}}(\cosh\theta_q^\sigma + \sinh\theta_q^\sigma)^2 \sum_{\mathbf{k},\hat{\lambda}_\mathbf{k}} \frac{1}{\omega_\mathbf{k}} |\hat{\sigma}\cdot\hat{\lambda}_\mathbf{k}|^2 |F_{\mathbf{k},q}|^2 \\ &\times \left([1+n_{\rm ph}(\omega_\mathbf{k})]e^{\mathrm{i}\omega_\mathbf{k}\tau} + n_{\rm ph}(\omega_\mathbf{k})e^{-\mathrm{i}\omega_\mathbf{k}\tau}\right). \end{aligned} \tag{4.54}$$

Inserting the results for the traces Eqs. (4.44) and (4.53) in Eq. (4.33) we arrive at

$$\begin{aligned}\dot{\tilde{\rho}}^\sigma(t) \simeq& -\frac{1}{\hbar^2}\sum_q \int_0^t \mathrm{d}\tau \\ &\times \Big\{ \mathcal{C}_q^{\sigma *}(\tau)\left[B_q^\sigma(t)+B_q^{\sigma\dagger}(t), \left(B_q^\sigma(t-\tau)+B_q^{\sigma\dagger}(t-\tau)\right)\tilde{\rho}^\sigma(t-\tau)\right] \\ &- \mathcal{C}_q^\sigma(\tau)\left[B_q^\sigma(t)+B_q^{\sigma\dagger}(t), \tilde{\rho}^\sigma(t-\tau)\left(B_q^\sigma(t-\tau)+B_q^{\sigma\dagger}(t-\tau)\right)\right] \\ &+ \mathcal{D}_q^{\sigma *}(\tau)\left[B_q^\sigma(t)-B_q^{\sigma\dagger}(t), \left(B_q^\sigma(t-\tau)-B_q^{\sigma\dagger}(t-\tau)\right)\tilde{\rho}^\sigma(t-\tau)\right] \\ &- \mathcal{D}_q^\sigma(\tau)\left[B_q^\sigma(t)-B_q^{\sigma\dagger}(t), \tilde{\rho}^\sigma(t-\tau)\left(B_q^\sigma(t-\tau)-B_q^{\sigma\dagger}(t-\tau)\right)\right]\Big\}. \end{aligned} \tag{4.55}$$

The correlation functions (4.45) and (4.54) which contain all information about the evolution of the electronic and photonic baths, are the sums of oscillating exponentials. Thus, for large number of degrees of freedom (i.e. large bath limit) they interfere destructively, allowing the approximation that the correlation functions $\mathcal{C}_q^\sigma(\tau)$ and $\mathcal{D}_q^\sigma(\tau)$ decrease as a function of τ on very short timescale $\tau_{\rm c}$ (called the correlation time). For $\tau > \tau_{\rm c}$, $\mathcal{C}_q^\sigma(\tau), \mathcal{D}_q^\sigma \approx 0$. The above assumption amounts to the *Markovian approximation* [91, 94]. This simplification allows us to change the upper limit of the integral in the right-hand-side of Eq. (4.55) to ∞, thus implying that we consider evolution of the system on a timescale $t \gg \tau_{\rm c}$.

Moreover, both the coupling of the plasmons with electrons (4.14) and with photons (4.17) are weak, and since the right-hand-side of Eq. (4.55) is already quadratic in the coupling we may omit the evolution of the density matrix between $t-\tau$ and t leading to

$$\begin{aligned}\dot{\tilde{\rho}}^\sigma(t) \simeq& -\frac{1}{\hbar^2}\sum_q \int_0^\infty \mathrm{d}\tau \\ &\times \Big\{ \mathcal{C}_q^{\sigma *}(\tau)\left[B_q^\sigma(t)+B_q^{\sigma\dagger}(t), \left(B_q^\sigma(t-\tau)+B_q^{\sigma\dagger}(t-\tau)\right)\tilde{\rho}^\sigma(t)\right] \\ &- \mathcal{C}_q^\sigma(\tau)\left[B_q^\sigma(t)+B_q^{\sigma\dagger}(t), \tilde{\rho}^\sigma(t)\left(B_q^\sigma(t-\tau)+B_q^{\sigma\dagger}(t-\tau)\right)\right] \\ &+ \mathcal{D}_q^{\sigma *}(\tau)\left[B_q^\sigma(t)-B_q^{\sigma\dagger}(t), \left(B_q^\sigma(t-\tau)-B_q^{\sigma\dagger}(t-\tau)\right)\tilde{\rho}^\sigma(t)\right] \\ &- \mathcal{D}_q^\sigma(\tau)\left[B_q^\sigma(t)-B_q^{\sigma\dagger}(t), \tilde{\rho}^\sigma(t)\left(B_q^\sigma(t-\tau)-B_q^{\sigma\dagger}(t-\tau)\right)\right]\Big\}. \end{aligned} \tag{4.56}$$

Now, inserting the time evolution of the normal modes operators (4.38) into Eq. (4.56) and using the *rotating wave approximation* (i.e. omitting the terms proportional to $e^{\pm \mathrm{i}2\omega_q^\sigma \tau}$) in addition to the use of

$$\int_0^\infty \mathrm{d}\tau\, e^{\pm \mathrm{i}\Omega\tau} = \pm \mathrm{i}\mathcal{P}\frac{1}{\Omega} + \pi\delta(\Omega), \tag{4.57}$$

where $\mathcal{P}$ denotes the Cauchy principal value, we obtain in the zero temperature limit the master equation for the density matrix in the Lindblad form [26, 27, 91]

$$\begin{aligned}\dot{\rho}^\sigma =& -\mathrm{i}\sum_q \tilde{\omega}_q^\sigma \left[B_q^{\sigma\dagger}B_q^\sigma, \rho^\sigma\right] \\ & -\sum_q \frac{\gamma_q^\sigma}{2}\left(B_q^{\sigma\dagger}B_q^\sigma\rho^\sigma + \rho^\sigma B_q^{\sigma\dagger}B_q^\sigma - 2B_q^\sigma\rho B_q^{\sigma\dagger}\right).\end{aligned} \tag{4.58}$$

We may extend this equation by adding the effect of the driving field (4.18) through

$$\dot{\rho}^\sigma = -(\mathrm{i}/\hbar)\left[H_{\mathrm{drive}}, \rho^\sigma\right], \tag{4.59}$$

which leads to final form of the master equation (4.58)

$$\begin{aligned}\dot{\rho}^\sigma =& -\mathrm{i}\sum_q \tilde{\omega}_q^\sigma \left[B_q^{\sigma\dagger}B_q^\sigma, \rho^\sigma\right] \\ & -\sum_q \frac{\gamma_q^\sigma}{2}\left(B_q^{\sigma\dagger}B_q^\sigma\rho^\sigma + \rho^\sigma B_q^{\sigma\dagger}B_q^\sigma - 2B_q^\sigma\rho B_q^{\sigma\dagger}\right) \qquad (4.60)\\ & +\mathrm{i}\sum_q \frac{\mathcal{A}_q^\sigma f(t)}{2\tilde{\omega}_q^\sigma}\left[B_q^{\sigma\dagger} + B_q^\sigma, \rho^\sigma\right], \qquad (4.61)\end{aligned}$$

where the amplitude $\mathcal{A}_q^\sigma$ is defined as

$$\mathcal{A}_q^\sigma = -2\sqrt{\frac{2}{\mathcal{N}+1}}\hat{\sigma}\cdot\hat{\epsilon}\sin(qd)\,\Omega_{\mathrm{R}}\tilde{\omega}_q^\sigma\sqrt{\frac{\omega_0}{\omega_q^\sigma}}. \tag{4.62}$$

The rate $\gamma_q^\sigma = \gamma^{\mathrm{a}} + \gamma_q^{\sigma,\mathrm{L}} + \gamma_q^{\sigma,\mathrm{r}}$ entering the master equation (4.60) and describing the decay of a collective plasmonic mode $\{q,\sigma\}$ into the ground state consists of three components: (i) the non-radiative bulk Ohmic losses characterized by the (mode-independent) decay rate γ^{a} [which is phenomenologically incorporated in the master equation (4.60) and not through a first-principle calculation], (ii) the non-radiative Landau damping linewidth $\gamma_q^{\sigma,\mathrm{L}}$, and (iii) the radiative losses with decay rate $\gamma_q^{\sigma,\mathrm{r}}$.

The non-radiative Landau damping decay rate arising from the coupling Hamiltonian (3.14) reads

$$\gamma_q^{\sigma,\mathrm{L}} = \frac{\omega_0}{\omega_q^\sigma}\Sigma^\sigma(\omega_q^\sigma) \tag{4.63}$$

with $\Sigma^\sigma(\omega)$ defined in Eq. (2.28) and evaluated in Eq. (2.35). The radiative decay rate originating from the plasmon-photon interaction (4.17) is given by

$$\gamma_q^{\sigma,\mathrm{r}} = 2\pi^2\omega_0^2\omega_q^\sigma\frac{a^3}{\mathcal{V}}\sum_{\mathbf{k},\hat{\lambda}_\mathbf{k}}\frac{\left|\hat{\sigma}\cdot\hat{\lambda}_\mathbf{k}\right|^2}{\omega_\mathbf{k}}|F_{\mathbf{k},q}|^2\delta(\omega_q^\sigma-\omega_\mathbf{k}), \tag{4.64}$$

In the master equation (4.60), the eigenfrequency $\tilde{\omega}_q^\sigma = \omega_q^\sigma - (\delta_q^{\sigma,\mathrm{L}} + \delta_q^{\sigma,\mathrm{r}})$ contains the redshifts due to the interaction with electronic [21, 23, 25] and photonic [91] environments, which read, respectively,

$$\delta_q^{\sigma,\mathrm{L}} = \frac{2}{\hbar^2}\Lambda^2\frac{\omega_0}{\omega_q^\sigma}\mathcal{P}\sum_{eh}|\langle e|\sigma|h\rangle|^2\frac{\omega_{eh}}{\omega_{eh}^2-\omega_q^{\sigma\,2}} \tag{4.65}$$

and

$$\delta_q^{\sigma,\mathrm{r}} = 2\pi\omega_0^2\omega_q^\sigma\frac{a^3}{\mathcal{V}}\mathcal{P}\sum_{\mathbf{k},\hat{\lambda}_\mathbf{k}}|\hat{\sigma}\cdot\hat{\lambda}_\mathbf{k}|^2|F_{\mathbf{k}q}|^2\frac{1}{\omega_\mathbf{k}^2-\omega_q^{\sigma\,2}}. \tag{4.66}$$

Nonetheless, these shifts are very small and we will neglect them in our study of the plsamon propagation.

4.3 Nonradiative and radiative decay rates of the collective plasmonic modes

We now turn to the evaluation of the nonradiative and radiative decay rates given by the Fermi golden rule expressions in Eqs. (4.63) and (4.64), respectively.

4.3.1 Landau damping

Evaluating the Landau damping (4.63) with the use of Eq. (2.35) yields

$$\gamma_q^{\sigma,\mathrm{L}} = \frac{3v_\mathrm{F}}{4a}\left(\frac{\omega_0}{\omega_q^\sigma}\right)^4 g\left(\frac{\hbar\omega_q^\sigma}{E_\mathrm{F}}\right), \tag{4.67}$$

where $g(\nu)$ is defined in Eq. (2.37).

The nonradiative decay rate (4.67) scales as the inverse of the nanoparticle size, so that for small enough nanoparticles Landau damping dominates over radiation damping (which scales as the particle volume, see Sec. 4.3.2).

The Landau damping decay rates of the transverse and longitudinal collective plasmon modes are shown in Fig. 4.3 as a function of momentum. Once scaled with the Landau damping decay rate of a single nanoparticle [14, 17, 24] γ_0^L [c.f. (2.38)], the nonradiative linewidths of the coupled plasmons show a significant modulation as a function of

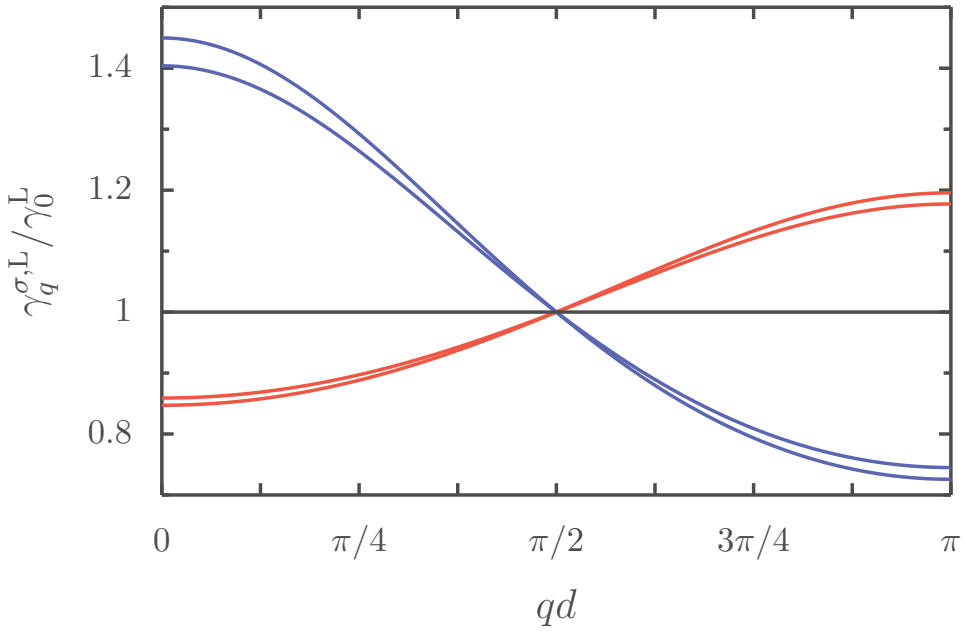

Figure 4.3: Landau damping decay rate from Eq. (4.67) as a function of momentum for the transverse (red dashed lines, $\sigma = x, y$) and longitudinal (blue solid lines, $\sigma = z$) collective plasmonic modes for an interparticle separation $d = 3a$. The thick (thin) lines correspond to $\hbar\omega_0/E_{\mathrm{F}} = 0.5$ ($\hbar\omega_0/E_{\mathrm{F}} = 1$).

the wavelength of the modes (between -25% and $+45\%$ for the longitudinal mode). The higher the frequency of the mode, the lower is its Landau damping linewidth, as for an isolated nanoparticle [27]. Notice also that the dependence of $\gamma_q^{\sigma,\mathrm{L}}$ on the ratio $\hbar\omega_0/E_{\mathrm{F}}$ is rather weak (thick and thin lines in Fig. 4.3 correspond to $\hbar\omega_0/E_{\mathrm{F}} = 0.5$ and 1, respectively). This is due to the relatively smooth behavior of the monotonically decreasing function $g(\nu)$ [defined in Eq. (2.37)] for realistic values of the ratio $\nu = \hbar\omega_0/E_{\mathrm{F}}$.

4.3.2 Radiative damping

In the Fermi golden rule (4.64) for the radiative decay rate of the collective plasmons, the summation over photon polarizations was done in Eq. (2.41), while the sum over photonic momenta $\mathbf{k}$ is performed in the continuous limit ($\mathcal{V} \to \infty$). Using spherical coordinates for the integral over $\mathbf{k}$, we arrive at

$$\gamma_q^{\sigma,\mathrm{r}} = \frac{3|\eta_\sigma|}{8}\gamma_0^{\mathrm{r}}\left(\frac{\omega_q^\sigma}{\omega_0}\right)^2 \times \int_0^\pi \mathrm{d}\theta \sin\theta \left(1 + \mathrm{sgn}\{\eta_\sigma\}\cos^2\theta\right)|F_{\mathbf{k}_q^\sigma,q}|^2 \tag{4.68}$$

for the radiative decay rates of the transverse ($\sigma = x, y$) and longitudinal ($\sigma = z$) collective plasmons, respectively. $\gamma_0^{\rm r}$ [c.f. (2.45)] is the radiation damping decay rate of a single isolated nanoparticle, and

$$|F_{\mathbf{k}_q^\sigma,q}|^2 = \frac{1}{2(\mathcal{N}+1)} \left\{ \sum_{\kappa=\pm} \frac{\sin^2\left(\mathcal{N}[q+\kappa k_q^\sigma \cos\theta]d/2\right)}{\sin^2\left([q+\kappa k_q^\sigma \cos\theta]d/2\right)} \right.$$
$$\left. -2\cos([\mathcal{N}+1]qd) \prod_{\kappa=\pm} \frac{\sin\left(\mathcal{N}[q+\kappa k_q^\sigma \cos\theta]d/2\right)}{\sin\left([q+\kappa k_q^\sigma \cos\theta]d/2\right)} \right\}, \qquad (4.69)$$

where $k_q^\sigma = \omega_q^\sigma/c$. In the infinite chain limit ($\mathcal{N} \to \infty$), the expression above reduces to

$$|F_{\mathbf{k}_q^\sigma,q}|^2 \simeq \pi \sum_{\kappa=\pm} \delta([q+\kappa k_q^\sigma \cos\theta]d), \qquad (4.70)$$

so that the remaining integral in Eq. (4.68) is easily performed, yielding

$$\gamma_q^{\sigma,{\rm r}} = \frac{3\pi|\eta_\sigma|\gamma_0^{\rm r}}{4k_0 d} \frac{\left(\omega_q^\sigma\right)^2 + {\rm sgn}\{\eta_\sigma\}\left(cq\right)^2}{\omega_0 \omega_q^\sigma} \Theta\left(\omega_q^\sigma - cq\right). \qquad (4.71)$$

In Fig. 4.4, we compare our analytical results for transverse (a) and longitudinal (b) plasmonic modes in infinite chains ($\mathcal{N} \to \infty$), Eq. (4.71), to a numerical evaluation of Eq. (4.68) for finite chains containing $\mathcal{N} = \{5, 10, 20\}$ nanoparticles. As one can see from Fig. 4.4, the behavior of the finite chain approaches the analytical infinite chain limit with a rather good agreement already for $\mathcal{N} = 20$. For $\mathcal{N} = 50$, the continuous black line representing the analytical result of Eq. (4.71) in Fig. 4.4 and the numerical data points (not shown in the figure) almost coincide.

The expression (4.71) shows that dark plasmonic modes with a wavelength smaller than $\sim 2\pi/k_0$ ($q \gtrsim k_0$), *i.e.*, outside of the light cone, have a vanishing radiative decay rate. This behavior comes from the destructive interference of the electric field associated with small domains of in-phase LSPs, resulting in subradiant collective modes which do not couple to light. The results in Eq. (4.71) and in Fig. 4.4 also show that most of the collective plasmons with a wavelength larger than $\sim 2\pi/k_0$ ($q \lesssim k_0$) are superradiant, with radiative decay rates that exceed the one of a single nanoparticle $\gamma_0^{\rm r}$. Moreover, as illustrated in the inset in Fig. 4.4, the expression (4.71) shows that the radiative linewidth $\gamma_q^{\sigma,{\rm r}}$, scaled with $\gamma_0^{\rm r}/k_0 d$, is almost a universal function of q/k_0. In the limit of uncoupled nanoparticles ($\Omega \to 0$) it is easy to show that $\int {\rm d}q\ \gamma_q^{\sigma,{\rm r}} = \pi\gamma_0^{\rm r}/d$ for both, the transverse and the longitudinal mode.

The behavior of the radiative decay of the transverse and longitudinal plasmonic modes in Fig. 4.4 has been demonstrated by means of

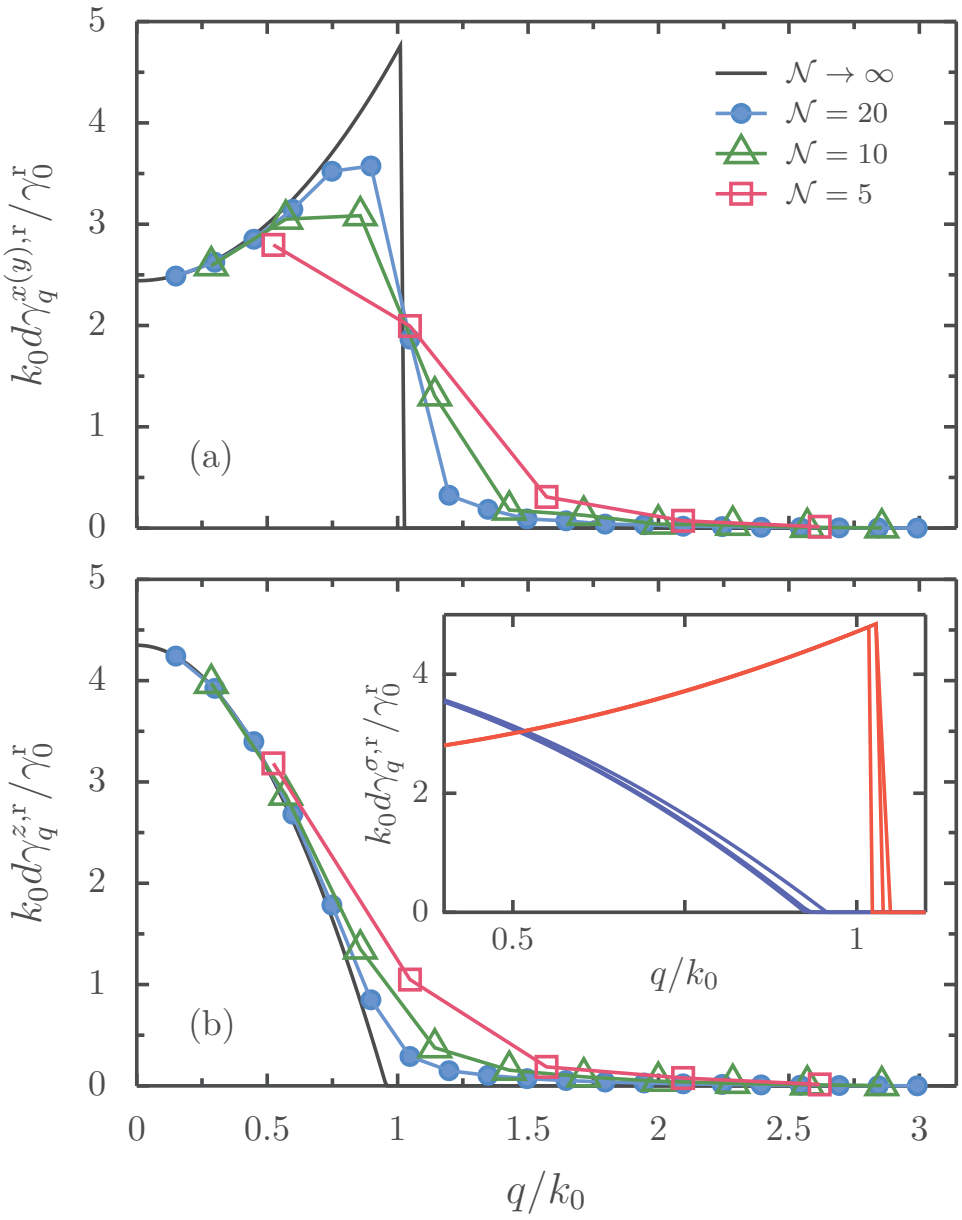

Figure 4.4: Radiation damping decay rate from Eq. (4.68) as a function of momentum for the (a) transverse and (b) longitudinal collective plasmonic modes for $k_0 d = 1$ in chains with $d = 3a$ that contain various numbers $\mathcal{N}$ of nanoparticles. The thick solid lines correspond to $\mathcal{N} \to \infty$, [cf. Eq. (4.71)]. The inset shows the radiation damping decay rate from Eq. (4.71) for the transverse (red dashed lines) and longitudinal (blue solid lines) collective plasmonic modes for $k_0 d = 0.25$, 0.5 and 1 from the thin to the thicker line.

sophisticated numerical and semi-analytical calculations in the past, including retardation in the interaction between the nanoparticles [46,47, 51–53, 65]. Our transparent analytical result (4.71) shows that a quasistatic description of the interparticle interactions is sufficient to de-

scribe, at least qualitatively, radiative energy losses in metallic nanoparticle chains.

4.4 Plasmon propagation along the nanoparticle chain

After having obtained analytical expressions for the nonradiative and radiative lifetimes of the collective plasmons in Sec. 4.3, we are now in a position of studying the plasmon propagation along the chain. To this end, we introduce the (dimensionless) dipole moment $\sigma_n = \langle b_n^\sigma + b_n^{\sigma\dagger} \rangle$ bared by nanoparticle n. This quantity can be calculated from its time evolution in momentum space, itself obtained from the master equation (4.60) using that $\langle \dot{\mathcal{O}} \rangle = \mathrm{Tr}\{\dot{\rho}\mathcal{O}\}$ for any operator $\mathcal{O}$. Using the above relation for $\sigma_q = \langle B_q^\sigma + B_q^{\sigma\dagger} \rangle$ [cf. Eq. (4.5)] and momentum $\pi_q^\sigma = \langle B_q^\sigma - B_q^{\sigma\dagger} \rangle$ we get

$$\dot{\sigma}_q = \mathrm{i}\omega_q^\sigma \pi_q^\sigma - \frac{\gamma_q^\sigma}{2}\sigma_q + \mathrm{i}\frac{\mathcal{A}_q^\sigma f(t)}{2\omega_q^\sigma}, \tag{4.72a}$$

$$\dot{\pi}_q^\sigma = \mathrm{i}\omega_q^\sigma \sigma_q - \frac{\gamma_q^\sigma}{2}\pi_q^\sigma. \tag{4.72b}$$

Taking the time derivative of Eq. (4.72a) and using Eq. (4.72b) we get

$$\ddot{\sigma}_q + \gamma_q^\sigma \dot{\sigma}_q + \Omega_q^{\sigma 2}\sigma_q = \mathcal{A}_q^\sigma f(t), \tag{4.73}$$

with $\Omega_q^{\sigma 2} = \tilde{\omega}_q^{\sigma 2} + (\gamma_q^\sigma/2)^2$, and where the amplitude of the driving force $\mathcal{A}_q^\sigma$ is defined in Eq. (4.62). In the following we first consider the case of a continuous drive by a monochromatic electric field, and then the case of the irradiation of the first nanoparticle by an extremely short (δ-like) laser excitation.

4.4.1 Continuous driving by a monochromatic electric field

We start by considering the case where the first nanoparticle in the chain is illuminated by a long-wavelength monochromatic electric field at the driving frequency ω_d, for which $f(t) = \sin(\omega_\mathrm{d} t)$. The stationary solution of Eq. (4.73) then reads

$$\sigma_q = \mathcal{S}_q^\sigma \sin(\omega_\mathrm{d} t) + \mathcal{C}_q^\sigma \cos(\omega_\mathrm{d} t) \tag{4.74}$$

with

$$\mathcal{S}_q^\sigma = \mathcal{A}_q^\sigma \frac{\Omega_q^{\sigma 2} - \omega_\mathrm{d}^2}{\left(\omega_\mathrm{d}^2 - \Omega_q^{\sigma 2}\right)^2 + \left(\gamma_q^\sigma \omega_\mathrm{d}\right)^2} \tag{4.75a}$$

and

$$\mathcal{C}_q^\sigma = \mathcal{A}_q^\sigma \frac{-\gamma_q^\sigma \omega_\mathrm{d}}{\left(\omega_\mathrm{d}^2 - \Omega_q^{\sigma 2}\right)^2 + \left(\gamma_q^\sigma \omega_\mathrm{d}\right)^2}. \tag{4.75b}$$

The root mean square dipole moment is defined as

$$\sqrt{\Delta\sigma_n^2} = \sqrt{\overline{\sigma_n^2} - \overline{\sigma}_n{}^2}, \tag{4.76}$$

where the bar denotes time averaging. Since the time-averaged dipole moment is zero (i.e. $\bar{\sigma}_n = 0$), Eq. (4.76) therefore reads

$$\sqrt{\Delta\sigma_n^2} = \frac{1}{\sqrt{\mathcal{N}+1}} \sqrt{(\tilde{\mathcal{S}}_n^\sigma)^2 + (\tilde{\mathcal{C}}_n^\sigma)^2}. \tag{4.77}$$

with

$$\tilde{\mathcal{S}}_n^\sigma = \sum_q \frac{\sin(nqd)}{\sqrt{\omega_q^\sigma/\omega_0}} \mathcal{S}_q^\sigma \tag{4.78a}$$

and

$$\tilde{\mathcal{C}}_n^\sigma = \sum_q \frac{\sin(nqd)}{\sqrt{\omega_q^\sigma/\omega_0}} \mathcal{C}_q^\sigma. \tag{4.78b}$$

In Figs. 4.5(a)-(d) we present numerical results for the average stationary dipole moment on nanoparticle n [cf. Eq. (4.77)] for the transverse (red dashed lines) and longitudinal modes (blue solid lines) along a chain composed of $\mathcal{N} = 1000$ Ag nanoparticles. Panels (a) to (d) in Fig. 4.5 correspond to nanoparticle radii $k_\mathrm{F}a = 100$, 350, 500 and 750, respectively, with k_F the Fermi wavevector, keeping the interparticle distance fixed to $d = 3a$.

We observe two different regimes for the decay of the dipole moment along the chain: Over the first few nanoparticles of the chain, the decay of the excitation is purely exponential

$$\sqrt{\frac{\Delta\sigma_n^2}{\Delta\sigma_1^2}} = e^{-(n-1)d/\xi^\sigma}, \tag{4.79}$$

with ξ^σ the propagation length for the polarization σ. Remarkably, such an exponential decay is exclusively due to nonradiative decay mechanisms of the collective plasmons, i.e. absorption losses and Landau damping. Indeed, the numerical evaluation of Eq. (4.77) without radiation damping (4.71) reproduce almost perfectly the exponential decay of $\sqrt{\Delta\sigma_n^2}$ shown in Figures 4.5(a)-(d).

For longer distances along the chain, the decay of the excitation is algebraic [see thick solid and dashed lines in Figures 4.5(a)-(d) which correspond to $\sqrt{\Delta\sigma_n^2} \sim 1/n^{\zeta^\sigma}$]. This algebraic decay results solely from the radiation damping rate (4.71) and its behavior as a function of momentum. The latter for the transverse modes is discontinuous

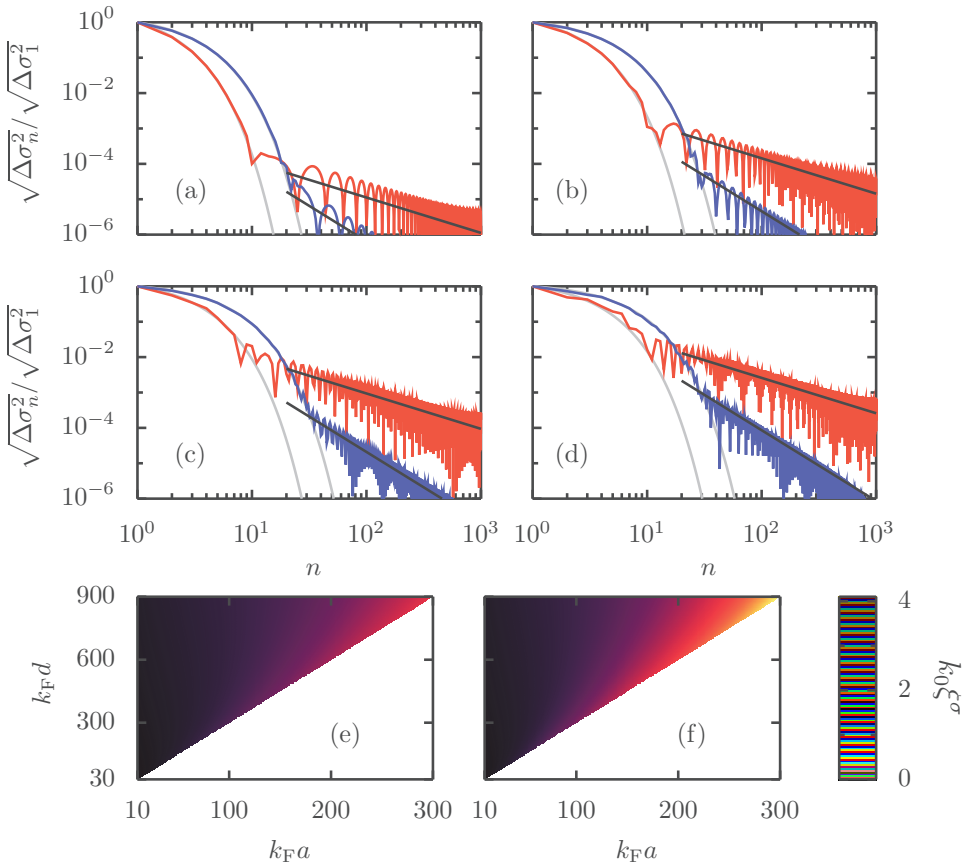

Figure 4.5: (a)-(d) Normalized time averaged root mean square dipole moment on nanoparticle n resulting from a monochromatic excitation at frequency $\omega_d = \omega_0$ of the 1st nanoparticle in a chain with $\mathcal{N} = 1000$ and interparticle distance $d = 3a$. Dashed red and solid blue lines correspond respectively to the numerical evaluation of Eq. (4.77) for the transverse and longitudinal modes, including, absorption losses, Landau and radiation damping. The thick dashed and solid gray lines corresponding to the analytical result (4.90) include only nonradiative losses, i.e. absorption and Landau damping. The nanoparticle sizes are (a) $k_F a = 50$, (b) $k_F a = 100$, (c) $k_F a = 200$, and (d) $k_F a = 300$. The thick dashed and solid black lines are algebraic fits for the transverse and longitudinal modes, respectively (see text). (e)-(f) Propagation length ξ^σ from Eq. (4.91) for (e) transverse (f) longitudinal modes as a function of a and d. the parameters in the figure are $\gamma^a/\omega_0 = 0.027$, $\hbar\omega_0/E_F = 0.47$, and $\omega_0/ck_F = 1.1 \times 10^{-3}$, corresponding to a chain of Ag nanoparticles. The frequency shifts (4.65) and (4.66) have been neglected.

(for $\mathcal{N} \gg 1$) at $q \approx k_0$ [see Fig. 4.4(a)], yielding $\zeta^{x,y} \simeq 1$ [see thick dashed lines in Figs. 4.5(a)-(d)], while for the longitudinal mode [see Fig. 4.4(b)], the monotonic decaying behavior of the radiative damping rate for $q \lesssim k_0$ yields $\zeta^z \simeq 2$. The algebraic behavior of the plasmon

decay along the chain becomes more dominant for increasing nanoparticle size and interparticle distance, at the constant ratio $d = 3a$ used in Figures 4.5(a)-(d). This is a result of the increasing influence of the radiation damping on the overall collective plasmon linewidth for increasing nanoparticle sizes.

Within the perspective of energy transfer, the initial exponential regime witnessed in Figures 4.5(a)-(d) is the determinant one. Therefore, it is useful to search for the maximization of the propagation length ξ^σ defined in Eq. (4.79) within the parameter range of the present model. Below we provide an analytical calculation of the root mean square dipole moment (4.77) in the weakly-coupled nanoparticle regime, and subsequently we deduce the propagation length ξ^σ as a function of the parameters of our model.

Since the exponential decay of the plasmon excitation is of nonradiative origin, in what follows we neglect the radiation damping (4.71). Moreover, we neglect the frequency shifts (4.65) and (4.66), as they represent a very small correction to the collective mode resonant frequencies [25]. To linear order in the coupling Ω/ω_0 and to quadratic order in γ_q^σ/ω_0, using Eqs. (4.11) and (4.67), the coefficients (4.75) read for $\omega_\mathrm{d} = \omega_0$

$$\mathcal{S}_q^\sigma \simeq \frac{\mathcal{A}_q^\sigma}{4\omega_0^2} \frac{\eta_\sigma \Omega \omega_0 \cos(qd) + (\gamma^\mathrm{nr}/4)^2}{[\eta_\sigma \Omega \omega_0 \cos(qd)]^2 + (\gamma^\mathrm{nr}/4)^2} \tag{4.80a}$$

and

$$\mathcal{C}_q^\sigma \simeq -\frac{\mathcal{A}_q^\sigma}{8\omega_0^2} \frac{\gamma^\mathrm{nr}\omega_0/2 + \eta_\sigma \gamma_0^\mathrm{L} \Omega G(\hbar\omega_0/E_\mathrm{F}) \cos(qd)}{[\eta_\sigma \Omega \omega_0 \cos(qd)]^2 + (\gamma^\mathrm{nr}/4)^2}, \tag{4.80b}$$

where $\gamma^\mathrm{nr} = \gamma^\mathrm{a} + \gamma_0^\mathrm{L}$ is the nonradiative part of the damping rate corresponding to a single nanoparticle and $G(\nu) = \mathrm{d}g(\nu)/\mathrm{d}\nu$. In the large chain limit ($\mathcal{N} \gg 1$), we replace the summation over plasmon momentum in Eq. (4.78) by an integral and arrive using Eq. (4.80), to

$$\mathcal{S}_n^\sigma \simeq -\frac{\sqrt{2(\mathcal{N}+1)}}{2\pi\eta_\sigma} \hat{\sigma} \cdot \hat{\epsilon} \frac{\Omega_\mathrm{R}}{\Omega} \left[\frac{(\gamma^\mathrm{nr}/4)^2}{\eta_\sigma \Omega \omega_0} \mathcal{I}\left(\frac{\gamma^\mathrm{nr}}{4|\eta_\sigma|\Omega}\right) + \mathcal{J}\left(\frac{\gamma^\mathrm{nr}}{4|\eta_\sigma|\Omega}\right) \right] \tag{4.81a}$$

and

$$\begin{aligned} \mathcal{C}_n^\sigma \simeq & -\frac{\sqrt{2(\mathcal{N}+1)}}{4\pi\eta_\sigma} \hat{\sigma} \cdot \hat{\epsilon} \frac{\Omega_\mathrm{R}}{\Omega} \left[\frac{\gamma^\mathrm{nr}}{2\eta_\sigma \Omega} \mathcal{I}\left(\frac{\gamma^\mathrm{nr}}{4|\eta_\sigma|\Omega}\right) \right. \\ & \left. + G\left(\frac{\hbar\omega_0}{E_\mathrm{F}}\right) \frac{\gamma_0^\mathrm{L}}{\omega_0} \mathcal{J}\left(\frac{\gamma^\mathrm{nr}}{4|\eta_\sigma|\Omega}\right) \right] \end{aligned} \tag{4.81b}$$

The two integrals appearing in Eq. (4.81) are defined by

$$\mathcal{I}_n(\alpha) = \int_0^\pi \mathrm{d}x \, \frac{\sin x \sin(nx)}{\cos^2 x + \alpha^2} \tag{4.82}$$

and

$$\mathcal{J}_n(\alpha) = \int_0^\pi \mathrm{d}x \, \frac{\sin x \cos x \sin(nx)}{\cos^2 x + \alpha^2}, \tag{4.83}$$

where α is real and positive, and n is an integer strictly larger than 0. It is easy to show that

$$\mathcal{I}_n(\alpha) = \frac{1}{2}\mathrm{Im} \int_0^{2\pi} \mathrm{d}x \, \frac{\sin x \, \mathrm{e}^{\mathrm{i}nx}}{\cos^2 x + \alpha^2} \tag{4.84}$$

for n odd and $\mathcal{I}_n(\alpha) = 0$ for n even, while

$$\mathcal{J}_n(\alpha) = \frac{1}{2}\mathrm{Im} \int_0^{2\pi} \mathrm{d}x \, \frac{\sin x \cos x \, \mathrm{e}^{\mathrm{i}nx}}{\cos^2 x + \alpha^2} \tag{4.85}$$

for n even and $\mathcal{J}_n(\alpha) = 0$ for n odd. Changing variables to $z = \mathrm{e}^{\mathrm{i}x}$ in Eqs. (4.84) and (4.85), we arrive at

$$\mathcal{I}_n(\alpha) = -\mathrm{Im} \oint \mathrm{d}z \, \frac{(z^2-1)z^n}{z^4 + 2(1+2\alpha^2)z^2 + 1} \tag{4.86}$$

and

$$\mathcal{J}_n(\alpha) = -\frac{1}{2}\mathrm{Im} \oint \mathrm{d}z \, \frac{(z^4-1)z^{n-1}}{z^4 + 2(1+2\alpha^2)z^2 + 1}, \tag{4.87}$$

where the two above integrals are taken over the unit circle in the complex plane. The denominator of the integrands appearing in Eqs. (4.86) and (4.87) has two simple poles lying outside of the unit circle, $z_\pm^{\mathrm{out}} = \pm\mathrm{i}[(1+\alpha^2)^{1/2} + \alpha]$, and two simple poles lying inside of the unit circle, $z_\pm^{\mathrm{in}} = \pm\mathrm{i}[(1+\alpha^2)^{1/2} - \alpha]$. By the residue theorem, we thus arrive to the final results

$$\mathcal{I}_n(\alpha) = [1 - (-1)^n] \, \mathrm{Im}\{\mathrm{i}^n\} \frac{\pi}{2} \frac{\left(\sqrt{1+\alpha^2} - \alpha\right)^n}{\alpha} \tag{4.88}$$

and

$$\mathcal{J}_n(\alpha) = -\left[1 + (-1)^n\right] \mathrm{Im}\{\mathrm{i}^{n+1}\} \frac{\pi}{2} \left(\sqrt{1+\alpha^2} - \alpha\right)^n \tag{4.89}$$

for all integers $n \geqslant 1$.

With Eqs. (4.88) and (4.89) and to leading order in Ω/ω_0 and γ_q^σ/ω_0, Eq. (4.77) finally reads

$$\sqrt{\Delta\sigma_n^2} \simeq \frac{|\hat{\sigma}\cdot\hat{\epsilon}|}{\sqrt{2}|\eta_\sigma|} \frac{\Omega_{\mathrm{R}}}{\Omega} \left[\sqrt{1 + \left(\frac{\gamma^{\mathrm{nr}}}{4|\eta_\sigma|\Omega}\right)^2} - \frac{\gamma^{\mathrm{nr}}}{4|\eta_\sigma|\Omega} \right]^n. \tag{4.90}$$

The decay of the plasmon excitation then follows the exponential behavior (4.79), with a decay length

$$\xi^\sigma = \frac{d}{\mathrm{arcsinh}(\gamma^{\mathrm{nr}}/4|\eta_\sigma|\Omega)}. \tag{4.91}$$

The latter, once scaled with the interparticle distance d, is a monotonically decreasing function of the unique parameter $\gamma^{\rm nr}/\Omega$. For weak dissipation and/or strong coupling ($\gamma^{\rm nr} \ll \Omega$), it behaves as $\xi^\sigma/d \simeq 4|\eta_\sigma|\Omega/\gamma^{\rm nr}$, while in the opposite regime $\gamma^{\rm nr} \gg \Omega$, $\xi^\sigma/d \simeq [\ln(\gamma^{\rm nr}/4|\eta_\sigma|\Omega) + \ln 2]^{-1}$.

We show in Figs. 4.5(a)-(d) our analytical result (4.90) for the transverse and longitudinal modes by thick solid and dashed gray lines, respectively. As can be seen from the figure, the agreement between Eq. (4.90) and the exponential part of the plasmon decay as obtained from the numerics is excellent, confirming that such an exponential behavior is solely of nonradiative origin.

The propagation length (4.91) is plotted in Fig. 4.5(e) for the transverse modes and in Fig. 4.5(f) for the longitudinal one for chains of Ag nanoparticles. The propagation length ξ^σ is measured in units of $k_0^{-1} = 76$ nm, while a and d are measured in units of $k_{\rm F}^{-1} = 0.83\mathring{A}$. In these two figures, we only show data points for $d \geqslant 3a$, as our model of point dipoles interacting through a quasistatic interaction is not valid for smaller interparticle distances [45].

As can be seen from panels (e) and (f) in Fig. 4.5 and inferred from Eq. (4.91), the smaller the interparticle distance d and the larger the nanoparticle radii a, i.e., the larger the coupling constant $\Omega = (\omega_0/2)(a/d)^3$, the larger the resulting propagation length ξ^σ is achieved. For a fixed d, the maximum ξ^σ is attained for $d/a = 3$, that is, at the limit of validity of the near-field approximation adopted in this work. It is then expected that the optimal propagation lengths occur for $d/a < 3$.

An important conclusion that can be extracted from Figs. 4.5(e) and 4.5(f) and from Eq. (4.91) is that the longitudinal mode generally propagates for a longer distance than the transverse one, thus confirming previous numerical studies [37, 40, 44] in the framework of a well-defined criterion. This is due to the fact that the LSPs have an effective interaction strength in Eq. (3.11) which is twice as much in the longitudinal case ($|\eta_z| = 2$) than in the transverse case ($|\eta_{x,y}| = 1$).

4.4.2 Short laser pulse excitation

We now consider an alternative situation of experimental relevance, where the first nanoparticle in the chain is irradiated by a very short laser pulse. In such a case, $f(t) = \delta(\omega_0 t)$ and the solution of Eq. (4.73) can be readily obtained, yielding the (dimensionless) dipole moment on nanoparticle n,

$$\sigma_n(t) = \sqrt{\frac{2}{(\mathcal{N}+1)\omega_0}}\Theta(t)\sum_q \frac{\mathcal{A}_q^\sigma}{(\omega_q^\sigma)^{3/2}}\sin(nqd)\mathrm{e}^{-\gamma_q^\sigma t/2}\sin(\omega_q^\sigma t). \tag{4.92}$$

We have checked by a numerical evaluation of Eq. (4.92) (not shown) that the radiation damping very weakly affects the decay of the plasmon excitation along the chain for short distances (below ca. 10 nanoparticles), as is the case for the continuous drive by a monochromatic field (see Sec. 4.4.1). Along the same lines as in the previous section, in the following we analytically evaluate Eq. (4.92) by disregarding the radiation damping (4.71). We further ignore the frequency shifts (4.65) and (4.66). In the large chain limit, and working up to leading order in $\Omega/\omega_0 \ll 1$, we obtain

$$\begin{aligned}\sigma_n(t) \simeq & -\frac{4}{\pi}\,\hat{\sigma}\cdot\hat{\epsilon}\,\frac{\Omega_{\rm R}}{\omega_0}\,\Theta(t)\,{\rm e}^{-\gamma^{\rm nr}t/2} \\ & \times\Big[\mathcal{K}_n\left(2\eta_\sigma\Omega t,\eta_\sigma\gamma_0^{\rm L}G(\hbar\omega_0/E_{\rm F})\Omega t/\omega_0\right)\sin\left(\omega_0 t\right) \\ & +\ \mathcal{L}_n\left(2\eta_\sigma\Omega t,\eta_\sigma\gamma_0^{\rm L}G(\hbar\omega_0/E_{\rm F})\Omega t/\omega_0\right)\cos\left(\omega_0 t\right)\Big]\,. \end{aligned} \tag{4.93}$$

The two integrals involved in the expression (4.93) describing the dipole moment resulting from the pulsed excitation of the first nanoparticle in the chain are defined by

$$\mathcal{K}_n(\alpha,\beta)=\int_0^\pi {\rm d}x\,\sin\left(nx\right)\sin x\cos\left(\alpha\cos x\right)\,{\rm e}^{-\beta\cos x} \tag{4.94}$$

and

$$\mathcal{L}_n(\alpha,\beta)=\int_0^\pi {\rm d}x\,\sin\left(nx\right)\sin x\sin\left(\alpha\cos x\right)\,{\rm e}^{-\beta\cos x}, \tag{4.95}$$

where α and β are both real and where n is an integer strictly larger than zero. Using that

$$\int_0^\pi {\rm d}x\,\cos\left(nx\right)\cos\left(z\cos x\right)=\pi\cos\left(\frac{n\pi}{2}\right)J_n(z) \tag{4.96}$$

and

$$\int_0^\pi {\rm d}x\,\cos\left(nx\right)\sin\left(z\cos x\right)=\pi\sin\left(\frac{n\pi}{2}\right)J_n(z), \tag{4.97}$$

where $J_n(z)$ denotes the Bessel function of the first kind with z a complex variable, we obtain

$$\mathcal{K}_n(\alpha,\beta)=\pi n\ {\rm Im}\left\{{\rm e}^{{\rm i}n\pi/2}\,\frac{J_n(\alpha+{\rm i}\beta)}{\alpha+{\rm i}\beta}\right\} \tag{4.98}$$

and

$$\mathcal{L}_n(\alpha,\beta)=-\pi n\ {\rm Re}\left\{{\rm e}^{{\rm i}n\pi/2}\,\frac{J_n(\alpha+{\rm i}\beta)}{\alpha+{\rm i}\beta}\right\}. \tag{4.99}$$

Together with Eqs. (4.98) and (4.99), we then obtain to leading order in Ω/ω_0 and in γ_q^σ/ω_0 the result

$$\sigma_n(t)=\frac{2\Omega_{\rm R}}{\omega_0}\,\hat{\sigma}\cdot\hat{\epsilon}\,\Theta(t)\frac{{\rm e}^{-\gamma^{\rm nr}t/2}\cos\left(\omega_0 t+n\pi/2\right)\,nJ_n(2\eta_\sigma\Omega t)}{\eta_\sigma\Omega t} \tag{4.100}$$

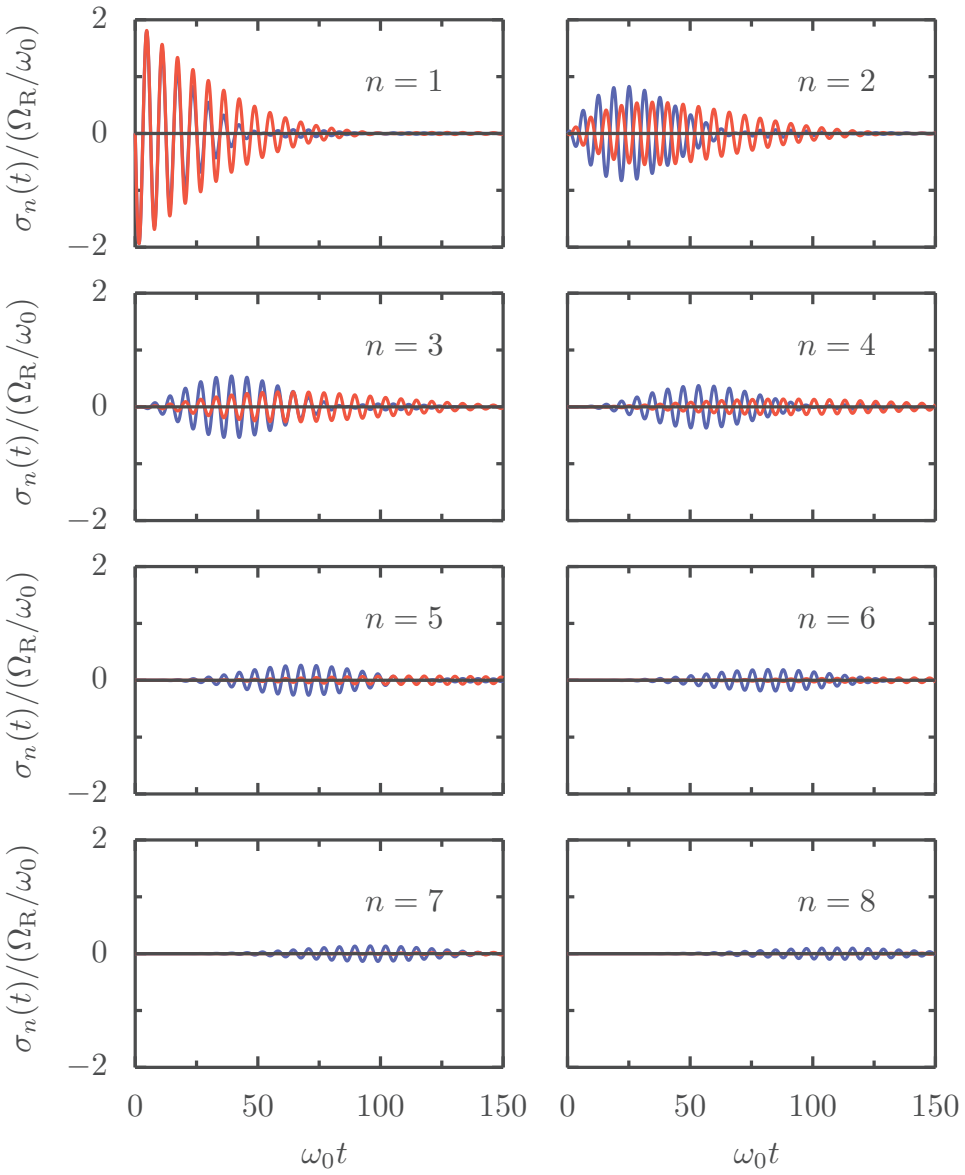

Figure 4.6: Dipole moment on nanoparticle n as a function of time resulting from the excitation of the first nanoparticle by a short pulse [cf. Eq. (4.100)]. The transverse and longitudinal modes are represented by red dashed and blue solid lines, respectively. The parameters used in the figure correspond to an infinite chain of Ag nanoparticles with radius $a = 200\ k_F^{-1} = 16.6$ nm separated by an interparticle distance $d = 3a$.

for the dipole moment on nanoparticle n resulting from a pulsed excitation on the first nanoparticle in the chain.

In Fig. 4.6 we plot the dipole moment (4.100) on nanoparticle $n = 1$ to 8 as a function of time for the transverse (red dashed lines) and longitudinal modes (blue solid lines). The parameters used in the figure correspond to the case of an infinite chain of Ag nanoparticles with ra-

dius $a = 200k_{\mathrm{F}}^{-1} = 16.6$ nm and interparticle distance $d = 3a$. As can be seen on the figure, the initial excitation propagates for at least $n = 8$ nanoparticles in the case of the longitudinal mode, corresponding to a distance of about 400 nm. It is clear from Fig. 4.6 for $n = 1$ to 4 that the transverse mode (cf. red dashed lines in the figure) has a longer lifetime than the longitudinal one (blue solid lines). Such a longer lifetime is associated with lower propagation efficiency. Hence, the longitudinal mode propagates for longer distances than the transverse mode. For instance on the 8^{th} nanoparticle, the longitudinal mode is still active (at the level of a few percent of the initial excitation) while the transverse one is totally suppressed. One may conclude from Fig. 4.6 that, although the signal is strongly damped, it may still be detectable and therefore be useful in the prospect of information transfer based on nanoscale plasmonic metamaterials.

4.5 Conclusions to Chapter 4

In this chapter we have investigated the plasmonic properties of one dimensional nanoparticle assemblies. Adapting theoretical framework of Chapters 2, extended in Chapter 3, we developed a simple model of near-field coupled nanoparticle chain. Within this model we derived a master equation which was utilized to gain insight into the limitation of the propagation of the plasmon along the chain.

We presented how the Landau and the radiation damping are modified through the interaction in the chain of metallic nanoparticles. The former was shown to have almost 40% modulation with respect to the plasmonic momentum, while the latter is separated into sub-radiant and super-radiant modes confirming earlier numerical results [46].

In the propagation study we concluded that the exponential decay of the signal along the chain was resulting from purely non-radiative damping mechanisms present in the system. Thanks to that, using few approximations we obtained analytical expression for the propagation length.

Chapter 5

Conclusions and perspectives

In this thesis we have investigated the properties of collective plasmons in one-dimensional assemblies of spherical metallic nanoparticles. We have studied the influence of the near-field interaction onto the damping mechanisms taking place in the system (i.e. Landau and radiation damping). Using these results we investigated how energy losses limit the propagation of a plasmonic excitation along metallic nanoparticle chains.

In Chapter 2 we have reviewed the theoretical framework of the open quantum system approach within the jellium approximation applied to an isolated metallic nanoparticle. Starting from the microscopic Hamiltonian in the Coulomb gauge we introduced the separation of coordinates into center-of-mass (plasmons) and relative (electrons) ones, which lead to the general form of the system Hamiltonian (2.8), used throughout the chapters 3 and 4 (with addition of the external driving force in Chapter 4). The Hamiltonian (2.8) is characteristic of open quantum systems, where the plasmons are coupled to electronic and photonic environments. The use of a mean-field approximation for the electronic bath enables one to obtain analytical results for the plasmon lifetime.

The coupling between plasmons and electrons originates from the breakdown of Kohn's theorem [89], due to the non-harmonicity of the single-electron confinement potential. This coupling results in a process in which the plasmon decays by producing an electron-hole pair (i.e. Landau damping). In Section 2.3 we have reviewed the method of the evaluation of Landau damping using Fermi's golden rule.

In Section 2.4 we have surveyed the evaluation of the effect of the coupling between plasmons and photons. This coupling leads to radiative losses which are a direct consequence of the radiation from accelerated charges. Using also the Fermi golden rule, one obtains the well-known expression for the radiation damping.

In Chapter 3 we used the theoretical framework of Chapter 2 to investigate how the radiation and Landau damping change in the case

of nanoparticle dimers, which are the building blocks of more complex arrays, such as the nanoparticle chain studied in Chapter 4.

We started our investigation by finding the eigenmodes of the coupled plasmons in a heterogeneous dimer. In Section 3.2, using a Bogoliubov transformation, we determined the eigenstates and eigenenergies of the plasmonic system. Our findings confirmed tendencies found in the literature (i.e. scaling of the eigenenergy with the interparticle distance d as d^{-3} resulting from dipole-dipole interactions) [71,73,75]. The obtained eigenmodes were of twofold nature: symmetric (i.e. plasmons oriented parallel) which is strongly coupled to the light thus dubbed as a bright mode; and anti-symmetric (i.e. plasmon oriented anti-parallel) weakly coupled to the light and dubbed a dark mode.

In Section 3.3 we used the results from Chapter 2 in order to find analytical expressions for the Landau damping decay rate of the collective modes. The behavior of the Landau damping with respect to the interparticle distance showed a change in the linewidth going up to 25%, for longitudinal modes, with respect to the Landau damping of an isolated nanoparticle.

The analytical expression for the radiation damping of the collective modes was obtained in Section 3.4. It was shown that for the case of homogeneous dimers the radiation damping of the dark mode vanishes and the one of the bright mode is twice as large as that of an isolated nanoparticle. In the case of a heterogeneous dimer the dark mode is always radiating. Moreover, for the longitudinal polarization radiation damping of the bright mode increases with the increasing interparticle distance to the point where it becomes larger than the radiation damping of the bright mode.

In Section 3.5 we have presented the size dependence of the total damping (radiation plus Landau) showing that there exists an optimal size that minimizes the total linewidth for the case of the bright modes. Moreover, we also presented two-dimensional maps of the total damping linewidth as a function of both size and interparticle distance. These maps appear as a convenient tool for finding the optimal parameters of the nanoparticle dimer system.

The results presented in Chapter 3 are in very good agreement with the existing experiments [79,80,85,86] and numerical findings [75], thus supporting our analytically-tractable model.

In Chapter 4 we have studied homogeneous nanoparticle chains. We started with the extension of the system Hamiltonian (2.8) by adding a driving term which is of experimental relevance. Considering a finite chain, we used a sine transform and the Bogoliugov transformation in order to obtain the eigenmodes of the collective plasmons, recovering dispersion relation existing in the literature [40].

Using the collective plasmon eigenmodes we derived a master equation for the density matrix of the plasmonic degrees of freedom with

polarization $\sigma = x, y, z$. For the derivation of master equation we assumed the weak coupling limit, as well as the Markovian approximation.

The weak coupling approximation constitutes an assumption ensuring that the coupling between the plasmons and the baths does not change the state of the latter. The Markovian hypothesis accounts for the fact that we are considering the evolution of the system on timescales longer than the correlation times present in the plasmonic system.

In Section 4.2, using the above approximations we obtained a master equation in the Lindblad form, with the decay rates given by the Fermi's golden rule. We also obtained expressions for Lamb shift due to coupling to both electron-hole and photonic environments.

In Section 4.3 we evaluated the Landau and radiation damping rates entering into master equation. We have obtained an analytical expression for the Landau damping and, in the limit of the infinite chain, for the radiation damping as well. The latter was in excellent agreement with previously found numerical results [46], showing the separation into super-radiative (i.e. damping higher than that of a single nanoparticle) and sub-radiative modes (i.e. damping lower than that of a single nanoparticle).

In Section 4.4, we used the master equation, to which we also included a driving term, and phenomenologically, the mode and size independent Ohmic losses. From the master equation we derived the equations of motion for the dimensionless dipole moments in momentum space.

We considered two scenarios of plasmon propagation: in Subsection 4.4.1 we studied the case of the continuous drive using monochromatic electric field, and in Subsection 4.4.2 we investigated the short laser pulse excitation of the plasmon.

Numerical solution of the case with continuous drive for the chain of 1000 Ag nanoparticles, showed two regimes in the quasi-static state. For short distances the decay of the excitation was exponential and it changed to an algebraic one for longer distances. The power laws found by fitting an algebraic decay in the numerically obtained results, yielding the exponent 1 (2) for the transverse (longitudinal) mode. The change from exponential to algebraic decay was understood to be a consequence of the discontinuous behavior of the radiation damping as a function of the plasmonic wavevector. Thus, proving that the exponential decay is of purely non-radiative origin. Using this fact, and neglecting radiation damping (which contributes only to the algebraic decay), we analytically calculated the expression for the plasmon propagation amplitude and the propagation length.

In the case of short laser pulse excitations, we tested that radiation damping weakly influences the pulse propagation. Thus, as in the case of continuous drive, we derived analytical expression for the local dipole

moment.

From our result we conclude that, although the propagation of the plasmon is possible and could be detected. Nonetheless the order of the attenuation is high enough to render signal detection on relatively large distances useless [11]. However, the prospects claimed in the literature of using collective plasmons for signal transmission [37, 40] might be only valid for relatively short distance propagation. A useful outcome of our work is that, our model, when properly adapted, provides a way to obtain the minimization of the losses that limit possible applications of nanoparticle arrays [11].

Our open quantum system approach can be easily adapted to any regular assembly of metallic nanoparticles, giving countless possibilities for potential applications. Using only a few approximations we were able to grasp the basic physics behind the propagation and decay of the collective plasmons in the chains of metallic nanoparticles. Moreover, working within a quantum description allowed us to properly include Landau damping, which is an important ingredient for describing the plasmon lifetime within nanoparticle of small sizes.

The extension of our model toward two [39] and three [66, 67] dimensional regular arrays of nanoparicle is straightforward. Among two dimensional structures [39] there exists a particularly interesting array, which is the honeycomb lattice of metallic nanoparticles [9]. For this special lattice the developed theory predicts the existence of coupled plasmonic states behaving like a massless Dirac bosons. Adapting our approach to this structure may shine some light onto the limitations of the usage of this peculiar metamaterial. In the case of three-dimensional cubic arrays of metallic nanoparticles [66,67] adapting our model can turn out to be useful, especially in order to understand the limitation of the application of plasmon-polaritons present therein.

In our description, we restricted ourselves only to the interaction between the plasmons and the driving electric field, but the interaction of the plasmon with an imposed magnetic field is also possible [30]. In this case, for an isolated nanoparticle, new collective oscillations are formed in the plane perpendicular to the magnetic field. Those new collective excitation are called *magnetoplasmons*. The investigation of how the properties of magnetoplasmons change in the presence of interparticle interaction is of interest from the theoretical and experimental point of view.

Throughout our work we only considered near-field coupled particles. Nevertheless, as we mentioned in the introduction for nearly touching particles new plasmonic states can form (i.e. charge transfer plasmon). In addition, multipolar (i.e. quadrupolar, octupolar, etc.) plasmons may also be excited. The influence of the Landau and radiation damping onto these collective multipolar plasmons of dipolar plasmons may be important from the practical point of view. Moreover,

placing a nanoparticle chain within a cavity, as to achieve the strong coupling regime, may also further modify those properties.

The inclusion of disorder in the nanoparticle arrays is also possible within our model. Earlier theoretical works [53, 65] provided some insight into the influence of disorder onto radiative losses and plasmon propagation. Adapting our approach to incorporate disorder allows to study more realistic systems, with already included quantum dissipation channel. Moreover, such model would be feasible to study Anderson localization of the plasmons within the array.

Finally, the experiment proving existence of the plasmon propagation [43] used Ag nanorods instead, as in our model, nanospheres. Thus, considering non-spherical shapes of the nanoparticle, both isolated [32] and in assembly [38,43], is of great importance from the theoretical and experimental perspective.

Appendix A

Classical radiation of the point dipole

In this appendix we present the derivation of the radiative losses γ_0^{r} [c.f. Eq. (2.45)] arising from the radiated power using classical electrodynamics [70].

The strength of the dipole moment of the plasmon is

$$\mathbf{p} = -eN_{\mathrm{e}}\mathbf{R}. \tag{A.1}$$

The fields produced by this dipole oscillating with the frequency ω_0 can be written as

$$\mathbf{E} = k^2(\hat{r}\times\mathbf{p})\times\hat{r}\frac{e^{\mathrm{i}kr}}{r} + [3\hat{r}(\hat{r}\cdot\mathbf{p}) - \mathbf{p}](\frac{1}{r^3} - \frac{\mathrm{i}k}{r^2})e^{\mathrm{i}kr}, \tag{A.2}$$

$$\mathbf{B} = k^2(\hat{r}\times\mathbf{p})\frac{e^{\mathrm{i}kr}}{r}(1 + \frac{\mathrm{i}}{kr}), \tag{A.3}$$

where $k = \omega_0/c$, with c being the speed of light. Calculating the Poynting vector $\mathbf{S} = (c/4\pi)\mathbf{E}\times\mathbf{B}^*$ and taking the far field limit $r\to\infty$ we have

$$\mathbf{S} = \frac{ck^4p^2}{4\pi r^2}[1 - (\hat{p}\cdot\hat{r})^2]\hat{r}. \tag{A.4}$$

Since our problem has spherical symmetry we may choose an arbitrary coordinate system. Thus for the convenience of the calculation, let us chose $\hat{z}$ direction as that of the plasmon oscillations. Now, the Poynting vector (A.4) can be simplified to

$$\mathbf{S} = \frac{ck^4p^2}{4\pi r^2}\sin^2\theta\hat{r}, \tag{A.5}$$

where θ is the elevation angle of the spherical coordinates r, ϕ, θ. The power radiated per unit of solid angle at the distance r from the dipole is expressed by

$$\frac{\mathrm{d}P}{\mathrm{d}\Omega} = r^2\hat{r}\cdot\mathbf{S} = \frac{ck^4p^2}{4\pi}\sin^2\theta. \tag{A.6}$$

Integrating the above equation over the solid angle

$$P = \frac{ck^4p^2}{4\pi}\int_0^{2\pi} \mathrm{d}\phi \int_0^{\pi} \mathrm{d}\theta \sin^3\theta = \frac{2ck^4p^2}{3} = \frac{2\omega_0^4 p^2}{3c^3}. \tag{A.7}$$

The total energy stored in the oscillating dipole (2.9) can be written as

$$E_{\mathrm{tot}} = \frac{m_{\mathrm{e}}p^2}{2e^2N_{\mathrm{e}}}\omega_0^2. \tag{A.8}$$

Thus, time-averaged power reads

$$\bar{P} = \frac{\omega_0^4 p^2}{3c^3} = \frac{2\omega_0 N_{\mathrm{e}} e^2}{3c^3 m_{\mathrm{e}}} E_{\mathrm{tot}}, \tag{A.9}$$

and the loss of the energy due to the radiated power may be expressed as

$$\frac{\mathrm{d}E_{\mathrm{tot}}}{\mathrm{d}t} = -\bar{P} = -\frac{1}{\tau}E_{\mathrm{tot}}, \tag{A.10}$$

where $1/\tau = \gamma_{\mathrm{r}}$ is radiative lifetime of the dipole i.e. the inverse of the radiation damping, which reads

$$\gamma_0^{\mathrm{r}} = \frac{2\omega_0^4}{3c^3}a^3. \tag{A.11}$$

The above expression is the same as Eq. (2.45), thus providing an alternative path for the calculation of radiation damping.

List of publications

1. Adam Brandstetter-Kunc, Guillaume Weick, Dietmar Weinmann, Rodolfo A. Jalabert, Decay of dark and bright plasmonic modes in a metallic nanoparticle dimer, Phys. Rev. B **91**, 035431 (2015).

   Erratum: Phys. Rev. B **92**, 199906 (2015).

2. Adam Brandstetter-Kunc, Guillaume Weick, Charles A. Downing, Dietmar Weinmann, Rodolfo A. Jalabert, Nonradiative limitations to plasmon propagation in chains of metallic nanoparticles, Phys. Rev. B **94**, 205432 (2016).

Conferences

1. August 24-29th 2014, 25th Conference of the Condensed Matter Division of the EPS - 14th Journées de la Matière Condensée (CMD 25 - JMC 14), Paris, Oral presentation: Landau damping of coupled plasmonic modes in metallic nanoparticle dimers

2. September 22-26th 2014, Conference: Echoes in Complex Systems, Dresden, Poster: The dark side of plasmonic decay in a metallic nanoparticle dimer

3. December 1-4th 2014, GDR Physique quantique mésoscopique, Aussois, Poster: The dark side of plasmonic decay in a metallic nanoparticle dimer

4. August 24-28th 2015, 23th congrès général de la Société Française de Physique, Strasbourg, Poster: Plasmon propagation and energy losses in chains of metallic nanoparticles

Bibliography

[1] U. Kreibig and M. Vollmer, *Optical properties of metal clusters*, (Springer-Verlag, Berlin, 1995)

[2] W. L. Barnes, A. Dereux, and T. W. Ebbesen, Surface plasmon subwavelength optics, Nature **424**, 824 (2003).

[3] S. A. Maier, *Plasmonics: Fundamentals and Applications* (Springer-Verlag, Berlin, 2007).

[4] J. A. Schuller, E. S. Barnard, W. Cai, Y. Chul Jun, J. S. White and M. L. Brongersma, Plasmonics for extreme light concentration and manipulation Nature Materials **9**, 193 (2010).

[5] N. W. Ashcroft and N. D. Mermin, *Solid state physics* (Harcourt, Orlando, 1976).

[6] J.-Y. Bigot, V. Halté, J.-C. Merle, A. Daunois, Electron dynamics in metallic nanoparticles, Chem. Phys. **251**, 181 (2000).

[7] S. Schlücker, SERS Microscopy: Nanoparticle Probes and Biomedical Applications, ChemPhysChem **10**, 1344-1354 (2009).

[8] J. Grand, M. Lamy de la Chapelle, J.-L. Bijeon, P.-M. Adam, A. Vial, and P. Royer, Role of localized surface plasmons in surface-enhanced Raman scattering of shape-controlled metallic particles in regular arrays, Phys. Rev. B **72**, 033407 (2005).

[9] G. Weick, C. Woollacott, W. L. Barnes, O. Hess, and E. Mariani, Dirac-like plasmons in honeycomb lattices of metallic nanoparticles, Phys. Rev. Lett. **110**, 106801 (2013).

[10] T. J. Sturges, C. Woollacott, G. Weick, and E. Mariani, Dirac plasmons in bipartite lattices of metallic nanoparticles, 2D Mater. **2**, 014008 (2015).

[11] J. B. Khurgin, How to deal with the loss in plasmonics and metamaterials, Nat. Nanotechnol. **10**, 2 (2015).

[12] G. Mie, Beiträge zur Optik trüber Medien, speziell kolloidaler Metallösungen, Ann. Phys. (Leipzig) **25**, 377 (1908).

[13] I. Freestone, N. Meeks, M. Sax, and C. Higgitt, The Lycurgus cup: A Roman nanotechnology, Gold Bull. **40**, 270 (2007).

[14] A. Kawabata and R. Kubo, J. Phys. Soc. Jap., **21**, 1765 (1966).

[15] R. Ruppin and H. Yatom, Size and Shape Effects on the Broadening of the Plasma Resonance Absorption in Metals, Phys. Stat. Solidi B **74**, 647 (1975).

[16] K.-P. Charle, W. Schulze, and B. Winter, The size dependent shift of the surface plasmon absorption band of small spherical metal particles, Z.Phys. D **12**, 471 (1989).

[17] C. Yannouleas and R.A. Broglia, Landau damping and wall dissipation in large metal clusters, Ann. Phys. **217**, 1 (1992).

[18] W. A. de Heer, The physics of simple metal clusters: experimental aspects and simple models, Rev. Mod. Phys **65**, 611 (1993).

[19] R. A. Molina, R. A. Jalabert, and D. Weinmann, Oscillatory size dependence of the surface plasmon linewidth in metallic nanoparticles, Phys. Rev. B **65**, 155427 (2002).

[20] C Sönnichsen, T Franzl, T Wilk, G von Plessen and J Feldmann, Plasmon resonances in large noble-metal clusters, New J. Phys. **4**, 93 (2002).

[21] L. G. Gerchikov, C. Guet, and A. N. Ipatov,, Multiple plasmons and anharmonic effects in small metallic clusters, Phys. Rev. A **66**, 053202 (2002).

[22] R.A. Molina, D. Weinmann and R.A. Jalabert, Oscillatory behavior and enhancement of the surface plasmon linewidth in embedded noble metal nanoparticles, Eur. Phys. J. D **24**, 127 (2003).

[23] K. Hagino, G. F. Bertsch, and C. Guet, Variational RPA for the dipole surface plasmon in metal clusters, Nucl. Phys. A **731**, 347 (2004).

[24] G. Weick, R. A. Molina, D. Weinmann, and R. A. Jalabert, Lifetime of the first and second collective excitations in metallic nanoparticles, Phys. Rev. B **72**, 115410 (2005).

[25] G. Weick, G.-L. Ingold, R. A. Jalabert, and D. Weinmann, Surface plasmon in metallic nanoparticles: Renormalization effects due to electron-hole excitations, Phys. Rev. B **74**, 165421 (2006).

[26] G. Weick, G.-L. Ingold, D. Weinmann, and R. A. Jalabert, Sidebands in the light absorption of driven metallic nanoparticles, Eur. Phys. J. D **44**, 359 (2007).

[27] C. Seoanez, G. Weick, R. A. Jalabert, and D. Weinmann, Friction of the surface plasmon by high-energy particle-hole pairs, Eur. Phys. J. D **44**, 351 (2007).

[28] H. Baida, P. Billaud, S. Marhaba, D. Christofilos, E. Cottancin, A. Crut, J. Lermé, P. Maioli, M. Pellarin, M. Broyer, N. Del Fatti, F. Vallée, A. Sánchez-Iglesias, I. Pastoriza-Santos and L. M. Liz-Marzán, Quantitative Determination of the Size Dependence of Surface Plasmon Resonance Damping in Single Ag@SiO_2 Nanoparticles, Nano Lett. **9**, 3463 (2009).

[29] W. Jacak, J. Krasnyj, J. Jacak1, R. Gonczarek1, A. Chepok, L. Jacak, D. Z. Hu and D. Schaadt, Radius dependent shift in surface plasmon frequency in large metallic nanospheres: Theory and experiment, J. Appl. Phys. **107**, 124317 (2010).

[30] G. Weick and D. Weinmann, Lifetime of the surface magnetoplasmons in metallic nanoparticles, Phys. Rev. B **83**, 125405 (2011).

[31] G. Manfredi, P-A. Hervieux and F. Haas, Nonlinear dynamics of electron–positron clusters, New J. Phys. **14**, 075012 (2012).

[32] V. Juvé, M. F. Cardinal, A. Lombardi, A. Crut, P. Maioli, J. Pérez-Juste, L.M. Liz-Marzán, N. Del Fatti, and F. Vallée, Nano Lett. **13**, 2234 (2013).

[33] P. Zhang, J. Feist, A. Rubio, P. García-González, and F. J. García-Vidal, Ab initio nanoplasmonics: The impact of atomic structure, Phys. Rev. B **90**, 161407(R) (2014).

[34] S. Raza, S. I. Bozhevolnyi, M. Wubs, and N. A. Mortensen, Nonlocal optical response in metallic nanostructures, J. Phys.: Condens. Matter **27**, 183204 (2015).

[35] J. Hurst, K. Lévêque-Simon, P-A. Hervieux, G. Manfredi, and F. Haas, High-harmonic generation in a quantum electron gas trapped in a nonparabolic and anisotropic well, Phys. Rev. B **93**, 205402 (2016).

[36] J. M. Gérardy and M. Ausloos, Absorption spectrum of clusters of spheres from the general solution of Maxwell's equations. II. Optical properties of aggregated metal spheres, Phys. Rev. B **25**, 4204 (1982).

[37] M. Quinten, A. Leitner, J. R. Krenn, and F. R. Aussenegg, Electromagnetic energy transport via linear chains of silver nanoparticles, Opt. Lett. **23**, 17 (1998).

[38] J. R. Krenn, A. Dereux, J. C. Weeber, E. Bourillot, Y. Lacroute, J. P. Goudonnet, G. Schider, W. Gotschy, A. Leitner, F. R. Aussenegg, and C. Girard, Squeezing the optical near-field zone by plasmon coupling of metallic nanoparticles, Phys. Rev. Lett. **82**, 2590 (1999).

[39] B. Lamprecht, G. Schider, R. T. Lechner, H. Ditlbacher, J. R. Krenn, A. Leitner, and F. R. Aussenegg, Metal Nanoparticle Gratings: Influence of Dipolar Particle Interaction on the Plasmon Resonance, Phys. Rev. Lett. **84**, 4721 (2000).

[40] M. L. Brongersma, J. W. Hartman, and H. A. Atwater, Electromagnetic energy transfer and switching in nanoparticle chain arrays below the diffraction limit, Phys. Rev. B **62**, 24 (2000).

[41] S. A. Maier, P. G. Kik, H. A. Atwater, Observation of coupled plasmon-polariton modes in Au nanoparticle chain waveguides of different lengths: Estimation of waveguide loss, App. Phys. Lett. **81**, 1714 (2002).

[42] S. A. Maier, M. L. Brongersma, P. G. Kik, and H. A. Atwater, Observation of near-field coupling in metal nanoparticle chains using far-field polarization spectroscopy, Phys. Rev. B **65**, 193408 (2002).

[43] S. A. Maier, P. G. Kik, H. A. Atwater, S. Meltzer, E. Harel, B. E. Koel, A. A.G. Requicha, Local detection of electromagnetic energy transport below the diffraction limit in metal nanoparticle plasmon waveguides, Nature Mater. **2**, 229 (2003).

[44] S. A. Maier, M. L. Brongersma, P. G. Kik, H. A. Atwater, Optical pulse propagation in metal nanoparticle chain waveguides, Phys. Rev. B **67**, 205402 (2003).

[45] S. Y. Park and D. Stroud, Surface-plasmon dispersion relations in chains of metallic nanoparticles: An exact quasistatic calculation, Phys. Rev. B **69**, 125418 (2004).

[46] W. H. Weber and G. W. Ford, Propagation of optical excitations by dipolar interactions in metal nanoparticle chains, Phys. Rev. B **70**, 125429 (2004).

[47] D. S. Citrin, Coherent excitation transport in metal-nanoparticle chains, Nano Lett. **4**, 1561 (2004).

[48] S. Zou, N. Janel and G. C Schatz, Silver nanoparticle array structures that produce remarkably narrow plasmon lineshapes , J. Chem. Phys. **120**, 10871 (2004).

[49] L. A. Sweatlock, S. A. Maier, H. A. Atwater, J. J. Penninkhof, and A. Polman, Highly confined electromagnetic fields in arrays of strongly coupled Ag nanoparticles, Phys. Rev. B **71**, 235408 (2005).

[50] S. Zou and G. C Schatz, Theoretical studies of plasmon resonances in one-dimensional nanoparticle chains: narrow lineshapes with tunable widths, Nanotechnology **17**, 2813 (2006).

[51] D. S. Citrin, Plasmon-polariton transport in metal-nanoparticle chains embedded in a gain medium, Opt. Lett. **31**, 98 (2006).

[52] A. F. Koenderink and A. Polman, Complex response and polariton-like dispersion splitting in periodic metal nanoparticle chains, Phys. Rev. B **74**, 033402 (2006).

[53] V. A. Markel and A. K. Sarychev, Propagation of surface plasmons in ordered and disordered chains of metal nanospheres, Phys. Rev. B **75**, 085426 (2007).

[54] K. B. Crozier, E. Togan, E. Simsek and T. Yang, Experimental measurement of the dispersion relations of the surface plasmon modes of metal nanoparticle chains, Optics Express **15**, 17482 (2007).

[55] B. Auguié and W. L. Barnes, Collective Resonances in Gold Nanoparticle Arrays, Phys. Rev. Lett. **101**, 143902 (2008).

[56] B. Willingham and S. Link, Energy transport in metal nanoparticle chains via sub-radiant plasmon modes, Optics Express **19**, 6450 (2011).

[57] C. Lee, M. Tame, J. Lim, and J. Lee, Quantum plasmonics with a metal nanoparticle array, Phys. Rev. A **85**, 063823 (2012).

[58] D. Solis, Jr., B. Willingham, S. L. Nauert, L. S. Slaughter, J. Olson, P. Swanglap, A. Paul, W.-S. Chang and S. Link, Electromagnetic Energy Transport in Nanoparticle Chains via Dark Plasmon Modes, Nano Lett. **12**, 1349 (2012).

[59] W. Jacak, On Plasmon Polariton Propagation Along Metallic Nano-Chain, Plasmonics **8**, 1317 (2013).

[60] A. Apuzzo, M. Fevrier, R. Salas-Montiel, A. Bruyant, A. Chelnokov, G. Lerondel, B. Dagens and S. Blaize, Observation of near-field dipolar interactions involved in a metal nanoparticle chain waveguide, Nano Lett. **13**, 1000 (2013).

[61] J. del Pino, J. Feist, F.J. Garcia-Vidal and J. J. Garcia-Ripoll, Entanglement detection in coupled particle plasmons, Phys. Rev. Lett. **91**, 216805 (2014).

[62] S. J. Barrow, D. Rossouw, A. M. Funston, G. A. Botton, and P. Mulvaney, Mapping Bright and Dark Modes in Gold Nanoparticle Chains using Electron Energy Loss Spectroscopy, Nano Lett. **14**, 3799 (2014).

[63] N. Meinzer, W. L. Barnes, I. R. Hooper, Plasmonic meta-atoms and metasurfaces, Nat, Phot. **8**, 889–898 (2014).

[64] R. A. Bustos-Marún, A. D. Dente, E. A. Coronado and H. M. Pastawski, Tailoring Optical Fields Emitted by Subwavelength Nanometric Sources, Plasmonics **9**, 925 (2014).

[65] M. Petrov, Disorder-induced Purcell enhancement in nanoparticle chains, Phys. Rev. A **91**, 023821 (2015).

[66] G. Weick and E. Mariani, Tunable plasmon polaritons in arrays of interacting metallic nanoparticles, Eur. Phys. J. B **88**, 7 (2015).

[67] S. Lamowski, F. Hellbach, E. Mariani, G. Weick, and F. Pauly, Plasmon polaritons in cubic lattices of spherical metallic nanoparticles, arXiv:1606.04897.

[68] G. Manfredi and F. Haas, Self-consistent fluid model for a quantum electron gas, Phys. Rev. B **64**, 075316 (2001).

[69] P. B. Johnson and R. W. Christy, Optical Constants of the Noble Metals, Phys. Rev. B **6**, 4370 (1972).

[70] J. D. Jackson, *Classical Electrodynamics*, 2nd ed. (Wiley, New York, 1962)

[71] R. Ruppin, Surface modes of two spheres, Phys. Rev. B **26**, 3440 (1982).

[72] J. M. Gérardy and M. Ausloos, Absorption spectrum of clusters of spheres from the general solution of Maxwell's equations. IV. Proximity, bulk, surface, and shadow effects (in binary clusters), Phys. Rev. B **27**, 6446 (1983).

[73] P. Nordlander, C. Oubre, E. Prodan, K. Li and M. I. Stockman, Plasmon Hybridization in Nanoparticle Dimers, Nano Lett. **4**, 899 (2004).

[74] C. Dahmen, B. Schmidt, and G. von Plessen, Radiation Damping in Metal Nanoparticle Pairs, Nano Lett. **7**, 318 (2007).

[75] J. Zuloaga, E. Prodan, and P. Nordlander, Quantum description of the plasmon resonances of a nanoparticle dimer, Nano Lett. **9**, 887 (2009).

[76] G. S. Smith, An insightful problem involving the electromagnetic radiation from a pair of dipoles, Eur. j. Phys. **31**, 819 (2010).

[77] R. Esteban, A. G. Borisov, P. Nordlander, and J. Aizpurua, Bridging quantum and classical plasmonics with a quantum-corrected model, Nat. Comm. **3**, 825 (2012).

[78] D.C. Marinica, A.K. Kazansky, P. Nordlander, J. Aizpurua, and A. G. Borisov, Quantum Plasmonics: Nonlinear Effects in the Field Enhancement of a Plasmonic Nanoparticle Dimer, Nano Lett. **12**, 1333 (2012).

[79] H. Tamaru, H. Kuwata, H. T. Miyazaki, and K. Miyano, Resonant light scattering from individual Ag nanoparticles and particle pairs, Appl. Phys. Lett. **80**, 1826 (2002).

[80] W. Rechberger, A. Hohenau, A. Leitner, J. R. Krenn, B. Lamprecht, and F. R. Aussenegg, Optical properties of two interacting gold nanoparticles, Opt. Commun. **220**, 137 (2003).

[81] P. K. Jain, W. Huang, and M. A. El-Sayed, On the Universal Scaling Behavior of the Distance Decay of Plasmon Coupling in Metal Nanoparticle Pairs: A Plasmon Ruler Equation, Nano Lett. **7**, 2080 (2007).

[82] G. Bachelier, I. Russier-Antoine, E. Benichou, C. Jonin, N. Del Fatti, F. Vallée, and P.-F. Brevet, Fano Profiles Induced by Near-Field Coupling in Heterogeneous Dimers of Gold and Silver Nanoparticles, Phys. Rev. Lett. **101**, 197401 (2008).

[83] P. Olk, J. Renger, M. T. Wenzel, and L. M. Eng, Distance dependent spectral tuning of two coupled metal nanoparticles, Nano Lett. **8**, 1174 (2008).

[84] M.-W. Chu, V. Myroshnychenko, C. H. Chen, J.-P. Deng, C.-Y. Mou, and F. J. García de Abajo, Probing Bright and Dark Surface-Plasmon Modes in Individual and Coupled Noble Metal Nanoparticles Using an Electron Beam, Nano Lett. **9**, 399 (2009).

[85] A. L. Koh, K. Bao, I. Khan, W. E. Smith, G. Kothleitner, P. Nordlander, S. A. Maier, and David W. McComb, Electron Energy-Loss Spectroscopy (EELS) of Surface Plasmons in Single Silver Nanoparticles and Dimers: Influence of Beam Damage and Mapping of Dark Modes, ACS Nano **3**, 3015 (2009).

[86] P. K. Jain and M. A. El-Sayed, Plasmonic coupling in noble metal nanostructures, Chem. Phys. Lett. **487**, 153 (2010).

[87] C. Girard, and A. Dereux, Near-field optics theories, Rep. Prog. Phys., **59**, 657 (1996).

[88] M. Brack, The physics of simple metal clusters: self-consistent jellium model and semiclassical approaches, Rev. Mod. Phys **66**, 677 (1993).

[89] W. Kohn, Cyclotron Resonance and de Haas-van Alphen Oscillations of an Interacting Electron Gas, Phys. Rev. **123**, 1242 (1961).

[90] C. Tsallis, Diagonalization methods for the general bilinear Hamiltonian of an assembly of bosons, J. Math. Phys. **19**, 277 (1978).

[91] C. Cohen-Tannoudji, J. Dupont-Roc, and G. Grynberg, *Atom-Photon Interactions: Basic Processes and Applications*, (Wiley-VCH, New York, 1992).

[92] D.L. Andrews, A unified theory of radiative and radiationless molecular energy transfer, Chem. Phys. **2**, 195 (1989).

[93] L. Jacak, P. Hawrylak, and A. Wójs, *Quantum Dots* (Springer-Verlag, Berlin, 1998).

[94] C. W. Gardiner and P. Zoller, *Quantum Noise*, (Springer-Verlang, Berlin 2000), 2$^{\text{nd}}$ enlarged ed.

[95] M. C. Gutzwiller, *Chaos in classical and quantum mechanics*, (Springer-Verlang, Berlin, 1990).

[96] M. Brack and R. K. Bhaduri, *Semiclassical physics*, Frontiers in Physics (Addison-Wesley, Reading, 1997)

[97] G. F. Bertsch and R. A. Broglia, *Oscillations in Finite Quantum Systems* (Cambridge University Press, Cambridge, 1994).

Adam BRANDSTETTER-KUNC

Decay of plasmonic excitations in one dimensional assemblies of metallic nanoparticles

Résumé

Nous avons étudié la dynamique des électrons dans des réseaux de nanoparticules métalliques. Nous avons d'abord considiré le réseau le plus simple, c'est-à-dire le dimère de nanoparticules. Nous avons trouvé des fréquences propres du dimère hétérogène et ensuite nous avons appliqué l'approche du système quantique ouvert pour décrire les processus d'amortissement présents dans le système. Nous avons étudié deux processus d'amortissement qui dépendent de la taille des nanoparticules constituant le dimère: l'amortissement de Landau avec une proportionnalité inverse à la taille du système, et l'amortissement radiatif, proportionnel au volume du système. En utilisant les résultats de l'étude des dimères, nous avons étendu notre approche du système quantique ouvert pour étudier des chaînes de nanoparticules unidimensionnelles. Nous avons dérivé une équation maîtresse qui a été utilisée pour étudier la propagation des plasmons le long de la chaîne. Nous avons constaté que la propagation du plasmon est limitée que par les sources non radiatives d'amortissement. Enfin, nous avons dérivé l'expression analytique de la longueur de propagation d'un plasmon dans une chaîne de nanoparticules.

Mots clés : *Matière condensée, physique mésoscopique, plasmonique, dynamique des électrons*

Résumé en anglais

We studied the electron dynamics in metallic nanoparticle arrays. We first considered the simplest array i.e. a nanoparticle dimer. We found the eigenfrequencies of the heterogeneous dimer and then we applied the open quantum system approach to describe the decay processes present in the system. We investigated two decay processes which depend on the size of the nanoparticles building up the dimer : the Landau damping, inversly proportional to the system-size, and radiation damping, proportional to the volume of the system. Using the results of the dimer study we extended our open quantum system approach to study one-dimensional nanoparticle chains. We derived a master equation and used it to investigate the propagation of plasmons along the chain. We found that the propagation of the plasmon is limited by the non-radiative sources of damping. Finally we derived an analytical expression for the propagation length of a plasmon in a nanoparticle chain.

Keywords : *condensed matter, mesoscopic physics, plasmonics, electron dynamics*